

NOVEL VOLUMETRIC PLASMONIC
RESONATOR ARCHITECTURES FOR
ENHANCED ABSORPTION IN THIN-FILM
ORGANIC SOLAR CELLS

A THESIS
SUBMITTED TO THE DEPARTMENT OF ELECTRICAL AND
ELECTRONICS ENGINEERING
AND THE INSTITUTE OF ENGINEERING AND SCIENCES
OF BILKENT UNIVERSITY
IN PARTIAL FULLFILMENT OF THE REQUIREMENTS
FOR THE DEGREE OF
MASTER OF SCIENCE

By
Mustafa Akın Sefünç
August 2010

I certify that I have read this thesis and that in my opinion it is fully adequate, in scope and in quality, as a thesis for the degree of Master of Science.

Assoc. Prof. Dr. Hilmi Volkan Demir (Supervisor)

I certify that I have read this thesis and that in my opinion it is fully adequate, in scope and in quality, as a thesis for the degree of Master of Science.

Assist. Prof. Dr. Ali Kemal Okyay (Co-Supervisor)

I certify that I have read this thesis and that in my opinion it is fully adequate, in scope and in quality, as a thesis for the degree of Master of Science.

Assoc. Prof. Dr. Oğuz Gülseren

Approved for the Institute of Engineering and Sciences:

Prof. Dr. Levent Onural
Director of Institute of Engineering and Sciences

ABSTRACT

**NOVEL VOLUMETRIC PLASMONIC RESONATOR
ARCHITECTURES FOR ENHANCED ABSORPTION IN
THIN-FILM ORGANIC SOLAR CELLS**

Mustafa Akin Sefiunç

M.S. in Electrical and Electronics Engineering

Supervisor: Assoc. Prof. Dr. Hilmi Volkan Demir

August 2010

There has been a growing interest in decreasing the cost and/or increasing the efficiency of clean renewable energy resources including those of photovoltaic approaches for conversion of sunlight into electricity. Today, although photovoltaics is considered a potential candidate in diversification of energy sources, the cost of photovoltaic systems remains yet to be reduced by several factors to compete with fossil fuel based energy production. To this end, new generation solar cells are designed to feature very thin layers of active (absorbing) materials in the order of tens of nanometers. Though this approach may possibly decrease the cost of solar cells, these ultra-thin absorbing layers suffer from undesirably low optical absorption of incident photons. Recently revolutionary efforts on increasing light trapping using nanopatterned metal layers in the active photovoltaic material via surface plasmon excitations have been demonstrated, which attracted interest of the academic community as well as the industry. In these prior studies, plasmonic structures, placed either on the top or at the bottom of absorbing layers, have been investigated to enhance the absorption in the active material. However, all these previous efforts were based only on using a single layer of plasmonic structures. In this thesis, different than

the previous reports of our group and the others, we focus on a new design concept of volumetric plasmonic resonators that relies on the idea of incorporating two (or more) layers of coupled plasmonic structures embedded in the organic solar cells. For proof-of-concept demonstration, here we embody one silver grating on the top of the absorbing layer and another at the bottom of the active layer to couple them with each other such that the resulting field localization is further increased and extended within the volume of the active material. In addition to individual plasmonic resonances of these metallic structures, this allows us to take the advantage of the vertical interaction in the volumetric resonator. Our computational results show that this architecture exhibits a substantial absorption enhancement performance particularly under the transverse-magnetic polarized illumination, while the optical absorption is maintained at a similar level as the top grating alone under the transverse-electric polarized illumination. As a result, the optical absorption in the active layer is enhanced up to ~67%, surpassing the improvement limit of individual gratings, when the total film thickness is kept fixed. This volumetric interaction contributes to further enhancement of optical absorption in the active layer, beyond the limited photon absorption in non-metallic (bare) organic solar cell.

Keywords: Photovoltaics, plasmonics, surface plasmons, localized plasmons, organic solar cells, FDTD.

ÖZET

İNCE-FİLM ORGANİK GÜNEŞ HÜCRELERİNDE OPTİK SOĞRULMAYI ARTIRMAK İÇİN TASARLANMIŞ YENİ HACİMSEL PLAZMONİK REZONATÖR MİMARİLERİ

Mustafa Akın Sefünç

Elektrik ve Elektronik Mühendisliği Bölümü Yüksek Lisans

Tez Yöneticisi: Doç. Dr. Hilmi Volkan Demir

Ağustos 2010

Son zamanlarda, temiz yenilenebilir enerji kaynaklarının, özellikle güneş ışığını elektriğe dönüştürme için uygulanan fotovoltaik yaklaşımlarının, maliyetlerinin azaltılması ve/ya verimliliklerini arttırılması için artan bir ilgi vardır. Günümüzde, fotovoltaik, enerji kaynaklarının çeşitlendirilmesinde potansiyel bir aday olarak kabul edilmesine rağmen, bu sistemlerin fosil yakıt tabanlı enerji üretimi ile rekabet edebilmesi için maliyetinin birkaç kat azaltılması gerekmektedir. Bu amaçla yeni nesil güneş hücrelerinin aktif (soğurucu) malzemeleri çok ince (onlarca nanometre mertebesinde) tabakalar olarak tasarlanmaktadır. Bu yaklaşım güneş hücrelerinin maliyetini azaltmasına karşın bu ultra-ince emici tabakalar gelen fotonların optik soğurma performansını düşürmektedir. Son günlerde yüzey plazmon uyarılmaları aracılığı ile nanoboyutta şekillendirilmiş metal katmanlar kullanarak etkin fotovoltaik malzeme soğurulumu artırmak üzerine yapılan ilerici çalışmalar akademik topluluğun yanı sıra sanayiden de ilgi görmektedir. Bundan önceki çalışmalarda, aktif malzeme soğurulumu artırmak için emici tabakanın üst veya alt kısmına yerleştirilmiş plazmonik yapılar incelenmiştir. Ancak tüm bu önceki çalışmalar, sadece tek katmanlı plasmonik yapılar kullanılmasına dayanmaktadır. Bu tez çalışmasında, grubumuz ve başka grupların önceki çalışmalarından farklı olarak,

organik güneş pillerinde yeni bir tasarım kavramı olan, iki (veya daha fazla) plazmonik yapıların birleştirilmesi fikrine dayanan hacimsel plazmonik rezonatörler üzerine odaklanılmıştır. Kavram ispatı gösterimi için, soğurucu tabakanın üstüne ve altına birer gümüş ızgara eklenerek, birbirlerinin etkileşimleri sayesinde oluşan elektrik alanın artışı aktif tabakanın hacmi içinde gözlenmiştir. Bu yaklaşım, metalik yapıların bireysel plazmonik rezonanslarına ek olarak, hacimsel rezonatör içinde oluşan dikey etkileşim avantajını kullanmaktadır. Hesaplamasal bulgularımız gösteriyor ki; optik soğrulma enine elektrik (TE) polarize ışık altında üst ızgara ile benzer düzeyde korunurken, enine manyetik (TM) polarize ışık altında artan bir soğurma performansı sergiler. Sonuç olarak, toplam film kalınlığı sabit tutulduğunda, aktif katmanda optik soğrulma tek başına ızgara iyileştirme sınırını aşarak %~67 artırılmıştır. Bu hacimsel etkileşim metalik olmayan (yalın) organik güneş pillerindeki sınırlı foton soğrulma miktarı ötesinde aktif katmandaki optik soğrulmanın artırılmasına ek katkıda bulunmaktadır.

Anahtar kelimeler: Fotovoltaik, plazmonik, yüzey plazmonları, lokalize plazmonlar, organik güneş hücreleri, FDTD.

Acknowledgements

I owe my deepest gratitude to my supervisor Assoc. Prof. Dr. Hilmi Volkan Demir for his endless support from the beginning of my academic career. He always wanted the best for me and encouraged me to do so. His positive attitude to life has been always a trigger and motivation for me.

I would like to thank my co-supervisor Asst. Prof. Dr. Ali Kemal Okyay for his guidance and support in our collaborative research work and also giving useful comments and suggestions as being a member of my thesis committee.

I would like to thank Assoc. Prof. Dr. Oguz Gülseren for his contributions and guidance during my research efforts and also giving useful comments and suggestions as being a member of my thesis committee.

I am very proud to dedicate my thesis to my mother; Gülendâmy Sefünç, my father; Atila Sefünç and my brother; Yavuz Selim Sefünç for their endless love and endless supports in my life. They always support me a lot to achieve my goals since my childhood.

This thesis would not have been possible unless their presence of my uncle Abdulvahap Fatih Gülmen, who has been like a father, and my aunt Seçkin Gülmen, who has been like a mother. I believe that my grandfather Mehmet Sabri Kelemerođlu (Gülmen) who passed away years ago, should be proud of where I am now, if he was alive today. I also would like to show my gratitude to my grandfather Ziya Sefünç, my grandmothers Rukiye Gülmen and Nedret Sefünç, and also my uncle Ali Sefünç.

I really want to thank to my ex-neighbors and my over 12 years old friends Muhammed Şafakođlu and Fatih Kürşat Şafakođlu for their endless friendship, endless support and hospitality all the time. I would also like to thank their father and my dear teacher Turgut Şafakođlu for his support and hospitality.

I would like to thank all former and recent group members of Devices and Sensors Group, who work under the supervision of H. Volkan Demir. I would especially like to thank Ugur Karatay, Refik Sina Toru, Nihan Kosku Perkgöz, Burak Güzeltürk, Talha Erdem, Can Uran, Evren Mutlugün, Sedat Nizamođlu, Tuncay Özel, Özge Özel, Veli Tayfun Kılıç, Sayim Gökyar, Neslihan Çiçek, Gülis Zengin, Emre Sarı, Özgün Akyüz, Emre Ünal, Urartu Şeker and Rohat Melik for their friendship and collaborations.

Lastly, I offer my regards and blessings to Murat Cihan Yüksek, Onur Akin, Kazım Gürkan Polat, Alper Yeşilyurt, Özgür Kazar, Gökçe Balkan, Eyüp Güler, who supported me in any respect during the completion of the project.

Table of Contents

ACKNOWLEDGEMENTS.....	VII
TABLE OF CONTENTS.....	X
CHAPTER 1 INTRODUCTION.....	1
CHAPTER 2 FUNDAMENTALS OF PLASMONICS.....	6
2.1 SURFACE PLASMONS	8
2.2 LOCALIZED SURFACE PLASMONS	18
2.3 PLASMONICS FOR PHOTOVOLTAICS	19
2.4 FINITE-DIFFERENCE TIME-DOMAIN (FDTD) METHOD	23
CHAPTER 3 PRINCIPLES OF ORGANIC SOLAR CELLS.....	26
3.1 ORGANIC SOLAR CELL ARCHITECTURES AND THEIR OPERATION PRINCIPLES	29
3.2 MATERIALS	33
CHAPTER 4 INCREASED ABSORPTION FOR ALL POLARIZATIONS VIA EXCITATION OF PLASMONIC MODES IN METALLIC GRATING BACKCONTACT.....	38
4.1 DEVICE STRUCTURE.....	40
4.2 NUMERICAL SIMULATIONS	43
4.3 NUMERICAL ANALYSES.....	44
CHAPTER 5 VOLUMETRIC PLASMONIC RESONATORS FOR INCREASED ABSORPTION IN THIN-FILM ORGANIC SOLAR CELLS.....	64
5.1 DEVICE STRUCTURE.....	66
5.2 NUMERICAL SIMULATIONS	69
5.3 ABSORPTION BEHAVIOR OF ORGANIC SOLAR CELLS EMBEDDED WITH PLASMONIC STRUCTURES UNDER TE AND TM POLARIZED ILLUMINATION.....	70
5.4 OPTIMIZATION RESULTS.....	78
CHAPTER 6	89
CONCLUSIONS.....	89
BIBLIOGRAPHY	92

List of Figures

Figure 2.1: Lycurgus Cup (4th century A.D.) under different illuminations from outside (left) and inside (right) in British Museum (retrieved from the webpage http://www.britishmuseum.org/explore/highlights/highlight_objects/pe_mla/t/the_lycurgus_cup.aspx).	7
Figure 2.2: Dielectric/metal interface considered in the dispersion relation derivation of surface plasmons. The structure is omitted to be infinite in y direction [7].	9
Figure 2.3: Visualization of surface plasmons at the metal/dielectric interface: the surface charge oscillations in the transverse magnetic (TM) case, while the magnetic field (H) is in the y-direction and the electric field (E) is normal to the surface [6].	14
Figure 2.4: Dispersion relation for existing surface plasmons [6].	15
Figure 2.5: The electric field profile at the dielectric/metal interface. δ_d is the decay length of the field in dielectric medium and δ_m is the decay length of the field in metal medium [6].	16
Figure 2.6: Field profile of light-to-surface plasmon polariton coupling by a grating at a metal/dielectric interface. The metallic film is on the bottom surface of the silica substrate. Light is incident normally from above on the coupling grating [9].	18
Figure 2.7: Visualization of localized surface plasmons (under the silver grating) and surface plasmons (on the silver grating) under the TM polarized normal-incident illumination at $\lambda=510\text{nm}$. The incident light is normal to the structure (shown with arrow). Unit cell of the structures is visualized in the electric field profiles.	19

Figure 2.8: Metallic nanoparticles embedded on top of absorbing material to excite the plasmon modes at metal/dielectric interface (plasmonic photovoltaics type 1) [4].	21
Figure 2.9: Metallic nanoparticles embedded in absorbing material to excite the plasmon modes around the metal nanoparticles (plasmonic photovoltaics type 2) [4].	22
Figure 2.10: Metallic periodic structures integrated with the backcontact (plasmonic photovoltaics type 3) [4].	22
Figure 2.11: A screenshot from Lumerical software user interface.	24
Figure 3.1: Cross-sectional view of bilayer heterojunction thin-film organic solar architecture made of glass/ITO/PEDOT:PSS/CuPc/PTCBI/BCP/Ag layers [52].	30
Figure 3.2: Schematic representation of bilayer heterojunction architecture. D stands for donor and A stands for acceptor [44].	31
Figure 3.3: Cross-sectional view of bulk heterojunction thin-film organic solar architecture made of glass/ITO/PEDOT:PSS/P3HT:PCBM/Ag layers [71].	32
Figure 3.4: Schematic representation of a bulk heterojunction architecture. D stands for donor and A stands for acceptor [44].	32
Figure 3.5: Chemical structures of examples of hole-conducting materials that work as electron donor: ZnPC, MDMO-PPV, P3HT, and PFB [44].	34
Figure 3.6: Chemical structures of example of electron-conducting materials that works as electron acceptor materials: Me-Ptcdi, C ₆₀ , CN-MEH-PPV, PCBM, and F8TB [47].	35
Figure 3.7: Absorption coefficients of organic semiconductors commonly used active materials in organic solar cell layers depicted in comparison with the standard AM1.5G solar spectrum [47].	36
Figure 3.8: Schematic device structure for a general organic solar cell. The active layer is sandwiched between two contacts: an indium-tin-oxide electrode coated with a hole transport layer PEDOT:PSS and an top electrode.	36

Figure 3.9: Chemical structure of hole transport layer PEDOT-PSS (poly(3,4-ethylen- dioxythiohene)-polystyrene-para-sulfonic acid) [47].	37
Figure 4.1: Cross-sectional view of the bare (non-metallic) thin-film organic solar cell architecture made of glass/ITO/PEDOT:PSS/P3HT:PCBM/Ag. (Here LT stands for the corresponding layer thickness.).....	41
Figure 4.2: Cross-sectional view of the thin-film organic solar architecture made of glass/ITO/PEDOT:PSS/P3HT:PCBM/Ag with the bottom silver grating. (Here LT stands for layer thickness of the corresponding layer, P indicates the period, w1 denotes the width, and h represents the height of the bottom silver grating.) In our simulations, the illumination is set to be normal to the device structure and the architecture is assumed to be infinite along the x and z axes.	42
Figure 4.3: Cross-sectional view of the thin-film organic solar cell structure made of glass/ITO/PEDOT:PSS/P3HT:PCBM/Ag with the top silver grating. (Here LT stands for layer thickness of the corresponding layer, P indicates the period, and w2 indicates the width of the top silver grating.) In our simulations, the illumination is set to be normal to the device structure and the architecture is assumed to be infinite along the x and z axes.	43
Figure 4.4: Absorption spectra of the organic active material in the bare, bottom grating, and top grating structures under TM-polarized light illumination, computed for the device parameters of P=130 nm, LT1=150 nm, LT2=50 nm, LT3=100 nm, w1=50 nm, w2=50 nm, and h=50 nm.	45
Figure 4.5: Normalized electric field map for the bare organic solar architecture (given in Figure 4.1) under TM-polarized light at $\lambda=550$ nm, computed for the device parameters of P=130 nm, LT1=150 nm, LT2=50 nm, and LT3=100 nm. Only one unit cell of the repeating grating structure is shown in this electric field profile.	47
Figure 4.6: Normalized electric field map for the bare organic solar architecture (given in Figure 4.1) under TM-polarized light at $\lambda=600$ nm, computed for the device parameters of P=130 nm, LT1=150 nm, LT2=50 nm, and	

LT3=100 nm. Only one unit cell of the repeating grating structure is shown in this electric field profile.	47
Figure 4.7: Normalized electric field map for the bottom grating organic solar architecture (given in Figure 4.2) under TM-polarized light at $\lambda=550$ nm, computed for the device parameters of $P=130$ nm, $LT1=150$ nm, $LT2=50$ nm, $LT3=100$ nm, $w1=50$ nm, and $h=50$ nm. Only one unit cell of the repeating grating structure is shown in this electric field profile.	48
Figure 4.8: Normalized electric field map for the bottom grating organic solar architecture (given in Figure 4.2) under TM-polarized light at $\lambda=600$ nm, computed for the device parameters of $P=130$ nm, $LT1=150$ nm, $LT2=50$ nm, $LT3=100$ nm, $w1=50$ nm, and $h=50$ nm. Only one unit cell of the repeating grating structure is shown in this electric field profile.	48
Figure 4.9: Normalized electric field map for the top grating organic solar architecture (given in Figure 4.3) under TM-polarized light at $\lambda=550$ nm, computed for the device parameters of $P=130$ nm, $LT1=150$ nm, $LT2=50$ nm, $LT3=100$ nm, and $w2=50$ nm. Only one unit cell of the repeating grating structure is shown in this electric field profile.	49
Figure 4.10: Normalized electric field map for the top grating organic solar architecture (given in Figure 4.3) under TM-polarized light at $\lambda=600$ nm, computed for the device parameters of $P=130$ nm, $LT1=150$ nm, $LT2=50$ nm, $LT3=100$ nm, and $w2=50$ nm. Only one unit cell of the repeating grating structure is shown in this electric field profile.	49
Figure 4.11: Electric field intensity enhancement within the volume of the organic active material using the bottom grating (given in Figure 4.2) and the top grating (given in Figure 4.3) structures compare to that generated in the bare structure. This field enhancement is computed for TM-polarized light illumination. Using the device parameter of $P=130$ nm, $LT1=150$ nm, $LT2=50$ nm, $LT3=100$ nm, $w1=50$ nm, $w2=50$ nm, and $h=50$ nm.	50
Figure 4.12: Absorption spectra of the organic active material in the bare, bottom grating, and top grating structures under TE-polarized light	

illumination, computed for the device parameter of; P=130 nm, LT1=150 nm, LT2=50 nm, LT3=100 nm, w1=50 nm, w2=50 nm, and h=50 nm.	52
Figure 4.13: Normalized electric field map for the bare organic solar architecture (given in Figure 4.1) under TE-polarized light at $\lambda=600$ nm, computed for the device parameters of P=130 nm, LT1=150 nm, LT2=50 nm, and LT3=100 nm. Only one unit cell of the repeating grating structure is shown in this electric field profile.	53
Figure 4.14: Normalized electric field map for the bottom grating organic solar architecture (given in Figure 4.2) under TE-polarized light at $\lambda=600$ nm, computed for the device parameters of P=130 nm, LT1=150 nm, LT2=50 nm, LT3=100 nm, w1=50 nm, and h=50 nm. Only one unit cell of the repeating grating structure is shown in this electric field profile.	54
Figure 4.15: Normalized electric field map for the top grating organic solar architecture (given in Figure 4.3) under TE-polarized light at $\lambda=600$ nm, computed for the device parameters of P=130 nm, LT1=150 nm, LT2=50 nm, LT3=100 nm, and w2=50 nm. Only one unit cell of the repeating grating structure is shown in this electric field profile.	54
Figure 4.16: Electric field intensity enhancement within the volume of the organic active material using the bottom grating (given in Figure 4.2) and the top grating (given in Figure 4.3) structures compare to that generated in the bare structure. This field enhancement is computed for TE-polarized light illumination. Using the device parameter of P=130 nm, LT1=150 nm, LT2=50 nm, LT3=100 nm, w1=50 nm, w2=50 nm, and h=50 nm.	55
Figure 4.17: Normalized electric field map for the top grating organic solar architecture (given in Figure 4.3) under TE-polarized light at $\lambda=650$ nm, computed for the device parameters of P=130 nm, LT1=150 nm, LT2=50 nm, LT3=100 nm, and w2=50 nm. Only one unit cell of the repeating grating structure is shown in this electric field profile.	56
Figure 4.18: Air mass (AM) 1.5G solar radiation [4].	56
Figure 4.19: Multiplication of AM1.5G solar radiation and overall absorptivity in the volume of the organic active material in the bare, bottom grating, and	

top grating structures compared to the electric field generated in the bare structure, computed for the device parameters of $P=130$ nm, $LT1=150$ nm, $LT2=50$ nm, $LT3=100$ nm, $w1=50$ nm, $w2=50$ nm, and $h=50$ nm.	57
Figure 4.20: Absorption enhancement of backside grating in comparison to the bare device computed for the following parameters: ITO layer thickness $LT1=150$ nm, PEDOT:PSS layer thickness $LT2=50$ nm, P3HT:PCBM layer thickness $LT3=100$ nm, width of bottom grating $w1=50$ nm, and height of the grating $h=50$ nm.	58
Figure 4.21: Normalized absorptivity map of the bare solar cell for comparison. These absorption spectra are computed for the device parameters of $LT1=150$ nm, $LT2=50$ nm, and $LT3=100$ nm.	59
Figure 4.22: Normalized absorptivity map of the bottom metallic grating solar cell as a function of the periodicity of the silver grating under TE-polarized light. Here the absorption spectra are computed for the device parameters of $LT1=150$ nm, $LT2=50$ nm, $LT3=100$ nm, $w1=50$ nm, and $h=50$ nm. ...	60
Figure 4.23: Normalized absorptivity map of the bottom metallic grating solar cell as a function of the periodicity of the silver grating under TM-polarized light. Here the absorption spectra are computed for the device parameters of $LT1=150$ nm, $LT2=50$ nm, $LT3=100$ nm, $w1=50$ nm, and $h=50$ nm. ...	60
Figure 4.24: Normalized absorptivity map of the top metallic grating solar cell as a function of the periodicity of the silver grating under TE-polarized light. Here the absorption spectra are computed for the device parameters of $LT1=150$ nm, $LT2=50$ nm, $LT3=100$ nm, and $w2=50$ nm.	61
Figure 4.25: Normalized absorptivity map of the top metallic grating solar cell as a function of the periodicity of the silver grating under TM-polarized light. Here the absorption spectra are computed for the device parameters of $LT1=150$ nm, $LT2=50$ nm, $LT3=100$ nm, and $w2=50$ nm.	62
Figure 5.1: Cross-sectional view of bare thin-film organic solar architecture (negative control group) made of glass/ITO/PEDOT:PSS/CuPc/PTCBI/BCP/Ag. (Here LT stands for layer	

thickness. Also note that this device cross-section is shown upside down here, with the incident light from the top.)	67
Figure 5.2: Cross-sectional view of thin-film organic solar structure made of glass/ITO/PEDOT:PSS/CuPc/PTCBI/BCP/Ag with the top silver grating. (Here LT stands for layer thickness, P indicates the period, and w1 denotes the width of the top silver grating.) In our simulations, the illumination is set to be normal to the device structure and the architecture is assumed to be infinite along the x and z axes.	68
Figure 5.3: Cross-sectional view of thin-film organic solar structure made of glass/ITO/PEDOT:PSS/CuPc/PTCBI/BCP/Ag with the bottom silver grating. (Here LT stands for layer thickness, P indicates the period, and w2 denotes the width of the bottom silver grating.) In our simulations, the illumination is set to be normal to the device structure and the architecture is assumed to be infinite along the x and z axes.....	68
Figure 5.4: Cross-sectional view of thin-film organic solar architecture made of glass/ITO/PEDOT:PSS/CuPc/PTCBI/BCP/Ag with the volumetric silver gratings (including both the top and bottom metal gratings.)(Here LT stands for layer thickness, P indicates the period of the gratings, and w1 and w2 denote the width of the top and bottom silver grating, respectively.) In our simulations, the illumination is set to be normal to the device structure and the architecture is assumed to be infinite along the x and z axes.	69
Figure 5.5: Normalized electric field profiles for the top silver grating, with the design parameters of P=200 nm (period of the grating), w1=50 nm (width of the top metal grating) under TM-polarized normal-incident illumination at $\lambda=510$ nm. The layer thicknesses of the solar cell are LT1=150 nm (ITO), LT2=20 nm (PEDOT:PSS), LT3=11 nm (CuPC), LT5=4 nm (PTCI), and LT5=12 nm (BCP). The incident light is normal to the device structure. Only one unit cell of the repeating grating structure is shown in this electric field profile.	71

Figure 5.6: Normalized electric field profiles for the bottom silver grating, with the design parameters of $P=200$ nm (period of the grating) $w_2=30$ nm (width of the bottom metal grating) under TM-polarized normal-incident illumination at $\lambda=510$ nm. The layer thicknesses of the solar cell are $LT_1=150$ nm (ITO), $LT_2=20$ nm (PEDOT:PSS), $LT_3=11$ nm (CuPC), $LT_4=4$ nm (PTCl), and $LT_5=12$ nm (BCP). The incident light is normal to the device structure. Only one unit cell of the repeating grating structure is shown in this electric field profile. 72

Figure 5.7: Normalized electric field profiles for the volumetric plasmonic resonator (including both the top and bottom silver gratings), with the design parameters of $P=200$ nm (period of the grating), $w_1=50$ nm (width of the top metal grating), and $w_2=30$ nm (width of the bottom metal grating) under TM-polarized normal-incident illumination at $\lambda=510$ nm. The layer thicknesses of the solar cell are $LT_1=150$ nm (ITO), $LT_2=20$ nm (PEDOT:PSS), $LT_3=11$ nm (CuPC), $LT_4=4$ nm (PTCl), and $LT_5=12$ nm (BCP). The incident light is normal to the structure. Only one unit cell of the repeating grating structure is shown in this electric field profile. 73

Figure 5.8: Absorption spectra of the four solar cell architectures (bare, bottom grating, top grating, and volumetric design) with the design parameters of $P=200$ nm (period of the grating), $w_1=50$ nm (width of the top metal grating), and $w_2=30$ nm (width of the bottom metal grating), under TM-polarized normal-incident illumination. The layer thicknesses of the solar cells are $LT_1=150$ nm (ITO), $LT_2=20$ nm (PEDOT:PSS), $LT_3=11$ nm (CuPC), $LT_4=4$ nm (PTCBl), and $LT_5=12$ nm (BCP). 75

Figure 5.9: Absorption spectra of the four solar cell architectures (bare, bottom grating, top grating, and volumetric design) with the design parameters of $P=200$ nm (period of the grating), $w_1=50$ nm (width of the top metal grating), and $w_2=30$ nm (width of the bottom metal grating), under TE-polarized normal-incident illumination. The layer thicknesses of the solar cells are $LT_1=150$ nm (ITO), $LT_2=20$ nm (PEDOT:PSS), $LT_3=11$ nm (CuPC), $LT_4=4$ nm (PTCBl), and $LT_5=12$ nm (BCP). 75

Figure 5.10: Overall absorption $(A_{TM}+A_{TE})/2$ spectra of the four solar cell architectures (bare, bottom grating, top grating, and volumetric design) with the design parameters of $P=200$ nm (period of the grating), $w_1=50$ nm (width of the top metal grating), and $w_2=30$ nm (width of the bottom metal gratings). The layer thicknesses of the solar cells are $LT_1=150$ nm (ITO), $LT_2=20$ nm (PEDOT:PSS), $LT_3=11$ nm (CuPC), $LT_4=4$ nm (PTCBI) and $LT_5=12$ nm (BCP)..... 76

Figure 5.11: AM1.5G solar irradiance spectrum [4]..... 78

Figure 5.12: Normalized absorptivity map of the bare solar cell for comparison. These absorption spectra are computed for the parameters of $LT_1=150$ nm, $LT_2=20$ nm, $LT_3=11$ nm, $LT_4=4$ nm and $LT_5=12$ nm..... 80

Figure 5.13: Normalized absorptivity map of only the bottom metallic grating solar cell as a function of the periodicity of the silver grating under TE-polarized light. Here the absorption spectra are computed for the device parameters of $w_2=30$ nm, $LT_1=150$ nm, $LT_2=20$ nm, $LT_3=11$ nm, $LT_4=4$ nm, and $LT_5=12$ nm. 80

Figure 5.14: Normalized absorptivity map of only the bottom metallic grating solar cell as a function of the periodicity of the silver grating under TM-polarized light. Here the absorption spectra are computed for the device parameters of $w_2=30$ nm, $LT_1=150$ nm, $LT_2=20$ nm, $LT_3=11$ nm, $LT_4=4$ nm, and $LT_5=12$ nm. 81

Figure 5.15: Normalized absorptivity map of only the top metallic grating solar cell as a function of the periodicity of the silver grating under TE-polarized light. Here the absorption spectra are computed for the device parameters of $w_1=50$ nm, $LT_1=150$ nm, $LT_2=20$ nm, $LT_3=11$ nm, $LT_4=4$ nm, and $LT_5=12$ nm. 81

Figure 5.16: Normalized absorptivity map of only the top metallic grating solar cell as a function of the periodicity of the silver grating under TM-polarized light. Here the absorption spectra are computed for the device parameters of $w_1=50$ nm, $LT_1=150$ nm, $LT_2=20$ nm, $LT_3=11$ nm, $LT_4=4$ nm, and $LT_5=12$ nm. 82

Figure 5.17: Normalized absorptivity map of volumetric metallic gratings solar cell as a function of the periodicity of the silver grating under TE-polarized light. Here the absorption spectra are computed for the device parameters of $w_1=50$ nm, $w_2=30$ nm, $LT_1=150$ nm, $LT_2=20$ nm, $LT_3=11$ nm, $LT_4=4$ nm, and $LT_5=12$ nm.	82
Figure 5.18: Normalized absorptivity map of volumetric metallic gratings solar cell as a function of the periodicity of the silver grating under TM-polarized light. Here the absorption spectra are computed for the device parameters of $w_1=50$ nm, $w_2=30$ nm, $LT_1=150$ nm, $LT_2=20$ nm, $LT_3=11$ nm, $LT_4=4$ nm, and $LT_5=12$ nm.	83
Figure 5.19: Normalized absorptivity map of only the top metallic grating solar cell as a function of the periodicity of the silver grating under TE-polarized light. Here the absorption spectra are computed for the device parameters of $w_1=60$ nm, $LT_1=150$ nm, $LT_2=20$ nm, $LT_3=11$ nm, $LT_4=4$ nm, and $LT_5=12$ nm.	83
Figure 5.20: Normalized absorptivity map of only the top metallic grating solar cell as a function of the periodicity of the silver grating under TM-polarized light. Here the absorption spectra are computed for the device parameters of $w_1=60$ nm, $LT_1=150$ nm, $LT_2=20$ nm, $LT_3=11$ nm, $LT_4=4$ nm, and $LT_5=12$ nm.	84
Figure 5.21: Normalized absorptivity map of volumetric metallic gratings solar cell as a function of the periodicity of the silver grating under TE-polarized light. Here the absorption spectra are computed for the device parameters of $w_1=60$ nm, $w_2=30$ nm, $LT_1=150$ nm, $LT_2=20$ nm, $LT_3=11$ nm, $LT_4=4$ nm, and $LT_5=12$ nm.	84
Figure 5.22: Normalized absorptivity map of volumetric metallic gratings solar cell as a function of the periodicity of the silver grating under TM-polarized light. Here the absorption spectra are computed for the device parameters of $w_1=60$ nm, $w_2=30$ nm, $LT_1=150$ nm, $LT_2=20$ nm, $LT_3=11$ nm, $LT_4=4$ nm, and $LT_5=12$ nm.	85

Figure 5.23: Normalized absorptivity map of only the top metallic grating solar cell as a function of the periodicity of the silver grating under TE-polarized light. Here the absorption spectra are computed for the device parameters of $w_1=40$ nm, $LT_1=150$ nm, $LT_2=20$ nm, $LT_3=11$ nm, $LT_4=4$ nm, and $LT_5=12$ nm. 85

Figure 5.24: Normalized absorptivity map of only the top metallic grating solar cell as a function of the periodicity of the silver grating under TM-polarized light. Here the absorption spectra are computed for the device parameters of $w_1=40$ nm, $LT_1=150$ nm, $LT_2=20$ nm, $LT_3=11$ nm, $LT_4=4$ nm, and $LT_5=12$ nm. 86

Figure 5.25: Normalized absorptivity map of volumetric metallic gratings solar cell as a function of the periodicity of the silver grating under TE-polarized light. Here the absorption spectra are computed for the device parameters of $w_1=40$ nm, $w_2=30$ nm, $LT_1=150$ nm, $LT_2=20$ nm, $LT_3=11$ nm, $LT_4=4$ nm, and $LT_5=12$ nm. 86

Figure 5.26: Normalized absorptivity map of volumetric metallic gratings solar cell as a function of the periodicity of the silver grating under TM-polarized light. Here the absorption spectra are computed for the device parameters of $w_1=40$ nm, $w_2=30$ nm, $LT_1=150$ nm, $LT_2=20$ nm, $LT_3=11$ nm, $LT_4=4$ nm, and $LT_5=12$ nm. 87

List of Tables

Table 3.1: Confirmed solar cell architectures and their corresponding measured efficiencies under the AM1.5G solar spectrum at 25°C. This table considers the latest and the highest achieved efficiency values considering both organic and inorganic solar cell architectures which is published annually by Green M. et al. This table is taken from “Solar cell efficiency tables (version 35)” published in 2010 [45]..... 28

To Gülendäm, Atila and Yavuz Selim Sefünç

Chapter 1

Introduction

Today climate change, also referred to as global warming by some scientists, is considered to be one of the most challenging problems that humankind faces in this century according to some scientific committees [1,2]. It is important to identify the sources of climate change in order to innovate proper solutions to mitigate the causes and negative effects on humankind and on Earth. Nanotechnology, especially nanophotonics, can offer some potential solutions to help combating with climate change from various aspects such as decreasing the global energy power consumption by solid state lighting, reducing environmental and biological pollution by photocatalytic nanomaterials, and producing alternative energy in a renewable, e.g., by photovoltaics.

Photovoltaics is potentially a promising technology for producing electricity possibly on a medium-large scale [3]. In 2008, approximate global electricity production capacity via photovoltaics was 5 GW and by 2015 this production is foresighted to be in order of 20 GW, which is yet a fraction of global electricity demand [4]. Photovoltaics seems to be a good candidate to remedy the energy

problem in the world only if the cost of photovoltaics is reduced or the efficiency of photovoltaics is increased by a factor of 2-5 to be competitive with today's fossil fuel based energy production [4]. For that, new generation thin film solar cells are designed to feature very thin layers of active (absorbing) materials in the order of tens of nanometers in thickness. Although this approach may decrease the cost of solar cells possibly to reasonable levels, these ultra-thin absorbing layers ruinously suffer from low total optical absorption of incident photons. To address this problem, there has been a great interest in designing plasmonic structures to enhance the total optical absorption in the active layers of these thin-film solar cells [4,5].

Plasmonics is one of the leading research topics of the fascinating field of nanophotonics, which investigates how electromagnetic waves can be confined in metallic architectures in order of or much more smaller than their wavelength, among other things. The interaction between electromagnetic waves and conducting electrons at a metallic interface result in a field localization. This near field enhancement can be benefited in different photonic applications including plasmonic waveguides, nanoscale optical antennas, plasmon-assisted surface-enhanced sensing, plasmonic integrating circuits, plasmonic lasers, metallic apertures for extraordinary transmission, plasmonic optical emitters, materials with negative refractive index, and plasmon-resonance enhanced solar cells [6-9].

Recent research efforts on improving the absorption behavior of organic and inorganic solar cells via exciting plasmonic modes have attracted significant attention all around the world [4,5]. In the literature, generally three ways of enhancing the optical absorption in solar cells are studied: (1) metallic nanoparticles or periodic structures integrated on top of the absorbing material to excite the plasmon modes and couple the incoming light into the thin-film absorbing layer [4,5,10-28,31,32], (2) metallic nanoparticles integrated into the absorbing layer to use them as a sub-wavelength antennas that enhance the

optical absorption with near-field plasmonic field localization [4,29-31,33,37], and (3) metallic periodic structures and random metallic nanoparticles placed on the backcontact surface to use surface plasmon polaritons excited at metal/dielectric interface and enhance the optical absorption with supported surface plasmon polaritons modes at this interface [4,34-36,38-42]. Generally these architecture ideas are based on placing only single resonators at the top, in the middle, or at the bottom of active layers for exciting plasmon modes. Nevertheless, there is a need for innovative design that utilizes the volume of the active layer of the thin-film solar cell and achieves higher enhancement levels beyond the reported values to date.

In this thesis, different than the previous works of our group and others, we propose and demonstrate a new design concept of volumetric plasmonic resonator that relies on the idea of coupling two layers of plasmonic structures embedded in an organic solar cell. For this, here we incorporate one silver grating on the top of the absorbing layer and another at the bottom of the active layer to couple them with each other such that field localization is further increased and extended within the volume of the active material between gratings. In addition to individual plasmonic resonances of these metallic structures, this allows for the vertical interaction in the volumetric resonator. This interaction contributes to further enhancement of total optical absorption in the active layer, beyond the limited photon absorption in non-metallic (bare) organic solar cell. Our results show that this architecture exhibits a substantial absorption enhancement performance particularly under the transverse magnetic (TM) polarized illumination, while the optical absorption is maintained at a similar level under the transverse electric (TE) polarized illumination. As a result, the optical absorption in the active layer is enhanced up to ~67% under AM1.5G (air mass (1.5) global) solar radiation.

Also in this thesis, we study the effect of periodic grating placed on top of backcontact in a P3HT:PCBM based solar cell for the first time. In the previous

reports, there are various types of metallic architectures that have been shown to enhance the absorption of solar cell active layers [4,34-36,38-42]. However it is challenging to make plasmonic structures that achieve high enough absorption enhancement under both transverse electromagnetic and transverse magnetic polarizations. Using a silver periodic metallic grating structure in P3HT:PCBM based organic solar cell, we achieve a ~21% performance enhancement under AM1.5G solar radiation compared to the bare device even when the active material is replaced by metallic gratings and no additional active layer is added.

In this thesis work, we proved our proposed concepts computationally and showed our numerical results based on finite-difference time-domain (FDTD) method simulations. The FDTD method is currently the state-of-the-art numerical method for solving Maxwell's curl equations in time domain on discretized spatial grids [55-56]. This method allows us to use experimentally measured complex dielectric constant of materials in the definition of the materials and simulate designed complex geometries.

This thesis is organized as follows. In Chapter 1, we begin with a brief introduction on plasmonic solar cells and explain our motivation. We discuss the issues of today's solar cells and plasmonic approaches reported in the literature to overcome this problem. Our proposed solutions are presented, which rely on enhancing the optical absorption of solar cells via plasmonics in new architectures. In Chapter 2, we present the technical background and basic concepts on plasmonics including basics of surface plasmons and basics of localized surface plasmons. We review the plasmonic resonator approaches in the literature for solar cells. Also in this chapter, we make an introduction to the FDTD method and show the basics of numerical simulation in Lumerical Software. In Chapter 3, we introduce the principles of organic photovoltaics including general architecture of organic solar cells, their operation principles and materials commonly used in fabrication of thin-film solar cells. In Chapter 4, we present periodic metal grating placed on top of backcontact in a

P3HT:PCBM based solar cell for enhanced absorption in both polarizations (TE and TM). We present the numerical results of our FDTD simulations. In Chapter 5, we present our new volumetric design concept based on using two coupled plasmonic resonators placed vertically in single organic solar cells. We also present the absorptivity and optimization results of these organic solar cells based on volumetric plasmonic resonators. In Chapter 6, we summarize the proposed plasmonic structures and their proof-of-concept demonstrations based on FDTD modeling.

Chapter 2

Fundamentals of Plasmonics

Plasmonics is a subfield of nanophotonics, which mainly focuses on how electromagnetic field interacts with metals in the order of or smaller than the wavelength. The extraordinary consequences of the interaction between the light and metal are described by the surface plasmon theory [6-9].

In this chapter, we start our discussion with a short history of plasmonics. We then continue with discussing surface plasmons and localized surface plasmons. We also explain the application of plasmonics in photovoltaics and provide a brief description on finite-difference time-domain simulations, which is a useful, simple tool for understanding the effect of plasmonics and a widely used simulation technique in this thesis.

In early times, the technique of coloring stain glasses by very small gold and silver particles was known to Romans. The first application of surface plasmons in the history is the famous Lycurgus Cup (4th century A.D.), shown in Figure 2.1, which changes its color depending on the illumination from inside or

outside. When viewed in reflected light with illumination from outside, for example, in daylight, it appears green. However, when a light is shone into the cup and transmitted through the glass, it appears red. Nowadays it is known that the coloration of the cup is determined by the frequency of surface plasmon resonance in metallic nanoparticles embedded into the glass [9].



Figure 2.1: Lycurgus Cup (4th century A.D.) under different illuminations from outside (left) and inside (right) in British Museum (retrieved from the webpage http://www.britishmuseum.org/explore/highlights/highlight_objects/pe_mla/t/the_lycurgus_cup.aspx).

Some of the first scientific studies on surface plasmons started in the beginning of the twentieth century. Robert W. Wood, an American physicist, noticed an inexplicable reflection caused by metallic gratings in 1902. In 1904, Maxwell Garnett worked on understanding the reason behind the observed vivid colors in metal nanoparticle doped glasses using the Drude model that explains the transport properties of electrons in metals derived by Paul Drude. In Maxwell Garnett's work, the electromagnetic properties of tiny metal spheres were studied using Lord Rayleigh's approaches. The further understanding on surface

plasmons continued with Gustav Mie's theory on light scattering properties of spherical particles in 1908 [8,9].

After some years, the research on surface plasmons continued with David Pines by describing the oscillations of free electrons travelling around the metals in 1956. In this work, "plasmons" term was articulated for the first time in science in the description of plasma oscillations in gas discharges. In mid 1950s, the pioneering work of Rufus Ritchie, published in *Physics Letters* by the title "Plasma losses by fast electrons in thin films", is the first paper that recognized the surface plasmons in the field of surface science by introducing a theoretical description of these collective oscillations. Following this step, localized plasmons were exhibited by Rufus Ritchie in 1973; by Martin Fleischmann et al. in 1974 and by Martin Moskovits in 1985. The introduction of plasmonics into engineered nanostructure started with Thomas Ebbesen in 1998 with a demonstration of extraordinary light transmission through subwavelength holes, which has subsequently boosted scientific research on plasmonics [8,9]. Today, plasmonics is applied to different photonic device architectures including waveguides, optical data storage devices, biological sensors, and solar cells, typically to improve their device performance beyond the limits [6-9].

2.1 Surface Plasmons

Surface plasmons (SPs) are electromagnetic waves that propagate along the surface of a conductor, usually a noble metal such as Au, Ag, and Al, while evanescently confined in the perpendicular direction. The free charges in the metal make collective oscillations at the metal/dielectric interface due to excitation of incident photons. SPs receive strong interest with the recent advances in technology that has started to allow metals to be shaped and characterized at nanometer scales. Shaping the nanostructures enables us to

control the properties of SPs to disclose new aspects of its usage and open new applications [6-9].



Figure 2.2: Dielectric/metal interface considered in the dispersion relation derivation of surface plasmons. The structure is omitted to be infinite in y direction [7].

The basic theory behind the surface plasmons can be described on a flat metal/dielectric interface, as depicted in Figure 2.2. We know that the interaction between metals and electromagnetic waves can be described by fundamental Maxwell's equations. However, in plasmonics, and also in our structures, we consider metallic structures in the order of few nanometers. Even when we go down to this small scale, classical Maxwell equations are capable of describing the interaction between metal and electromagnetic waves, since the high density of free carriers results in minute spacings of the electron energy levels compared to thermal excitations of energy $k_B T$ at room temperature. All metal structures described in this thesis fall within the domain of classical Maxwell's theory. Thus, we start our derivation by stating the Maxwell equations [7]. Basic Maxwell's equations of macroscopic electromagnetism are given as:

$$\nabla \cdot \mathbf{D} = \rho_{ext} \quad (2.1)$$

$$\nabla \cdot \mathbf{B} = 0 \quad (2.2)$$

$$\nabla \times \mathbf{E} = -\frac{d\mathbf{B}}{dt} \quad (2.3)$$

$$\nabla \times \mathbf{H} = \mathbf{J}_{ext} + \frac{d\mathbf{D}}{dt} \quad (2.4)$$

where \mathbf{D} is the dielectric displacement, \mathbf{E} is the electric field, \mathbf{H} is the magnetic field, \mathbf{B} is the magnetic induction (or magnetic flux density), ρ_{ext} is the external charge, and \mathbf{J}_{ext} is the external current density. In this representation, we represent the external charge and current densities ($\rho_{ext}, \mathbf{J}_{ext}$) and the internal charge and current densities (ρ, \mathbf{J}) as:

$$\rho_{tot} = \rho_{ext} + \rho \quad (2.5)$$

$$\mathbf{J}_{tot} = \mathbf{J}_{ext} + \mathbf{J} \quad (2.6)$$

The relations between the four macroscopic fields ($\mathbf{D}, \mathbf{B}, \mathbf{E}, \mathbf{H}$) and the polarization \mathbf{P} and magnetization \mathbf{M} are given as:

$$\mathbf{D} = \epsilon_0 \mathbf{E} + \mathbf{P} \quad (2.7)$$

$$\mathbf{H} = \frac{1}{\mu_0} \mathbf{B} - \mathbf{M} \quad (2.8)$$

where ϵ_0 is the electric permittivity and μ_0 is the magnetic permeability of vacuum.

To determine the spatial field profile and dispersion of propagating waves, we need explicit expressions for the different field components of \mathbf{E} and \mathbf{H} . This can be achieved via using the curl equations given in (2.3) and (2.4).

Equation (2.3) can be rewritten as:

$$\nabla \times \mathbf{E} = i\omega \mathbf{B} = i\omega \mu_0 \mathbf{H} \quad (2.9)$$

where $\frac{\partial}{\partial t} = -i\omega$ harmonic time dependence, which then yields:

$$\left(\hat{a}_x \frac{\partial}{\partial x} + \hat{a}_y \frac{\partial}{\partial y} + \hat{a}_z \frac{\partial}{\partial z} \right) x (\hat{a}_x E_x + \hat{a}_y E_y + \hat{a}_z E_z) = i\omega\mu_0 \mathbf{H} \quad (2.10)$$

The explicit expressions for E fields along x, y and z direction lead to:

$$\frac{\partial E_z}{\partial y} - \frac{\partial E_y}{\partial z} = i\omega\mu_0 H_x \quad (2.11)$$

$$\frac{\partial E_x}{\partial z} - \frac{\partial E_z}{\partial x} = i\omega\mu_0 H_y \quad (2.12)$$

$$\frac{\partial E_y}{\partial x} - \frac{\partial E_x}{\partial y} = i\omega\mu_0 H_z \quad (2.13)$$

Similarly, (2.4) can be rewritten as:

$$\nabla \times \mathbf{H} = i\omega \mathbf{D} = -i\omega \varepsilon_0 \varepsilon \mathbf{E} \quad (2.14)$$

$$\left(\hat{a}_x \frac{\partial}{\partial x} + \hat{a}_y \frac{\partial}{\partial y} + \hat{a}_z \frac{\partial}{\partial z} \right) x (\hat{a}_x H_x + \hat{a}_y H_y + \hat{a}_z H_z) = i\omega \varepsilon_0 \varepsilon \mathbf{E} \quad (2.15)$$

The explicit expressions for E fields along x, y and z direction yield:

$$\frac{\partial H_z}{\partial y} - \frac{\partial H_y}{\partial z} = -i\omega \varepsilon_0 \varepsilon E_x \quad (2.16)$$

$$\frac{\partial H_x}{\partial z} - \frac{\partial H_z}{\partial x} = -i\omega \varepsilon_0 \varepsilon E_y \quad (2.17)$$

$$\frac{\partial H_y}{\partial x} - \frac{\partial H_x}{\partial y} = -i\omega \varepsilon_0 \varepsilon E_z \quad (2.18)$$

For waves propagating in x-direction, setting $\frac{\partial}{\partial x} = i\beta$, and assuming homogeneity in the y-direction, setting $\frac{\partial}{\partial y} = 0$, the equations simplify into:

$$-\frac{\partial E_y}{\partial z} = i\omega\mu_0 H_x \quad (2.19)$$

$$\frac{\partial E_x}{\partial z} - i\beta E_z = i\omega\mu_0 H_y \quad (2.20)$$

$$i\beta E_y = i\omega\mu_0 H_z \quad (2.21)$$

$$\frac{\partial H_y}{\partial z} = i\omega\varepsilon_0\varepsilon E_x \quad (2.22)$$

$$\frac{\partial H_x}{\partial z} - i\beta H_z = -i\omega\varepsilon_0\varepsilon E_y \quad (2.23)$$

$$i\beta H_y = -i\omega\varepsilon_0\varepsilon E_z \quad (2.24)$$

For TM mode, these equations (2.19-2.24) reduce to:

$$E_x = -i \frac{1}{\omega\varepsilon_0\varepsilon} \frac{\partial H_y}{\partial z} \quad (2.25)$$

$$E_z = -\frac{\beta}{\omega\varepsilon_0\varepsilon} H_y \quad (2.26)$$

and the wave equation for TM mode becomes

$$\frac{\partial^2 H_y}{\partial z^2} + (k_0^2\varepsilon - \beta^2)H_y = 0 \quad (2.27)$$

For TE mode, these equations (2.19-2.24) boil down to:

$$H_x = i \frac{1}{\omega\mu_0} \frac{\partial E_y}{\partial z} \quad (2.28)$$

$$H_z = \frac{\beta}{\omega\mu_0} E_y \quad (2.29)$$

and the wave equation for TE mode becomes

$$\frac{\partial^2 E_y}{\partial z^2} + (k_0^2\varepsilon - \beta^2)E_y = 0 \quad (2.30)$$

Now we consider the starting simple planar geometry, given in Figure 2.2, sustaining surface plasmon polaritons, based on a single, flat interface between a nonabsorbing dielectric layer with a real dielectric constant ε_2 and a metal layer with a dielectric function that depends on frequency, $\varepsilon_1(\omega)$. Let us first look at TM solutions of surface plasmons for this geometry. In metal (for $z < 0$),

$$H_y(z) = A_2 e^{i\beta x} e^{-k_2 z} \quad (2.31)$$

$$E_x(z) = iA_2 \frac{1}{\omega \varepsilon_0 \varepsilon_2} k_2 e^{i\beta x} e^{-k_2 z} \quad (2.32)$$

$$E_z(z) = -A_1 \frac{\beta}{\omega \varepsilon_0 \varepsilon_2} e^{i\beta x} e^{-k_2 z} \quad (2.33)$$

In dielectric (for $z > 0$),

$$H_y(z) = A_1 e^{i\beta x} e^{k_1 z} \quad (2.34)$$

$$E_x(z) = -iA_1 \frac{1}{\omega \varepsilon_0 \varepsilon_1} k_1 e^{i\beta x} e^{k_1 z} \quad (2.35)$$

$$E_z(z) = -A_1 \frac{\beta}{\omega \varepsilon_0 \varepsilon_1} e^{i\beta x} e^{k_1 z} \quad (2.36)$$

At the boundary ($z=0$), H_y and E_x for metal and dielectric must be equal to each other due to continuity. Thus, the equality yields:

$$A_2 e^{i\beta x} e^{-k_2 z} \Big|_{z=0} = A_1 e^{i\beta x} e^{k_1 z} \Big|_{z=0} \quad (2.37)$$

$$A_2 = A_1 \quad (2.38)$$

$$iA_2 \frac{1}{\omega \varepsilon_0 \varepsilon_2} k_2 e^{i\beta x} e^{-k_2 z} \Big|_{z=0} = -iA_1 \frac{1}{\omega \varepsilon_0 \varepsilon_1} k_1 e^{i\beta x} e^{k_1 z} \Big|_{z=0} \quad (2.39)$$

$$A_2 \frac{k_2}{\varepsilon_2} = -A_1 \frac{k_1}{\varepsilon_1} \quad (2.40)$$

$$\frac{k_2}{\varepsilon_2} = -\frac{k_1}{\varepsilon_1} \quad (2.41)$$

This condition must be satisfied for SPs to exist. This condition is satisfied only at the interfaces between materials with opposite signs of the real part of their dielectric permittivities such as metal and dielectric. Surface plasmons are visualized in Figure 2.3 for TM polarized illumination.

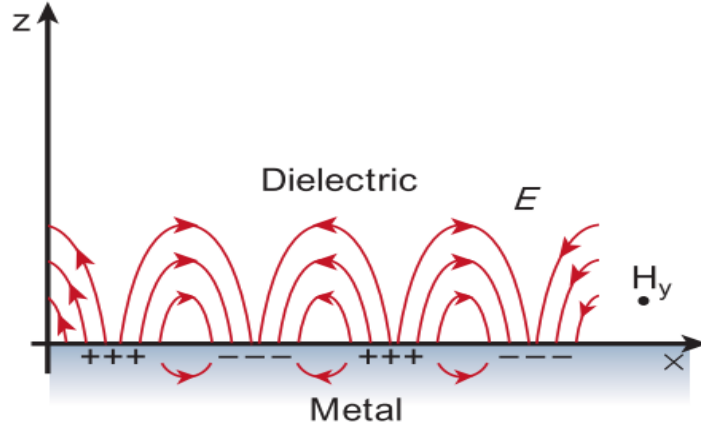


Figure 2.3: Visualization of surface plasmons at the metal/dielectric interface: the surface charge oscillations in the transverse magnetic (TM) case, while the magnetic field (\mathbf{H}) is in the y-direction and the electric field (\mathbf{E}) is normal to the surface [6].

The TM solutions for $H_y(z)$ given in (2.31) and (2.34) must satisfy the wave equation for TM modes given in (2.27), which gives the conditions of,

$$k_1^2 = \beta^2 - k_0^2 \epsilon_1 \quad (2.42)$$

$$k_2^2 = \beta^2 - k_0^2 \epsilon_2 \quad (2.43)$$

After solving the Maxwell equations with proper boundary conditions, the resonant interaction between the surface charge oscillation and the light illumination – electromagnetic field – is given as:

$$\beta = k_{SP} = k_0 \sqrt{\frac{\epsilon_1 \epsilon_2}{\epsilon_1 + \epsilon_2}} \quad (2.44)$$

where k_{SP} is the dispersion relation of surface plasmons propagating at the metal/dielectric interface and ϵ_1 and ϵ_2 are the frequency dependent permittivity of the metal and real dielectric permittivity constant of the dielectric medium, respectively. This condition is satisfied for metals because the dielectric function (ϵ_1) is both complex and negative. The dispersion relation shown in Figure 2.4

demonstrates that the SP mode always lies beyond the light line; that is, SP mode has a greater momentum (k_{sp}) than a free space photon (k_0) of the same frequency ω . Therefore, there exists a momentum mismatch, which prevents free-space light from directly being coupled into a SP mode. This is the first consequence of the interaction between electromagnetic field and surface charges.

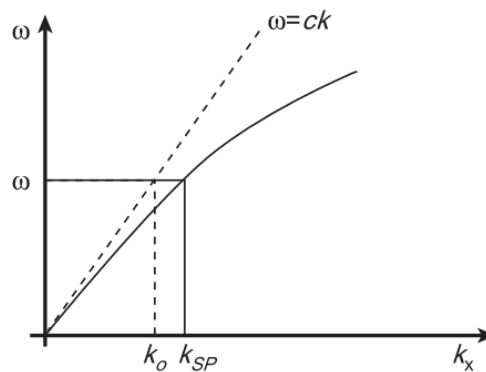


Figure 2.4: Dispersion relation for existing surface plasmons [6].

The second consequence is that the field near dielectric/metal interface decreases exponentially with the distance from the surface (Figure 2.5). The field in the perpendicular direction has evanescent behavior due to nonradiative nature of SPs, which prevents power from propagating away from the surface.

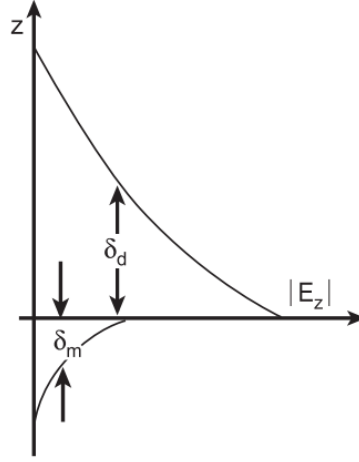


Figure 2.5: The electric field profile at the dielectric/metal interface. δ_d is the decay length of the field in dielectric medium and δ_m is the decay length of the field in metal medium [6].

In the literature, three main techniques are used to overcome the momentum mismatch problem. The first approach is to use a prism coupling setup to modify the momentum of the incident light. The second approach uses topological defects on the surface such as subwavelength holes and grids, which provide a convenient way to generate SPs locally. The third approach is based on using a periodic corrugation in the metal, e.g., metal gratings, which constitutes the main idea of our plasmonic resonator design in organic solar cells in this thesis [6].

Previously, we considered TM solution of SPs. Let us now look at TE solutions of surface plasmons.

In metal (for $z < 0$),

$$E_y(z) = A_2 e^{i\beta x} e^{-k_2 z} \quad (2.45)$$

$$H_x(z) = -iA_2 \frac{1}{\omega\mu_0} k_2 e^{i\beta x} e^{-k_2 z} \quad (2.46)$$

$$H_z(z) = A_2 \frac{\beta}{\omega\mu_0} e^{i\beta x} e^{-k_2 z} \quad (2.47)$$

In dielectric (for $z>0$),

$$E_y(z) = A_1 e^{i\beta x} e^{k_1 z} \quad (2.48)$$

$$H_x(z) = iA_1 \frac{1}{\omega\mu_0} k_1 e^{i\beta x} e^{k_1 z} \quad (2.49)$$

$$H_z(z) = A_1 \frac{\beta}{\omega\mu_0} e^{i\beta x} e^{k_1 z} \quad (2.50)$$

At the boundary ($z=0$), H_x and E_y for metal and dielectric must be equal to each other due to continuity. Thus, the equality leads to:

$$A_1(k_1+k_2) = 0 \quad (2.51)$$

$$A_1 = A_2 \quad (2.52)$$

Since the $\text{Re}\{k_1\}$ and $\text{Re}\{k_2\}$ is greater than 0, this condition is only satisfied for the case of $A_1=0$. Thus no surface plasmon mode exists under TE polarization. Surface plasmons only exist under TM polarized illumination [7].

From solar cell point of view, the surface plasmons are beneficial for efficient light absorption if the absorption of the surface plasmons in the semiconductor is stronger than in the metal (Figure 2.6). When we satisfy this condition, the surface plasmon resonances produce a very strong and stable charge displacement and also light concentration at the dielectric interface. The dielectric layer is made of an absorbing material in our case. Large field increases in the absorbing material contributes to total optical absorption, which is given by:

$$\text{Absorption} = \omega * \text{Im}(\varepsilon) \oint_V |E|^2 dV' \quad (2.53)$$

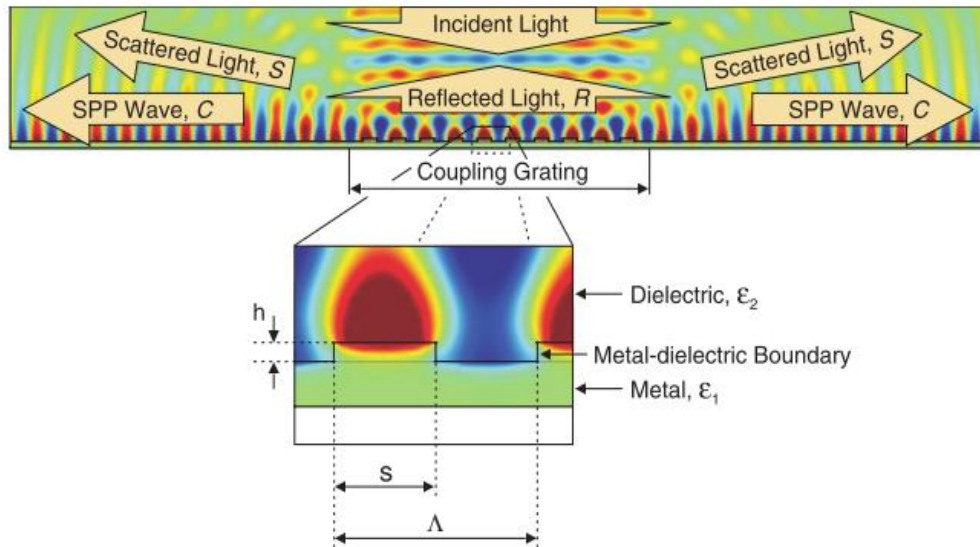


Figure 2.6: Field profile of light-to-surface plasmon polariton coupling by a grating at a metal/dielectric interface. The metallic film is on the bottom surface of the silica substrate. Light is incident normally from above on the coupling grating [9].

2. 2 Localized Surface Plasmons

We have seen that surface plasmons are propagating electromagnetic waves at the metal and dielectric interface. These are propagating, dispersive electromagnetic waves that occur when the surface plasmon momentum condition is satisfied. Localized surface plasmons, or localized plasmons, are simply non-propagating resonances that occur both in the near-field and inside the conductor due to excitation of the conductor free electrons with the incident electromagnetic wave. As a consequence of curved surfaces and sufficient penetration depth, localized surface plasmon resonances can be formed by direct light illumination, in contrast to propagating surface plasmon resonances. Thus, the localized surface plasmons can be excited under TE and TM illumination [7].

If these resonances – also called as field amplification – occur in the absorbing material, the absorptivity of the active material increases. Localized surface

plasmon based absorption enhancement is observed in solar cell architectures where the metallic plasmonic resonators are placed on top of the absorbing layer. The interaction between the electromagnetic wave and the metal resonator causes great field amplification under the resonating structure, which is mainly an absorbing material. In one of our simulation outputs, it is possible to observe the localized surface plasmons and surface plasmon polaritons due to excitation of plasmon modes in metallic grating structure (Figure 2.7). The field amplification that takes place under the metallic grating is localized in the active material, and as a result, enhancement in absorptivity is observed.

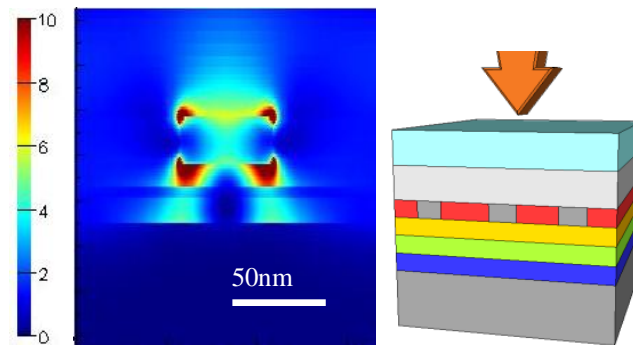


Figure 2.7: Visualization of localized surface plasmons (under the silver grating) and surface plasmons (on the silver grating) under the TM polarized normal-incident illumination at $\lambda=510\text{nm}$. The incident light is normal to the structure (shown with arrow). Unit cell of the structures is visualized in the electric field profiles.

2.3 Plasmonics for Photovoltaics

The recent research efforts on increasing the optical absorption of organic and inorganic solar cells via exciting plasmonic modes have attracted significant attention all around the world [4,5]. In the literature, generally three ways of enhancing the optical absorption in the solar cells are studied: 1.) metallic nanoparticles or metallic periodic gratings placed on top of absorbing material to

excite the plasmon modes and couple the incoming light into the thin-film absorbing (plasmonic photovoltaics type 1). These nano-metallic structures excite plasmon modes at different wavelengths and are tailored to particular frequencies by engineering the architecture geometry [4,5,10-28,31,32]. 2.) The second method is to integrate metallic nanoparticles into absorbing layer to use them as sub-wavelength antennas, which enhance the optical absorption with near-field plasmonic field increase [4,29-31,33,37] (plasmonic photovoltaics type 2). 3.) Metallic periodic structures and random metallic nanoparticles on the backcontact surface to use surface plasmon polariton excited at metal/dielectric interface and enhance the optical absorption with supported surface plasmon polariton modes at this interface [4,34-36,38-42] (plasmonic photovoltaics type 3). Generally these architecture ideas are based on placing only single layer of resonators at the top, in the middle, or at the bottom of the active layers for exciting plasmon modes.

The first approach relies on the use of random metallic nanoparticles or periodic metallic structures on top of absorbing material as sketched in Figure 2.8. This approach allows solar cell to trap the light in the absorbing layer due to back reflection of the light from the back of metallic structure, besides exciting the plasmon modes in metal/dielectric surface. The frequencies of allowed plasmon modes can be adjusted by engineering the nano-metallic structures including geometry of the metallic structure, periodicity of the architecture, diameter of the metallic nanoparticle and the type of the metal. At some frequencies especially at high frequencies (low wavelengths), covering the absorbing material with a metallic surface may cause a direct reflection of incoming light. However, the excited surface plasmon modes at other frequencies cause extraordinary oscillations in free electrons in the metal, and they consequently generate highly localized electric fields in the dielectric, which is set to be the absorbing material. This high field concentration contributes to absorptivity of solar cell structure since the absorptivity is linearly dependent on the field intensity (field amplitude square). This approach can also be applied to other

type of light trapping devices such as photodetectors [11,15]. In plasmonic photodetectors, matching the surface plasmon resonance frequency of specially engineered metallic geometry at the operating frequency of the detector leads to increased sensitivity of the photodetector because of allowed plasmon mode at the operating frequency.

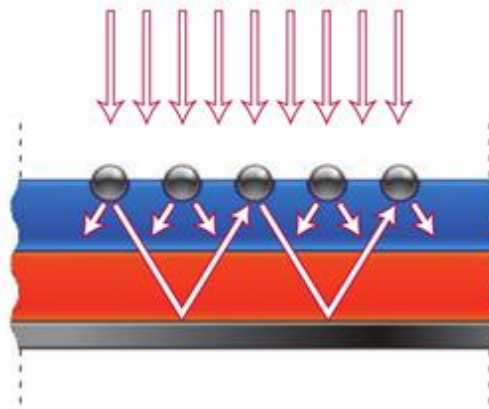


Figure 2.8: Metallic nanoparticles embedded on top of absorbing material to excite the plasmon modes at metal/dielectric interface (plasmonic photovoltaics type 1) [4].

The second plasmonic design approach is to embed random metallic nanoparticles into the active as shown in Figure 2.9. Here the high near-field concentrations localized around the metal allow for the creation of electron-hole pairs in the absorbing material [4]. Also, if the nanoparticles are close enough to each other, it is possible to take the advantage of metal-to-metal interaction, which causes great field increase in the semiconductor [29]. However, the drawback of this approach is that metallic nanoparticles are mixed with absorbing material and it is thus impossible to engineer the design parameters including the distance between the nanoparticles and location of the nanoparticles due to randomness.

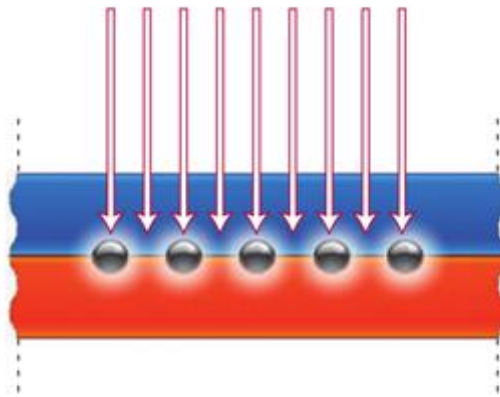


Figure 2.9: Metallic nanoparticles embedded in absorbing material to excite the plasmon modes around the metal nanoparticles (plasmonic photovoltaics type 2) [4].

This second method integrates these metallic nanoparticles into absorbing layer also to employ them as sub-wavelength antennas, which enhance the optical absorption with near-field plasmonic field localization [4].

The last method reported in literature is to metallic periodic structures or metallic nanoparticles on top of the back contact of the solar cell architecture given in Figure 2.10. The surface plasmons excited at the dielectric/metal interface propagates in the plane of absorbing layer and high field concentration enhances the optical absorption in surface plasmon resonance frequencies [4].

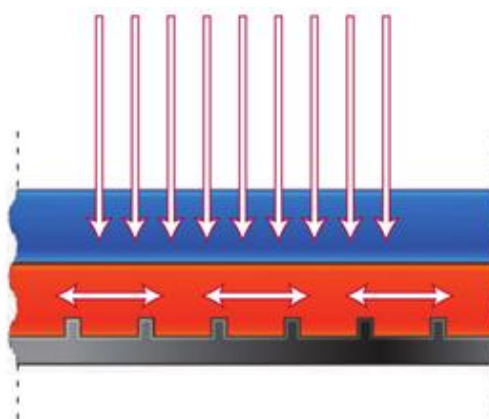


Figure 2.10: Metallic periodic structures integrated with the backcontact (plasmonic photovoltaics type 3) [4].

2.4 Finite-Difference Time-Domain (FDTD) method

The FDTD method is presently the state-of-the-art computation approach for solving Maxwell's curl equations in time domain on discretized spatial grids. This method is first introduced by Kane Yee in 1966. The idea of this method is to solve time dependent Maxwell equations represented in partial differential form by using central-difference approximations to the space and time partial derivatives on a discretized grid. This method has become a popular one for solving electromagnetic problems after progressive advancement in computing technology. Today FDTD method is a widely used technique for understanding the interaction between electromagnetic waves and material structures [55,56]. In this thesis, the numerical simulations that computationally prove our proposed concepts for enhancing the optical absorption in solar cell using new plasmonic architectures are carried out by this method.

FDTD is a time domain solver. However, generally FDTD simulators are used to calculate the electromagnetic fields as a function of frequency (or wavelength). Frequency responses of fields are computed by performing Fourier transforms during the simulation. This allows to obtain complex-valued fields and other derived quantities such as the complex Poynting vector, normalized transmission, and far field projections as a function of frequency (or wavelength).

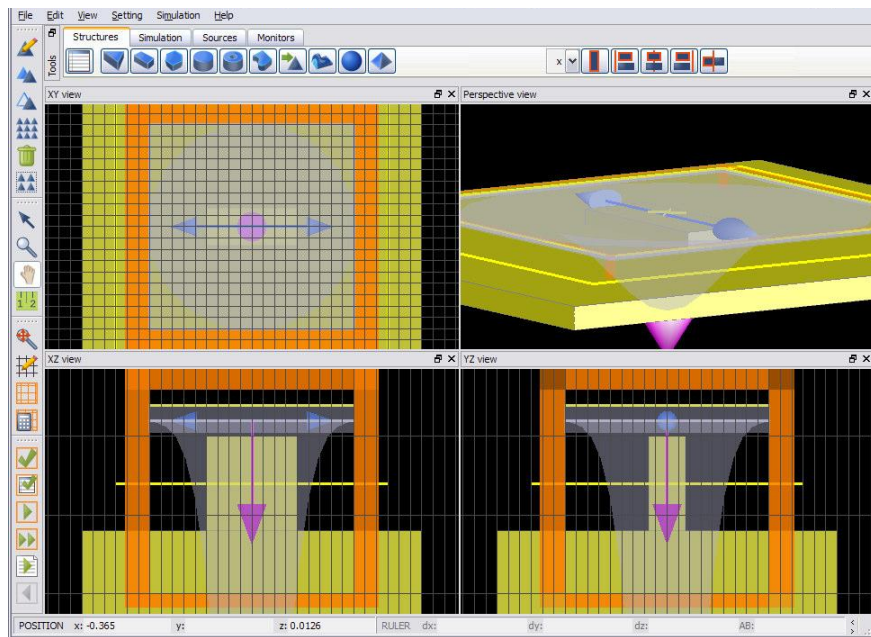


Figure 2.11: A screenshot from Lumerical software user interface.

We performed our simulations with a commercial FDTD software package, which is developed by Lumerical Solutions Inc., Vancouver, Canada (Figure 2.11). The flow chart of creating a simulation in Lumerical FDTD solver is as follows: 1.) generating the structures and assigning material types to these structures, 2.) creating a simulation region, and 3.) selection of the source and placing the data monitors in simulation region.

The software allows us to shape any kind of composite structures via controlling a CAD tool embedded into software. After creating the structures, the material types need to be assigned with corresponding complex refractive indices as a function of frequency. This method allows us to use experimentally measured complex dielectric constant of materials in the definition of the material. Dispersive materials with tabulated refractive index (n,k) data as a function of wavelength can be assigned by the users. The tabulated refractive indexes are also available for well known materials such as Ag, Au, and Al, and different types of references such as Palik, and Johnson and Christy.

After creating the investigated structure and assigning the material properties, the simulation area limits the region where the simulations will be performed should be set. In this section, assigning proper boundary conditions (BC) of the simulation area is important. Lumerical Solutions package supports a range of boundary conditions including: 1.) perfectly matched layer BC (PML) – this condition allows the PML to strongly absorb outgoing waves from the interior of a computational region without reflecting them back into the interior, 2.) periodic BC – this condition is used in the structures that continue along the infinity with some periodicity in the structure architecture and, 3.) Bloch BC – this condition is used when the structures are periodic, and the EM fields are periodic, except for a phase shift between each period.

Sources make another important component of a simulation. FDTD Solutions support a number of different types of sources such as point dipoles, beams, plane waves, total-field scattered-field (TFSF) sources, guided-mode source for integrated optical components and imported sources for interface with external photonic design softwares.

Chapter 3

Principles of Organic Solar Cells

Today renewable and clean energy production is one of the most important components of the global new energy strategy. Photovoltaics receive great attention among other renewable resources because utilizing the power of the Sun is certainly one of the most viable ways to help to combat the foreseeable climate change. Though common materials used in photovoltaics are inorganic materials, there has also been an increasing effort to develop organic solar cells within the last decades. Organic solar cells are particularly attractive because of their ease of processing, non-toxicity, mechanical flexibility and potential for low cost printing of large areas [43,44,46-48]. Thus, in this thesis, we mainly focus on applying and demonstrating plasmonic resonator structures on these promising devices based on different types of organic solar cell architectures.

The advantages make this class of devices attractive, however their low photon conversion efficiency is one of the main problems to be overcome [45]. The latest achieved efficiency levels with their corresponding solar cell structures are gathered and shown in Table 3.1. The results show that the photon conversion efficiencies of these organic solar cell structures under the AM1.5G solar

radiation are noticeably low compared to inorganic solar cell architectures available today. These efficiency values are not high enough to win the competition against mature inorganic photovoltaics technologies; hence, there is a clear need for developing more efficient organic solar cell architectures by optimizing absorbing materials or cell architectures, or embedding functional nanostructures, e.g., to utilize the advantage of surface plasmon excitations in the case of metal nanopatterns. In this thesis, we concentrate on proposing and computing nanometallic resonators to enhance the optical absorption beyond the photon absorption limits in non-metallic organic thin-film solar cell architectures.

Classification ^a	Effic. ^b (%)	Area ^c (cm ²)	V _{oc} (V)	J _{sc} (mA/cm ²)	FF ^d (%)	Test centre ^e (and date)	Description
Silicon							
Si (crystalline)	25.0 ± 0.5	4.00 (da)	0.706	42.7	82.8	Sandia (3/99) ^f	UNSW PERL [17]
Si (multicrystalline)	20.4 ± 0.5	1.002 (ap)	0.664	38.0	80.9	NREL (5/04) ^f	FhG-ISE [18]
Si (thin film transfer)	16.7 ± 0.4	4.017 (ap)	0.645	33.0	78.2	FhG-ISE (7/01) ^f	U. Stuttgart (45 μm thick) [19]
Si (thin film submodule)	10.5 ± 0.3	94.0 (ap)	0.492 ^g	29.7 ^g	72.1	FhG-ISE (8/07) ^f	CSG Solar (1–2 μm on glass; 20 cells) [20]
III–V Cells							
GaAs (thin film)	26.1 ± 0.8	1.001 (ap)	1.045	29.6	84.6	FhG-ISE (7/08) ^f	Radboud U. Nijmegen [21]
GaAs (multicrystalline)	18.4 ± 0.5	4.011 (t)	0.994	23.2	79.7	NREL (11/95) ^f	RTI, Ge substrate [22]
InP (crystalline)	22.1 ± 0.7	4.02 (t)	0.878	29.5	85.4	NREL (4/90) ^f	Spire, epitaxial [23]
Thin Film Chalcogenide							
CIGS (cell)	19.4 ± 0.6 ^h	0.994 (ap)	0.716	33.7	80.3	NREL (1/08) ^f	NREL, CIGS on glass [24]
CIGS (submodule)	16.7 ± 0.4	16.0 (ap)	0.661 ^g	33.6 ^g	75.1	FhG-ISE (3/00) ^f	U. Uppsala, 4 serial cells [25]
CdTe (cell)	16.7 ± 0.5 ^h	1.032 (ap)	0.845	26.1	75.5	NREL (9/01) ^f	NREL, mesa on glass [26]
Amorphous/Nanocrystalline Si							
Si (amorphous)	9.5 ± 0.3 ⁱ	1.070 (ap)	0.859	17.5	63.0	NREL (4/03) ^f	U. Neuchatel [27]
Si (nanocrystalline)	10.1 ± 0.2 ^j	1.199 (ap)	0.539	24.4	76.6	JQA (12/97)	Kaneka (2 μm on glass) [28]
Photochemical							
Dye sensitised	10.4 ± 0.3 ^k	1.004 (ap)	0.729	22.0	65.2	AIST (8/05) ^f	Sharp [29]
Dye sensitised (submodule)	8.5 ± 0.3^k	17.13 (ap)	0.669^g	18.9^g	67.1	AIST (6/09)^f	Sony, 8 serial cells [4]
Organic							
Organic polymer	5.15 ± 0.3 ^k	1.021 (ap)	0.876	9.39	62.5	NREL(12/06) ^f	Konarka [30]
Organic (submodule)	3.5 ± 0.3^k	208.4 (ap)	8.620	0.847	48.3	NREL (7/09)	Solarmer [5]
Multijunction Devices							
GaInP/GaAs/Ge	32.0 ± 1.5 ^l	3.989 (t)	2.622	14.37	85.0	NREL (1/03)	Spectrolab (monolithic)
GaInP/GaAs	30.3 ^l	4.0 (t)	2.488	14.22	85.6	JQA (4/96)	Japan Energy (monolithic) [31]
GaAs/CIS (thin film)	25.8 ± 1.3 ^j	4.00 (t)	—	—	—	NREL (11/89)	Kopin/Boeing (4 terminal) [32]
a-Si/μc-Si (thin submodule) ^{ll}	11.7 ± 0.4 ^{ll}	14.23 (ap)	5.462	2.99	71.3	AIST (9/04)	Kaneka (thin film) [33]
Organic (2-cell tandem)	6.1 ± 0.2^k	1.989	1.589	6.18	61.9	FhG-ISE (7/09)	Heliatek [6]

Table 3.1: Confirmed solar cell architectures and their corresponding measured efficiencies under the AM1.5G solar spectrum at 25⁰C. This table considers the latest and the highest achieved efficiency values considering both organic and inorganic solar cell architectures which is published annually by Green M. et al. This table is taken from “Solar cell efficiency tables (version 35)” published in 2010 [45].

In this chapter, we start our discussion with discussing the general operation principles of organic solar cells by constituting a theoretical background of the organic photonic devices. We will overview the materials that are typically used in organic solar cells. In this chapter, we also give further information on the cell architectures- in particular, copper phthalocyanine/perylene tetracarboxylic-bis-

benzimidazole (CuPc/PTCBI) based solar cell architectures used in Chapter 4 and poly(3-hexylthiophene) doped with phenyl-C61-butyric acid methyl ester (P3HT:PCBM) used in Chapter 5, to both of which we applied plasmonic resonators.

3.1 Organic Solar Cell Architectures and their Operation Principles

The operation principles of organic solar cells are similar to inorganic semiconductor based solar cells. The main differences between the operation of organic and inorganic solar cells are observed in the process of how electron and hole pairs are generated and how a photogenerated charge is transported in organic material [44,47].

The process flow of conversion of illuminated light into electricity via an organic solar cell device can be stated in three consecutive steps: (1)absorption of an incident photon leading to the formation of an excited state, which is, the bound electron - hole pair (exciton) creation, (2)exciton diffusion to a region where exciton dissociation (charge separation) occurs, and (3)charge transport within the organic semiconductor to the respective electrodes.

The operation principles of organic devices also depend on their device architectures which can be classified as: single layer, bilayer heterojunction, bulk heterojunction, and diffuse bilayer heterojunction solar cells. In this classification, the arrangement of donor and acceptor material is considered. In this thesis, we mainly focused on two of these solar cell architectures, bilayer heterojunction and bulk heterojunction architectures.

In bilayer heterojunction architecture, donor and acceptor materials are sequentially stacked together with a planar interface. In the literature, there are various types of material combinations [44] utilized in bilayer heterojunction devices. The CuPc/PTCBI based solar cell used in Chapter 4 is an example of bilayer heterojunction architecture. The cross-sectional view of this cell structure is given in Figure 3.1. In one exemplary device implementation, the active layers can be chosen to be 11 nm thick copper phthalocyanine (CuPc) as a donor layer and 4 nm thick perylene tetracarboxylic bisbenzimidazole (PTCBI) as an acceptor layer.

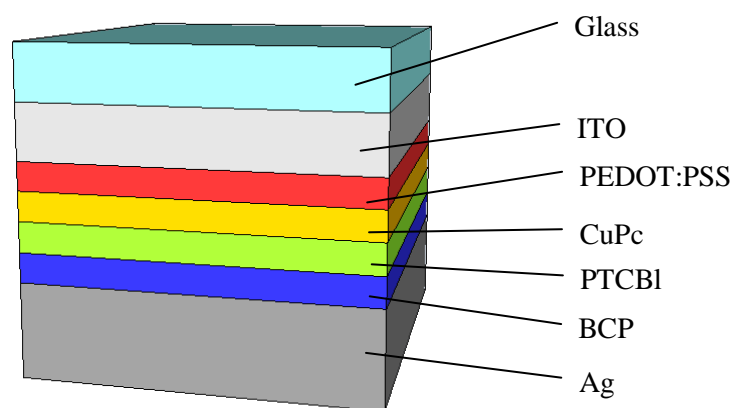


Figure 3.1: Cross-sectional view of bilayer heterojunction thin-film organic solar architecture made of glass/ITO/PEDOT:PSS/CuPc/PTCBI/BCP/Ag layers [52].

The active materials of donor and acceptor layers are sandwiched between two electrodes and the charge separation take place between donor and acceptor layers due to their different ionization potential and electron affinity (Figure 3.2). In such a device architecture, the photon conversion efficiency is limited by the photon absorption and subsequent charge generation, which typically occurs across a 10-20 nm layer thickness. This leads to low photon absorption and consequentially low quantum efficiencies in this type of solar cell structures.

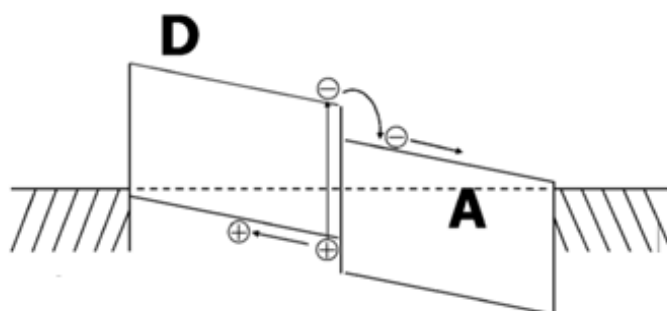


Figure 3.2: Schematic representation of bilayer heterojunction architecture. D stands for donor and A stands for acceptor [44].

The second type of architecture that we considered in this thesis is the bulk heterojunction architecture. In this device architecture, the acceptor and donor materials are blended with each other. Thus, in bulk heterojunction devices, the donor and acceptor phases are intimately intermixed, while in the bilayer heterojunction the acceptor and donor phases are completely separated from each other and selectively make contact to the anode and cathode at their respective sides. Several approaches have been extensively studied for creating bulk heterojunctions by co-deposition of donor and acceptor pigments [57-59], and by solution casting of polymer/polymer [60-62], polymer/molecule [63-66], molecule/molecule [67,68] and donor-acceptor blends in the literature. The P3HT:PCBM active layer based solar cell structure embodied in Chapter 5 is a well-known example of bulk heterojunction architecture. The cross-sectional view of this cell architecture is depicted in Figure 3.3. A schematic of a bulk heterojunction device is sketched in Figure 3.4. The acceptor (A) and the donor (D) materials are blended with each other throughout the whole active layer. Thus, photogenerated excitons are dissociated into separate electron and hole charges at any place across this layer.

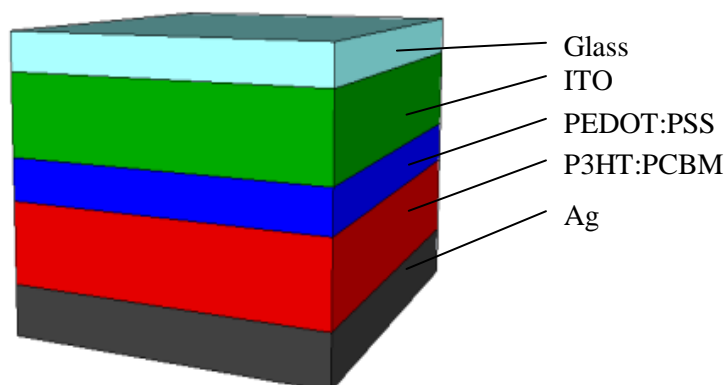


Figure 3.3: Cross-sectional view of bulk heterojunction thin-film organic solar architecture made of glass/ITO/PEDOT:PSS/P3HT:PCBM/Ag layers [71].

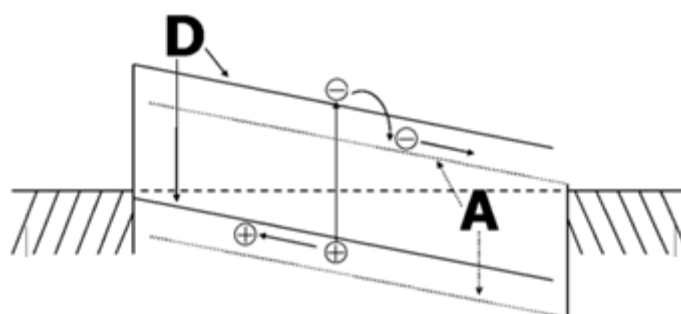


Figure 3.4: Schematic representation of a bulk heterojunction architecture. D stands for donor and A stands for acceptor [44].

The primary photoexcitation events in organic materials do not directly lead to free charge carriers but to coulombically bound electron-hole pairs, the excitons, to be disassociated under the electric field. It is estimated that only 10% of the photoexcitations yield free charge carriers in conjugated polymers at the end. For efficient dissociation of excitons, strong electric fields are necessary. Such local fields can be supplied via externally applied electrical fields (which would defeat the purpose of photovoltaics in the first place) as well as via interfaces (which is possible in D-A blends). At an interface, where abrupt changes of the potential energy occur, strong local electrical fields are possible. Photo-induced charge transfer can occur when an exciton has reached such an interface within

its lifetime. Therefore, exciton diffusion length limits the thicknesses of bilayers. Exciton diffusion length should be in the same order of magnitude as the donor acceptor phase separation length. Otherwise excitons decay via radiative or nonradiative path ways and their energy is lost for the power conversion. Exciton diffusion lengths in conjugated polymers and small organic molecules are usually around 10-20 nm [44,47].

3.2 Materials

In organic solar cells, besides the absorption of incident sunlight, photogeneration of excitons and their separation into charge carriers, the ability to transport these charge carriers is another requirement of selected active absorbing material. This property is commonly found in organic materials that contain a delocalized π -electron, which participates in π -bonding in their chemical structures. It is worth recalling π -bonds are covalent chemical bands format with two lobes of the other involved electron orbitals [44,48].

The materials used in organic solar cells are divided into two classes with respect to their conducting behavior: hole conductivity and electron conductivity. In addition to this distinction, the classification of these materials can be made by their type of processing into solution processable organic semiconducting molecules/polymers and vacuum deposited (evaporated) small molecular materials [43,44,47].

One of the most preferred materials in fabrication of organic solar cells is phthalocyanine and its derivatives. Phthalocyanine is a representative of the p-type, hole-conducting material that works as an electron donor. CuPc (copper phthalocyanine) and ZnPc (zinc phthalocyanine) are two of the well known and widely used phthalocyanine based materials. CuPc is the main active material in organic cell structure utilized in Chapter 4. Phthalocyanine molecules and their

derivatives are often used in evaporated solar cells. The three important representatives of hole-conducting donor type polymers are MDMO-PPV (poly[2-methoxy-5-(3,7-dimethyloctyloxy)]-1,4-phenylenevinylene), P3HT (poly(3-hexylthiophene-2,5-diyl)) and PFB (poly(9,9'-dioctylfluorene-co-bis-N,N'-(4-butylphenyl)-bis-N,N'-phenyl-1,4-phenylenediamine)). P3HT is the main active material used in combination with PCBM in organic cell device indicated in Chapter 5. The chemical structures of MDMO-PPV, ZnPC, P3HT, PFB and MDMO-PPV are shown in Figure 3.5.

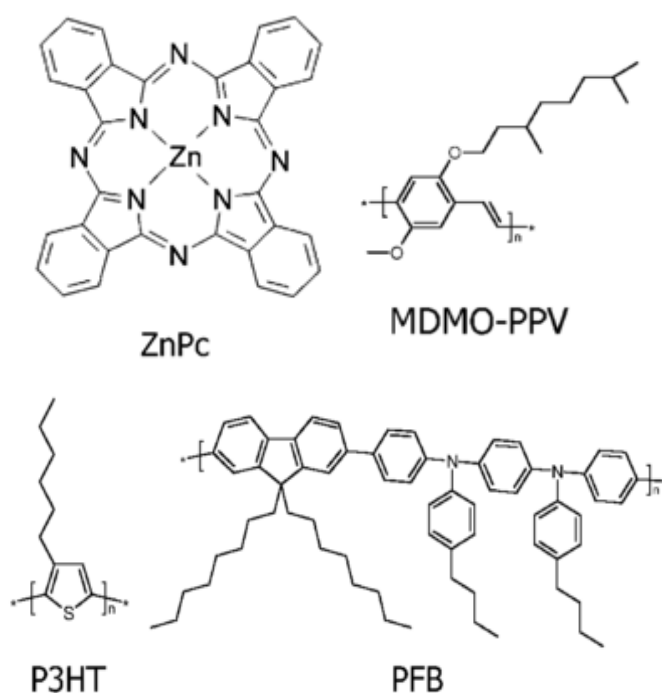


Figure 3.5: Chemical structures of examples of hole-conducting materials that work as electron donor: ZnPC, MDMO-PPV, P3HT, and PFB [44].

The other widely used organic materials in organic solar cell fabrication are perylene and its derivatives. The perylene and its derivatives show an n-type, electron-conducting behavior and serve as electron acceptor materials. In Figure 3.6, some commonly used electron-conducting organic materials are given. These include C₆₀ (buckminster fullerene), Me-Ptcdi (N,N'-dimethyl- perylene-

3,4,9,10-dicarboximide), CN-MEH-PPV (poly-[2-methoxy-5-(2'-ethylhexyloxy)-1,4-(1-cyanovinylene)-phenylene] and F8BT (poly(9,9'-dioctylfluorene-co-benzothiadiazole) and PCBM (1-(3-methoxycarbonyl) propyl-1-phenyl[6,6]C₆₀), a soluble derivative of C₆₀. As phthalocyanine, the perylene based molecules, Me-Ptcdi and C₆₀ are incorporated into evaporated solar cells. CN-MEH-PPV, PCBM and F8BT organic materials are solution processible because of their side-chain solubilization, and these polymers also show photoluminescence and electroluminescence.

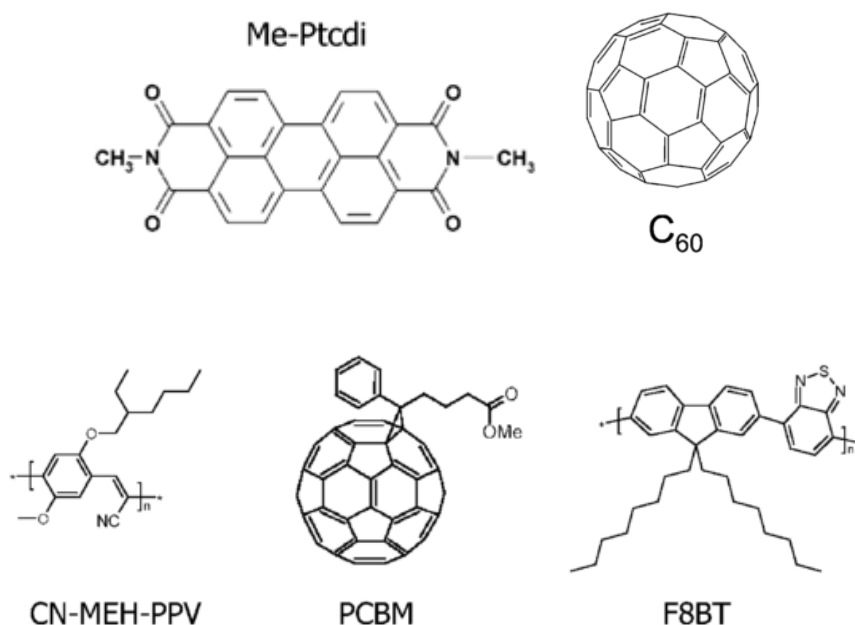


Figure 3.6: Chemical structures of example of electron-conducting materials that works as electron acceptor materials: Me-Ptcdi, C₆₀, CN-MEH-PPV, PCBM, and F8TB [47].

To display the fraction of sunlight that can contribute to energy conversion in these materials, absorption coefficients of thin films of some organic active materials are shown in comparison with the air mass (AM)1.5 standard solar spectrum in Figure 3.7. Different from the most commonly used active materials in inorganic solar cell, e.g., Si, the organic materials use only the blue side of the solar spectrum, whereas the typical absorption spectrum of silicon extends over the red side of solar spectrum (up to 1100 nm).

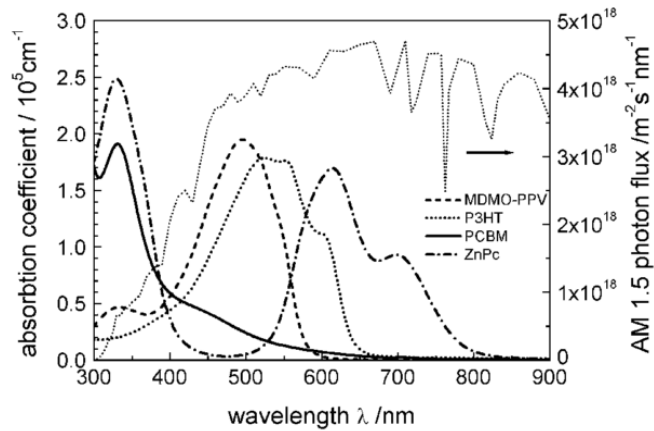


Figure 3.7: Absorption coefficients of organic semiconductors commonly used active materials in organic solar cell layers depicted in comparison with the standard AM1.5G solar spectrum [47].

One of the most commonly used bulk heterojunction organic solar cell structure can be realized in five subsequent thin-film layers of Al or Ag cathode, active layer, PEDOT:PSS and ITO anode glass substrate in sandwich geometry shown in Figure 3.8. Up to this point we introduced and discussed only the organic absorbing materials used as the active layer in organic solar cells. Other important non-absorbing materials used in the fabrication of organic solar cells are indium-tin-oxide (ITO) and poly(3,4-ethylenedioxythiophene) poly(styrenesulfonate) (PEDOT:PSS).

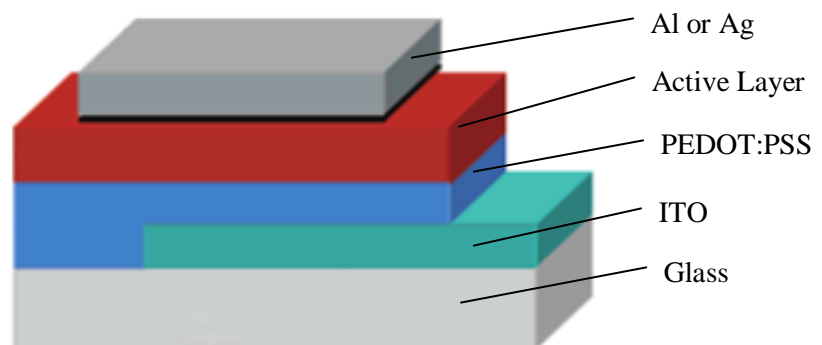


Figure 3.8: Schematic device structure for a general organic solar cell. The active layer is sandwiched between two contacts: an indium-tin-oxide electrode coated with a hole transport layer PEDOT:PSS and an top electrode.

In Figure 3.8, from bottom to top, the first part is the solar cell substrate, which can be made of a heat-resistant transparent substrate such as glass, or a flexible substrate such as polyester. While conventional inorganic solar cells allow light to enter through a conductive grid anode on the opposite end, organic devices generally admit light through a transparent substrate that is coated with a transparent contact layer. For example, ITO is a commercially available transparent conductive coating used as the cathode. This is the second layer of organic solar cell (and the first thin film on glass). ITO is highly preferred because of its optical transparency and carrier injection properties that can be further enhanced using film treatments. On the transparent conducting coated substrate, PEDOT:PSS is spin-coated as the second thin film from an aqueous solution. The chemical structures of PEDOT and PSS are shown in Figure 3.9. This PEDOT:PSS layer improves the surface quality of the ITO electrode by covering the rough surface, making it smoother, and reducing the probability of short-circuiting and facilitates the hole extraction. Furthermore, the workfunction of this electrode can be conveniently changed by chemical/electrochemical redox reactions of the PEDOT layer. Subsequently, the active layers are coated using solution or vacuum deposition techniques. Finally, the top electrode is evaporated to serve as an anode. In general, a lower workfunction metal as compared to ITO such as aluminum (Al) or silver (Ag) are used to extract electrons from this side of the organic solar cell.

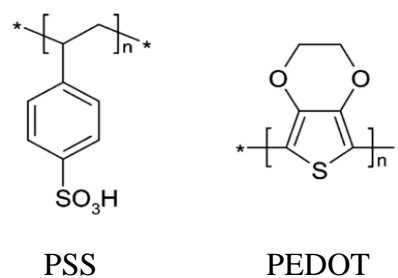


Figure 3.9: Chemical structure of hole transport layer PEDOT-PSS (poly(3,4-ethylenedioxythiophene)-polystyrene-*para*-sulfonic acid) [47].

Chapter 4

Increased absorption for all polarizations via excitation of plasmonic modes in metallic grating backcontact

Recently increasing optical absorption in inorganic and organic solar cell architectures via excitation of surface plasmon modes using nano-metallic structures has received great interest [4,5]. The main reason of incorporating such engineered metallic structures into the solar cells is to increase the solar conversion efficiency of these photovoltaic devices to compete with the fossil fuel based energy production [4]. Organic solar cells are good candidates for future photovoltaics technology since they can be produced at low costs. However, the limited solar conversion efficiency near the band edge due to weak optical absorption is still an important problem to be addressed [44,45].

Surface plasmons are electromagnetic oscillations of free electrons located in the metallic structure, which favorably leads to strong field localization at the metallic/dielectric interface provided that the surface plasmon momentum matching conditions satisfied are satisfied [6]. The polarization of incoming light and the design parameters of the metallic structure (height of the structure, periodicity of the structure, type of the material, etc.) are among the important factors that control these electron oscillations and foremost the field localization [6].

In the literature, there is a significant amount of research work reported on the plasmonic enhancement of the optical absorption in organic/inorganic solar cells when a specific polarization condition of the illuminated light is satisfied [4,5,11-40]. In these previous works, one polarization may cause great field localization in the active material because of the excitation of plasmon modes. On the other hand, the other polarization may not lead to as much strong field localization. Even one may observe reduced absorption in the other polarization. However, in the most realist case, we observe that the incoming and scattered sun light is omni-polarized, including both transverse electromagnetic (TE) and transverse magnetic (TM) polarizations. Hence, designing a proper plasmonic geometry that simultaneously enhances the optical absorption under both TE- and TM-polarized illumination is essential to future plasmonic solar cells.

In this chapter, we introduce periodic plasmonic resonators integrated on top of organic solar cell backcontact for achieving significant absorption enhancements in both polarizations. We present our device architecture along with the plasmonic design and describe our FDTD simulations that we performed in this chapter. We finally present and discuss our numerical simulation.

4.1 Device Structure

We demonstrate our plasmonic architectures in a organic solar cell based on a popular, well-known material of P3HT:PCBM. As we introduced in Chapter 3, this organic solar cell architecture is a type of bulk heterojunction devices that use a mixtures of donor and acceptor active materials. In such bulk heterojunction devices the photogenerated excitons (bound electron-hole pairs) form across the absorbing material in its entirety and subsequently disassociated in this layer since the donor and acceptor materials are blended with each other.

The device architecture details are given as follows. A thick Ag cathode layer is covered by a 100 nm thick absorbing layer of P3HT:PCBM (typically one-to-one ratio mixture of poly-3-hexylthiophene and phenyl-C61-butyric acid methyl ester). A 50 nm thick PEDOT:PSS (poly(3,4-ethylenedioxythiophene):poly(styrenesulfonate)) layer is used for the hole transportation in the device. Subsequently, a transparent 150 nm thick ITO (indium-tin-oxide) layer is followed on top of the PEDOT:PSS layer for providing an electrical contact from the organic solar cell architecture. A transparent glass substrate (refractive index $n \sim 1.52$) is used to provide mechanical support for these thin-film layers spun on it. The schematic view of this solar cell architecture is illustrated in Figure 4.1.

In our group, we have been working on the fabrication of P3HT:PCBM organic solar cells. These PEDOT:PSS and ITO layers are optimized to make optimal layer thicknesses in our fabrication. To simulate the most realistic case, these optimized layer thicknesses are used in the simulations. The thickness of the active material is, on the other hand, chosen as a design parameter. Our simulations showed that a 100 nm thick active material is the best to observe the strongest effect of plasmonic resonators. Also the experimentally produced solar cell architectures feature a P3HT:PCBM active layer thickness in the order of ~ 100 s of nanometers.

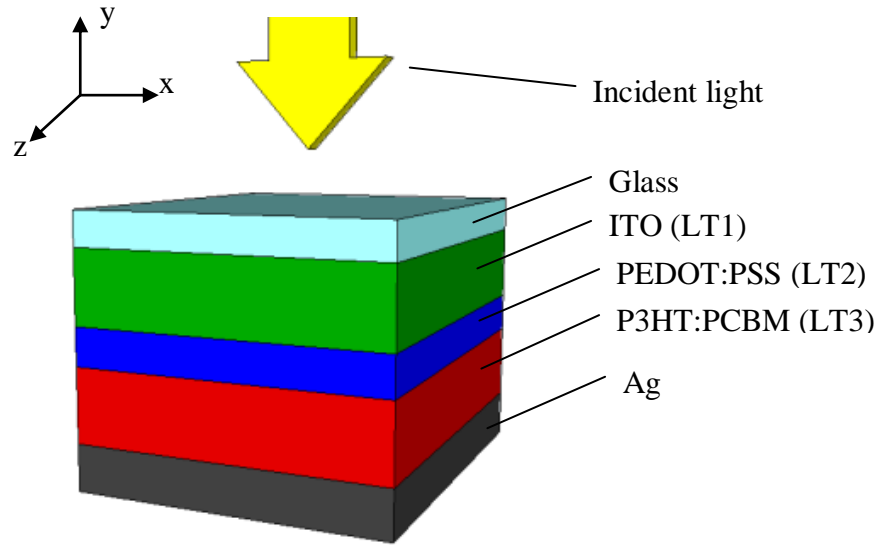


Figure 4.1: Cross-sectional view of the bare (non-metallic) thin-film organic solar cell architecture made of glass/ITO/PEDOT:PSS/P3HT:PCBM/Ag. (Here LT stands for the corresponding layer thickness.)

In our comparative study, we analyzed two plasmonic architectures embedded into the solar cell architecture comprised of glass/ITO/PEDOT:PSS/P3HT:PCBM/Ag layers and compared their absorptivity performance with the case of bare device architecture to identify the enhancement of the proposed plasmonic resonators. The first investigated plasmonic architecture is the bottom silver grating architecture. This structure consists of periodic silver gratings placed on top of the silver cathode layer. Our aim in designing this structure is to excite surface plasmons around the silver grating and consequently to enhance the optical absorption in the active materials. The cross-sectional view of the corresponding plasmonic architecture is presented in Figure 4.2. In this architecture, some of the active material is replaced by the metallic grating. Here we do not add any active material to compensate for the removed active material; the active material thickness is fixed to 100 nm in all cases. The second plasmonic architecture that we consider for comparison purposes in this chapter is the top silver grating embedded in the organic solar cell device, as shown in Figure 4.3. In this architecture, the hole transport layer (PEDOT:PSS layer) is partially substituted by the periodic silver

grating. The top periodic grating structure has been widely studied in the previous literature [4,5,23-28,31,32]. Here we simulate and compare our proposed plasmonic architecture of patterned backcontact with this well-studied top grating architecture to understand the performance enhancement contribution of our plasmonic architecture located on the bottom silver grating in the cathode layer.

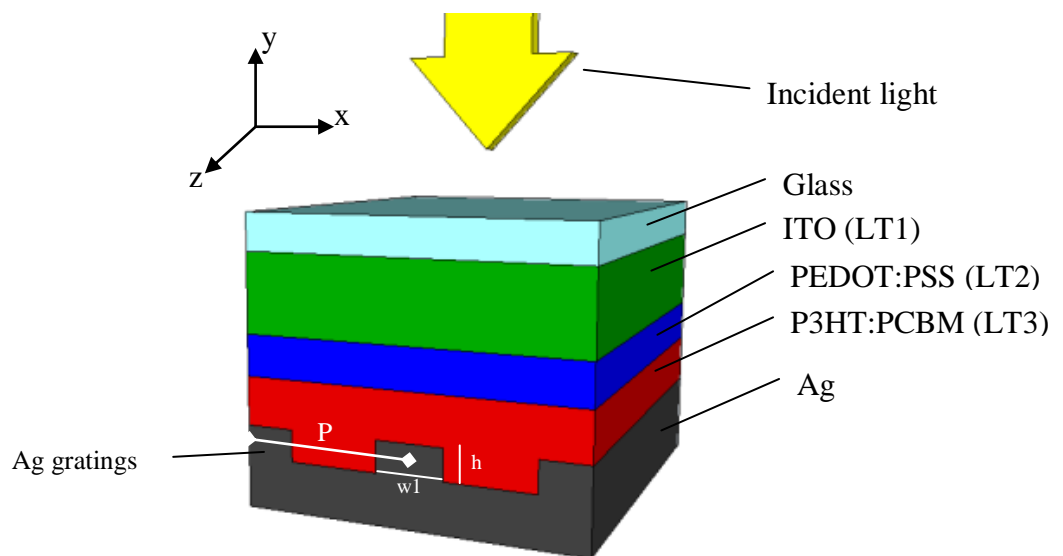


Figure 4.2: Cross-sectional view of the thin-film organic solar architecture made of glass/ITO/PEDOT:PSS/P3HT:PCBM/Ag with the bottom silver grating. (Here LT stands for layer thickness of the corresponding layer, P indicates the period, w1 denotes the width, and h represents the height of the bottom silver grating.) In our simulations, the illumination is set to be normal to the device structure and the architecture is assumed to be infinite along the x and z axes.

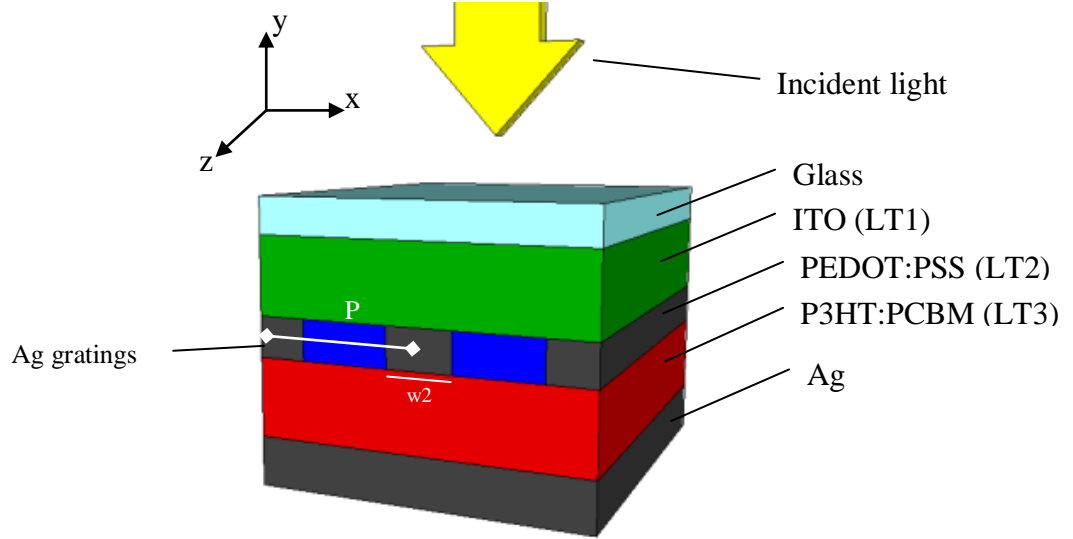


Figure 4.3: Cross-sectional view of the thin-film organic solar cell structure made of glass/ITO/PEDOT:PSS/P3HT:PCBM/Ag with the top silver grating. (Here LT stands for layer thickness of the corresponding layer, P indicates the period, and w_2 indicates the width of the top silver grating.) In our simulations, the illumination is set to be normal to the device structure and the architecture is assumed to be infinite along the x and z axes.

4.2 Numerical Simulations

We performed 2-dimensional finite-difference time-domain (FDTD) simulations to compute the optical absorption in different devices structures and understand the absorption enhancement contribution of plasmonic architectures embedded into the solar cell. In our computations we use experimentally measured complex dielectric constants of Ag [69], P3HT:PCBM [54], PEDOT:PSS [73] and ITO [74] layers with no approximation. All of the investigated organic solar cells structures are illuminated by a planewave incident through the glass, which is set normal to the cell structure, as illustrated in Figure 4.1, Figure 4.2 and Figure 4.3. Periodic boundary conditions are set along the x-axis (x_{\max} and x_{\min}) and perfectly matched layer (PML) boundaries are set along the y-axis (y_{\max} and

y_{\min}). The absorption spectra are calculated in the active P3HT:PCBM layer in the wavelength range of 400 nm and 900 nm. This wavelength range covers most of the effective solar radiation spectrum and the absorption region of P3HT:PCBM active material.

As described in the previous section, we particularly examine three different cases: namely, the bare (non-metallic) organic solar cell architecture given in Figure 4.1, the bottom backcontact grating architecture depicted in Figure 4.2 and the top silver grating architecture illustrated in Figure 4.3. We simulated all of these architectures separately under normally-incident planewave illumination in both of TM polarization – with the magnetic field pointed along the z-axis while the electric field is directed along x-axis – and TE polarization – with the electric field pointed along the z-axis while the magnetic field is directed along x-axis – separately.

4.3 Numerical Analyses

Figure 4.4 presents the absorption spectra of the active material in the bare, bottom grating and top grating architectures under the TM-polarized light. In these simulations, we choose the architecture parameters as follows: the periodicity of the metallic gratings $P=130$ nm, ITO layer thickness $LT_1=150$ nm, PEDOT:PSS layer thickness $LT_2=50$ nm, P3HT:PCBM layer thickness $LT_3=100$ nm, width of the bottom grating $w_1=50$ nm, width of the top grating $w_2=50$ nm, and height of the bottom grating $h=50$ nm.

The effective photon conversion in P3HT:PCBM active material based devices take place in the 400-650 nm range because of high optical absorption of the active material in this range. The plasmonic bottom grating structure enhances the optical absorption of P3HT:PCBM based organic solar cell in 400-450 nm and 525-800 nm ranges because of the excitation of surface plasmon modes in the metallic grating. Especially the absorption increases in the 650-800nm range

where the bare architecture suffers from the optical absorption of incoming photons. There is a crossover of the absorption curves of the bare and bottom grating architecture in the 450-525 nm range. On the other hand, the optical absorption is reduced when we embed a plasmonic top grating structure especially in the 400-575nm range.

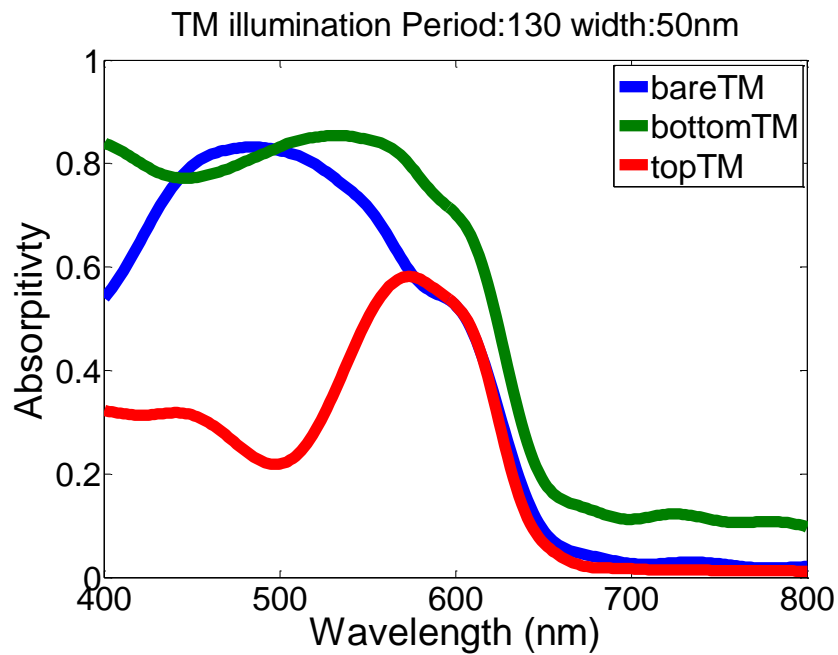


Figure 4.4: Absorption spectra of the organic active material in the bare, bottom grating, and top grating structures under TM-polarized light illumination, computed for the device parameters of $P=130$ nm, $LT1=150$ nm, $LT2=50$ nm, $LT3=100$ nm, $w1=50$ nm, $w2=50$ nm, and $h=50$ nm.

The normalized electric field profiles for the corresponding cell structures under TM-polarized illumination at different wavelength are presented in Figure 4.5-4.10. The field profiles of the bare, bottom grating and top grating architectures at $\lambda=500$ nm are given in Figure 4.5, Figure 4.7 and Figure 4.9 and the field profile of these device architectures at $\lambda=600$ nm are depicted in Figure 4.6, Figure 4.8 and Figure 4.10, respectively. For easy visualization, one unit cell of the repeating plasmonic architecture is displayed; all layers in the architecture

are highlighted with solid white lines. These devices are illuminated under TM-polarized light. The dimensions of the bottom and top grating are set equal with a 50 nm height and a 50 nm width. The resulting field profiles are normalized in the range of 0-10.

Figure 4.5 and Figure 4.6 show the field profiles generated in the bare (non metallic) architecture. The field intensity in the volume of the active material is slightly higher compared to other layers. Also some reflection from the PEDOT:PSS layer can be observed in these maps. Figure 4.7 and Figure 4.8 clearly prove the surface plasmons generated around the bottom metallic gratings (represented as high field intensities in the color map) which are localized in the active material. These surface plasmon polaritons directly contributes to absorptivity enhancement of the active material. These improvements are indicated in the absorption spectra of Figure 4.4. Figure 4.9 and Figure 4.10 present the electric field map of the top grating architecture under TM-polarized at $\lambda=600$ nm and $\lambda=550$ nm, respectively. As we notice in Figure 4.4, the absorptivity performance of the top grating based architecture is lower than the absorptivity of the bare architecture. The field profiles show that the top metallic gratings reflect the incoming light, and this reflection causes a decrease in the absorption of the active material. The field intensity in the volume of the active material in the top grating architecture at $\lambda=550$ nm (given in Figure 4.9) is lower compared to that of the bare architecture. However at 600 nm, the electric field in the volume of the active material shows an equal amplitude level (thus, equal electric field intensity), implying that the optical absorption of the bare and top metallic architectures are similar.

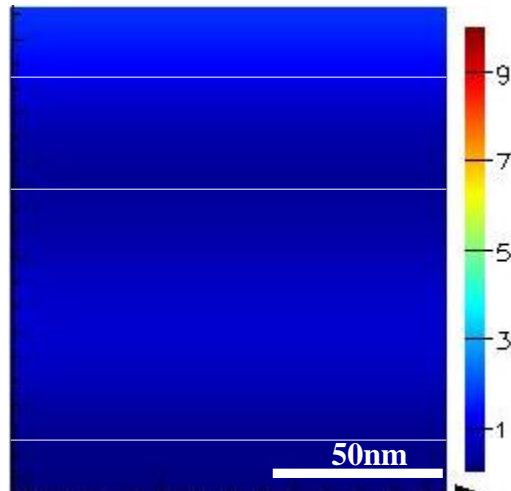


Figure 4.5: Normalized electric field map for the bare organic solar architecture (given in Figure 4.1) under TM-polarized light at $\lambda=550$ nm, computed for the device parameters of $P=130$ nm, $LT1=150$ nm, $LT2=50$ nm, and $LT3=100$ nm. Only one unit cell of the repeating grating structure is shown in this electric field profile.

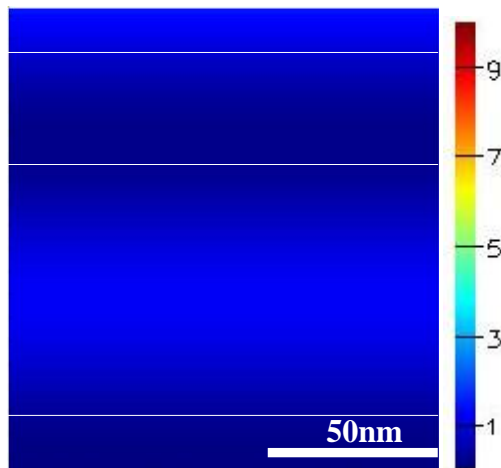


Figure 4.6: Normalized electric field map for the bare organic solar architecture (given in Figure 4.1) under TM-polarized light at $\lambda=600$ nm, computed for the device parameters of $P=130$ nm, $LT1=150$ nm, $LT2=50$ nm, and $LT3=100$ nm. Only one unit cell of the repeating grating structure is shown in this electric field profile.

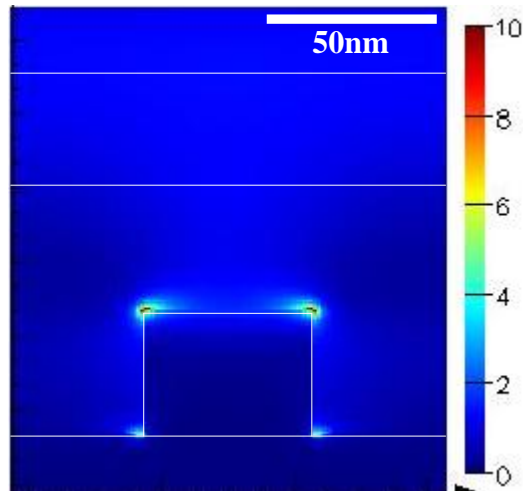


Figure 4.7: Normalized electric field map for the bottom grating organic solar architecture (given in Figure 4.2) under TM-polarized light at $\lambda=550$ nm, computed for the device parameters of $P=130$ nm, $LT1=150$ nm, $LT2=50$ nm, $LT3=100$ nm, $w1=50$ nm, and $h=50$ nm. Only one unit cell of the repeating grating structure is shown in this electric field profile.

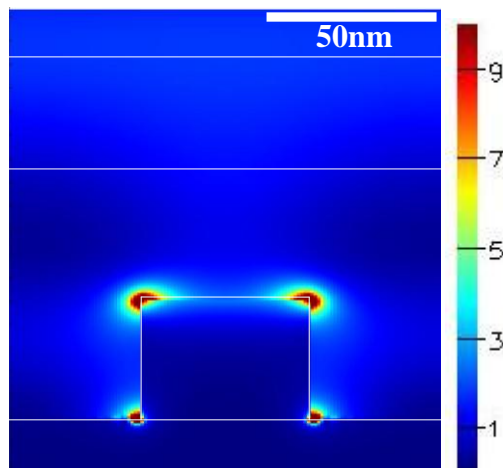


Figure 4.8: Normalized electric field map for the bottom grating organic solar architecture (given in Figure 4.2) under TM-polarized light at $\lambda=600$ nm, computed for the device parameters of $P=130$ nm, $LT1=150$ nm, $LT2=50$ nm, $LT3=100$ nm, $w1=50$ nm, and $h=50$ nm. Only one unit cell of the repeating grating structure is shown in this electric field profile.

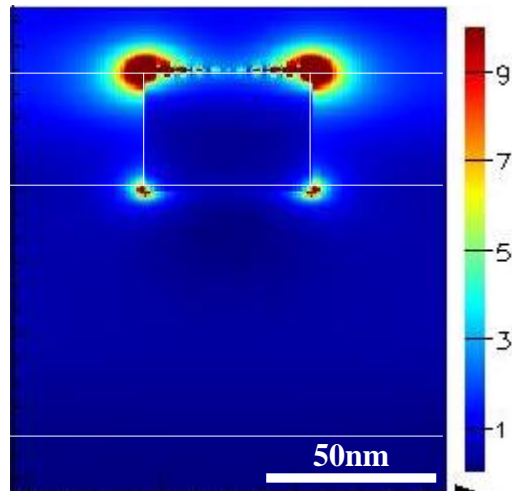


Figure 4.9: Normalized electric field map for the top grating organic solar architecture (given in Figure 4.3) under TM-polarized light at $\lambda=550$ nm, computed for the device parameters of $P=130$ nm, $LT1=150$ nm, $LT2=50$ nm, $LT3=100$ nm, and $w2=50$ nm. Only one unit cell of the repeating grating structure is shown in this electric field profile.

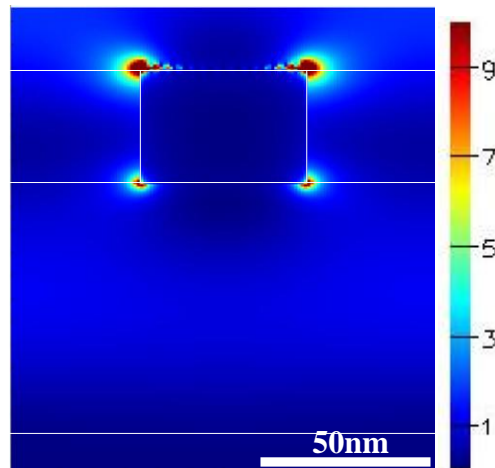


Figure 4.10: Normalized electric field map for the top grating organic solar architecture (given in Figure 4.3) under TM-polarized light at $\lambda=600$ nm, computed for the device parameters of $P=130$ nm, $LT1=150$ nm, $LT2=50$ nm, $LT3=100$ nm, and $w2=50$ nm. Only one unit cell of the repeating grating structure is shown in this electric field profile.

Figure 4.11 presents the electric field intensity (electric field square) enhancement in the volume of active layer in the bottom and top grating

architectures in comparison to the electric field in the bare structure. To compute the field intensity enhancement in the structure, we use equation given by (5.1):

$$\frac{\int_V |E_{top,bottom}|^2 dV}{\int_V |E_{bare}|^2 dV} \quad (5.1)$$

The optical absorption spectrum at a given wavelength is given by $A = \omega * Im(\epsilon) \oint_V |E|^2 dV'$ relation, where E is the electric field; V is volume of the material, and $Im(\epsilon)$ is the dielectric constant of the material of which absorption will be calculated. Figure 4.11 shows that we enhance the electric field in the 400-800 nm region, except for a small region of 450-500 nm. In the 550-800nm range, the electric field is boosted up to 6 folds by placing the bottom plasmonic structure. However, the top grating architecture reduces the electric field in the active material. This condition causes to decrease the overall absorption as observed in Figure 4.4.

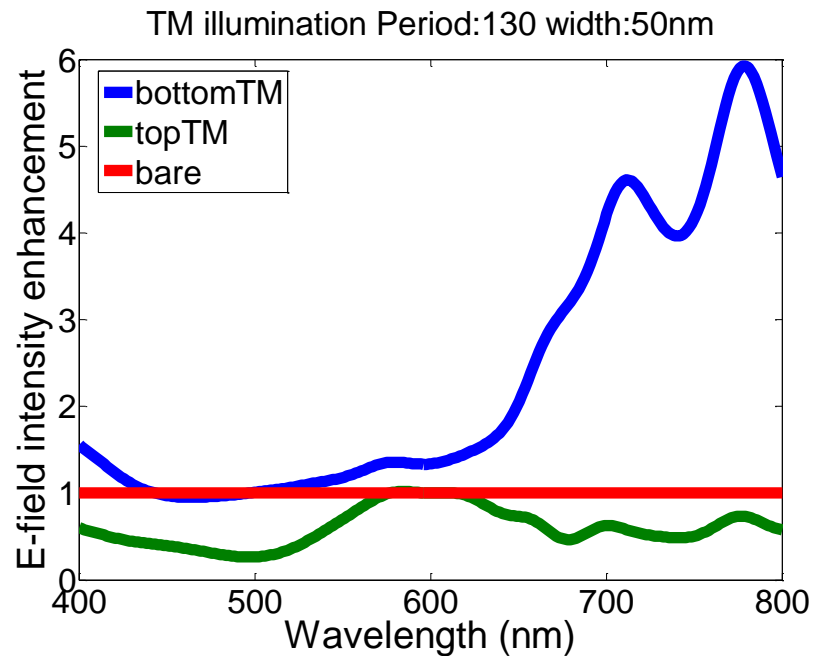


Figure 4.11: Electric field intensity enhancement within the volume of the organic active material using the bottom grating (given in Figure 4.2) and the top grating (given in Figure 4.3) structures compare to that generated in the bare structure. This field enhancement is

computed for TM-polarized light illumination. Using the device parameter of $P=130$ nm, $LT1=150$ nm, $LT2=50$ nm, $LT3=100$ nm, $w1=50$ nm, $w2=50$ nm, and $h=50$ nm.

We also investigated the optical absorptivity behavior of these architectures under TE-polarized light illumination. Figure 4.11 presents the absorption spectra of the bare, the bottom grating and the top grating architectures. In these simulations, we chose the structure parameters as follows: the periodicity of the metallic gratings $P=130$ nm, ITO layer thickness $LT1=150$ nm, PEDOT:PSS layer thickness $LT2=50$ nm, P3HT:PCBM layer thickness $LT3=100$ nm, width of the bottom grating $w1=50$ nm, width of the top grating $w2=50$ nm, and height of the grating $h=50$ nm.

As can be observed in Figure 4.11, the bottom plasmonic architecture exhibits a broadband absorption enhancement under TE polarization because of strong field localization in the P3HT:PCBM layer according to the excitation of waveguide modes. On the other hand, the top plasmonic architecture suppresses the optical absorption since the incoming light is reflected from the metallic grating placed on top of the active material, except for the 630-700nm range.

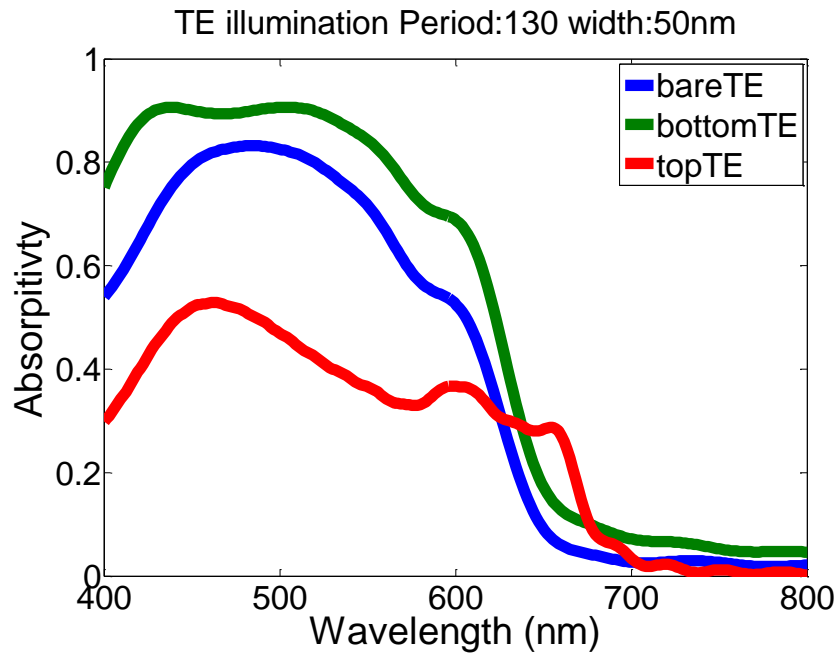


Figure 4.12: Absorption spectra of the organic active material in the bare, bottom grating, and top grating structures under TE-polarized light illumination, computed for the device parameter of; $P=130$ nm, $LT1=150$ nm, $LT2=50$ nm, $LT3=100$ nm, $w1=50$ nm, $w2=50$ nm, and $h=50$ nm.

The normalized electric field profiles for the corresponding cell structures under TE polarized illumination at $\lambda=600$ nm are shown in Figure 4.13-4.15. The field maps of the bare, bottom grating and top grating architectures are presented in these figures in their respective order. For the visualization, one unit cell of the repeating plasmonic architecture is displayed, all layers are highlighted with solid white lines. These field profiles are normalized in the range of 0-1.5.

Figure 4.13 depicts the field profile generated in the bare (non metallic) architecture. The field intensity in the volume of the active material is slightly higher than the other layers. Also a reflection from the PEDOT:PSS layer is observed in this field profile. Figure 4.14 presents the electric field profile for the bottom grating architecture. The excited modes around the metallic surface (bottom grating) lead to strong field localization due to oscillations around this metallic surface. The refractive index difference between the P3HT:PCBM

($n \sim 2.1$ at $\lambda = 600$ nm) and PEDOT:PSS ($n \sim 1.45$ at $\lambda = 600$ nm) layers causes total internal reflection, thus the light is trapped in the P3HT:PCBM active layer. Figure 4.15 presents the electric field intensity behavior of the top grating architecture under TM-polarized illumination at $\lambda = 600$ nm. As observed in Figure 4.12, the absorptivity performance is lower than that of the bare architecture. The field map shows that the top metallic gratings reflect the incoming light, which decreases the optical absorption of the active material.

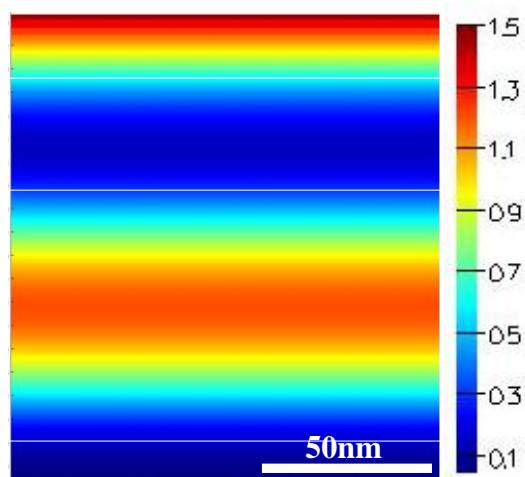


Figure 4.13: Normalized electric field map for the bare organic solar architecture (given in Figure 4.1) under TE-polarized light at $\lambda = 600$ nm, computed for the device parameters of $P = 130$ nm, $LT1 = 150$ nm, $LT2 = 50$ nm, and $LT3 = 100$ nm. Only one unit cell of the repeating grating structure is shown in this electric field profile.

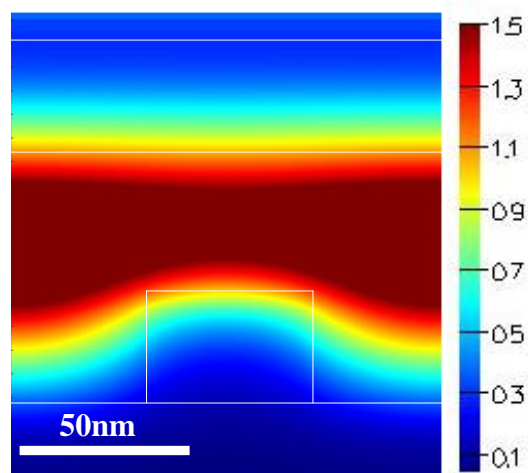


Figure 4.14: Normalized electric field map for the bottom grating organic solar architecture (given in Figure 4.2) under TE-polarized light at $\lambda=600$ nm, computed for the device parameters of $P=130$ nm, $LT1=150$ nm, $LT2=50$ nm, $LT3=100$ nm, $w1=50$ nm, and $h=50$ nm. Only one unit cell of the repeating grating structure is shown in this electric field profile.

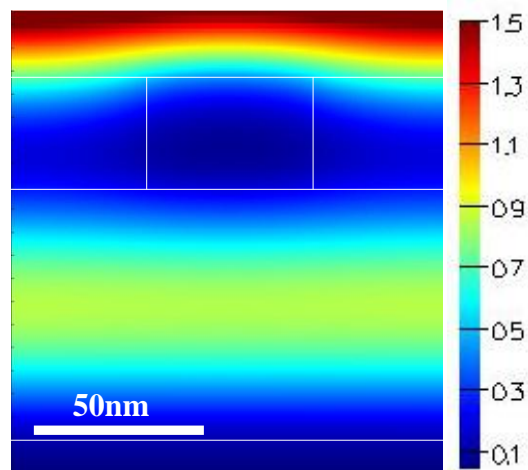


Figure 4.15: Normalized electric field map for the top grating organic solar architecture (given in Figure 4.3) under TE-polarized light at $\lambda=600$ nm, computed for the device parameters of $P=130$ nm, $LT1=150$ nm, $LT2=50$ nm, $LT3=100$ nm, and $w2=50$ nm. Only one unit cell of the repeating grating structure is shown in this electric field profile.

Figure 4.16 presents the electric field intensity enhancement in the volume of active layer in the computed using (5.1) bottom and top grating architectures compare to the electric field intensity in the bare structure. Figure 4.16 shows that we enhance the electric field in the 400-800 nm region. In the 550-800nm range, the electric field is enhanced up to 2.7 folds with the bottom grating structure. The top grating architecture reduces the electric field intensity in active material except for the enhancement in 630-700 nm range. In this range, the allowed waveguide modes at these frequencies lead to the localized surface plasmons located at the bottom of top grating. The normalized field map of the top grating structure is given in Figure 4.17. This field localization at these frequencies enhances the absorptivity in this wavelength range as shown in Figure 4.12.

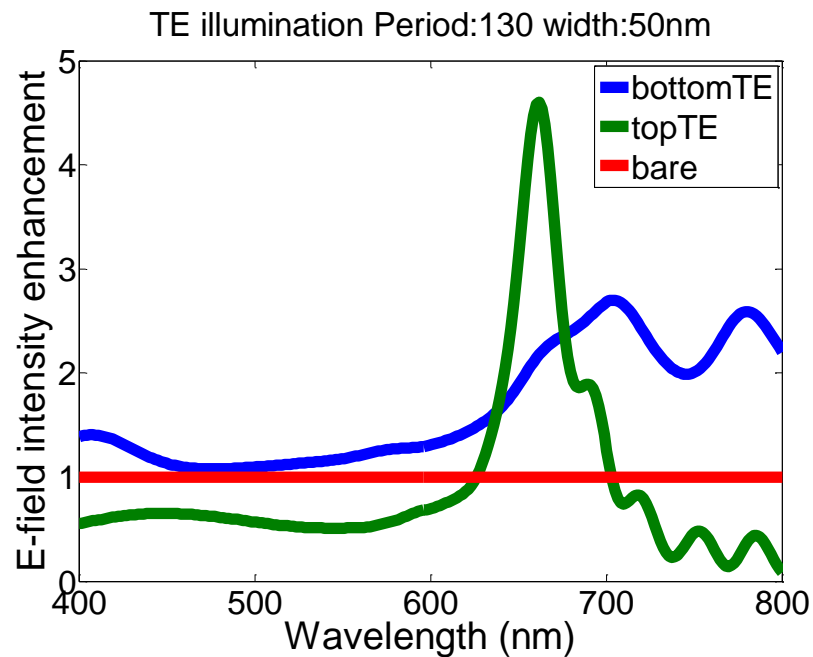


Figure 4.16: Electric field intensity enhancement within the volume of the organic active material using the bottom grating (given in Figure 4.2) and the top grating (given in Figure 4.3) structures compare to that generated in the bare structure. This field enhancement is computed for TE-polarized light illumination. Using the device parameter of $P=130$ nm, $LT1=150$ nm, $LT2=50$ nm, $LT3=100$ nm, $w1=50$ nm, $w2=50$ nm, and $h=50$ nm.

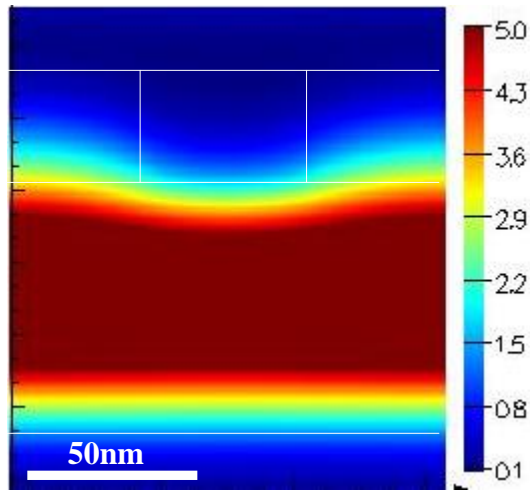


Figure 4.17: Normalized electric field map for the top grating organic solar architecture (given in Figure 4.3) under TE-polarized light at $\lambda=650$ nm, computed for the device parameters of $P=130$ nm, $LT1=150$ nm, $LT2=50$ nm, $LT3=100$ nm, and $w2=50$ nm. Only one unit cell of the repeating grating structure is shown in this electric field profile.

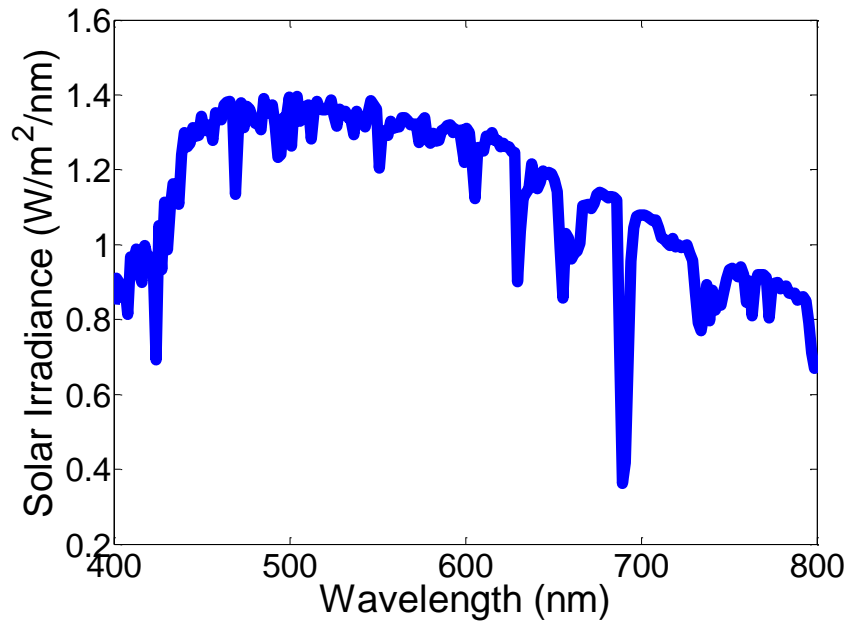


Figure 4.18: Air mass (AM) 1.5G solar radiation [4].

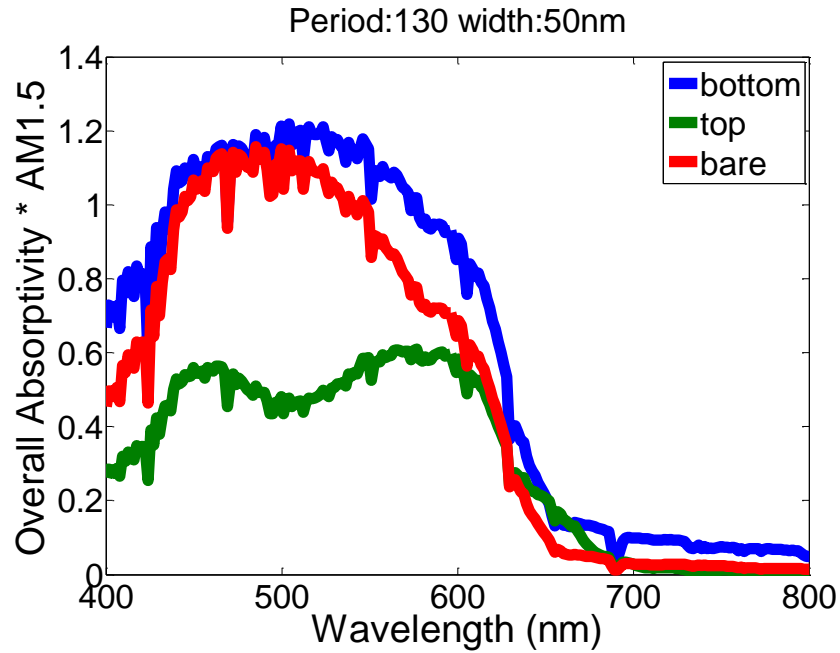


Figure 4.19: Multiplication of AM1.5G solar radiation and overall absorptivity in the volume of the organic active material in the bare, bottom grating, and top grating structures compared to the electric field generated in the bare structure, computed for the device parameters of $P=130$ nm, $LT1=150$ nm, $LT2=50$ nm, $LT3=100$ nm, $w1=50$ nm, $w2=50$ nm, and $h=50$ nm.

In the FDTD simulations, the illuminated light has an equal weight at every wavelength; however, the spectrum of the sun has different light contributions at different wavelengths. AM1.5G solar radiation, which is commonly used in photovoltaic device characterization, mimic the radiation of the sun as shown in Figure 4.18. It is important to calculate the enhancement factors under AM1.5G to identify the contribution of plasmonic architecture. Figure 4.19 presents the multiplication of the overall absorption, which is given by the average of absorptivity under both TE- and TM-polarized $(A_{TM}+A_{TE})/2$, with this AM1.5G solar spectrum. We simply compute the performance enhancement of the plasmonic solar cell architecture (in %) under AM1.5G solar radiation by using (4.2):

$$\frac{\int_0^\infty \left(\frac{A_{TM}(\lambda) + A_{TE}(\lambda)}{2} \right) * AM1.5G(\lambda) d\lambda - \int_0^\infty A_{bare} * AM1.5G(\lambda) d\lambda}{\int_0^\infty A_{bare} * AM1.5G(\lambda) d\lambda} * 100 \quad (4.2)$$

As a result, we show that we enhance the absorption by up to ~21% using backcontact grating with respect to the bare structure. This performance level is reached by using the proposed architecture parameters (Figure 4.20): periodicity of the metallic grating $P=130$ nm, ITO layer thickness $LT1=150$ nm, PEDOT:PSS layer thickness $LT2=50$ nm, P3HT:PCBM layer thickness $LT3=100$ nm, width of bottom grating $w1=50$ nm, width of top grating $w2=50$ nm, and height of the grating $h=50$ nm.

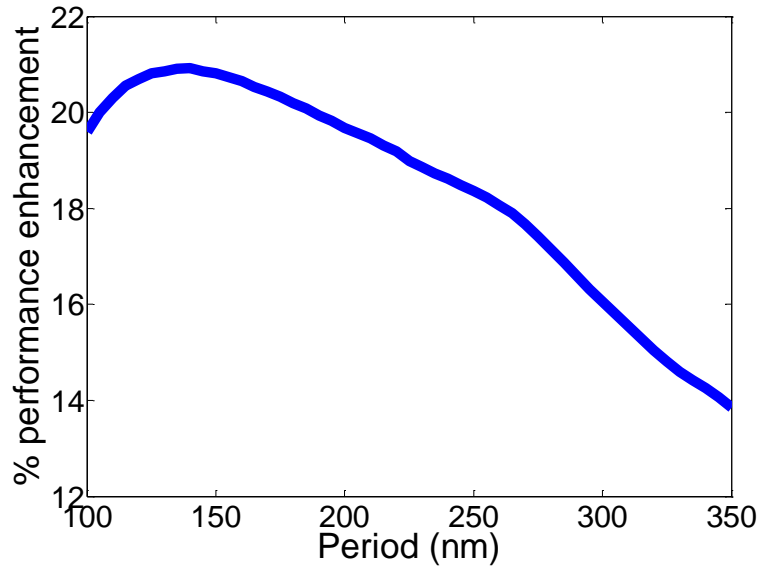


Figure 4.20: Absorption enhancement of backside grating in comparison to the bare device computed for the following parameters: ITO layer thickness $LT1=150$ nm, PEDOT:PSS layer thickness $LT2=50$ nm, P3HT:PCBM layer thickness $LT3=100$ nm, width of bottom grating $w1=50$ nm, and height of the grating $h=50$ nm.

We also consider the effect of silver grating periodicity on the absorptivity for only top, only bottom, and volumetric resonator architectures under both TE- and TM-polarized illumination. The absorptivity vs. periodicity maps of the bare structure, bottom grating structure under TE-polarized illumination, bottom grating structure under TM-polarized illumination, top grating structure under

TE polarized illumination and top grating structure under TM-polarized illumination are given in Figure 4.21, Figure 4.22, Figure 4.23, Figure 4.24 and Figure 4.25 respectively. All absorptivity vs. periodicity maps are normalized in the absorptivity range of 0-1.

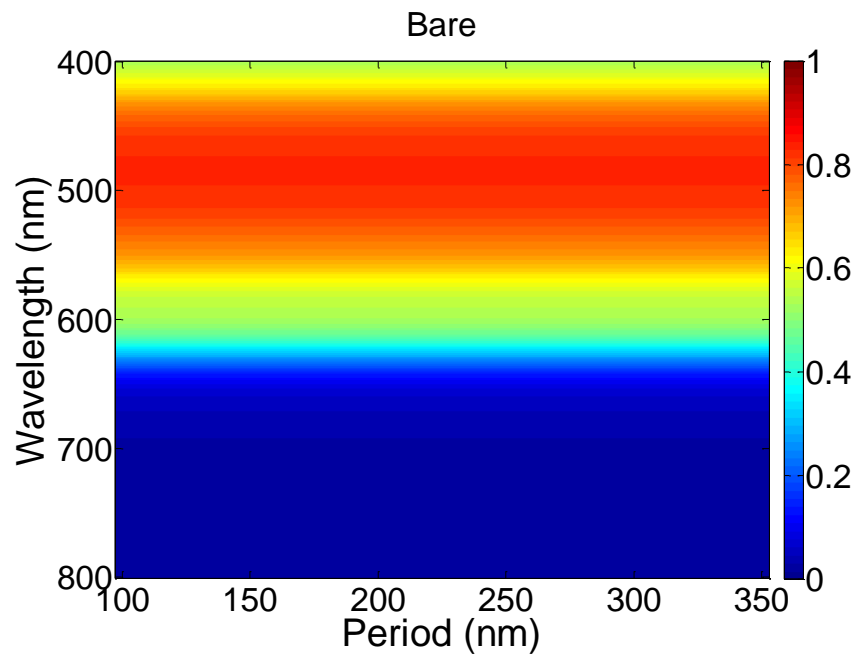


Figure 4.21: Normalized absorptivity map of the bare solar cell for comparison. These absorption spectra are computed for the device parameters of $LT1=150$ nm, $LT2=50$ nm, and $LT3=100$ nm.

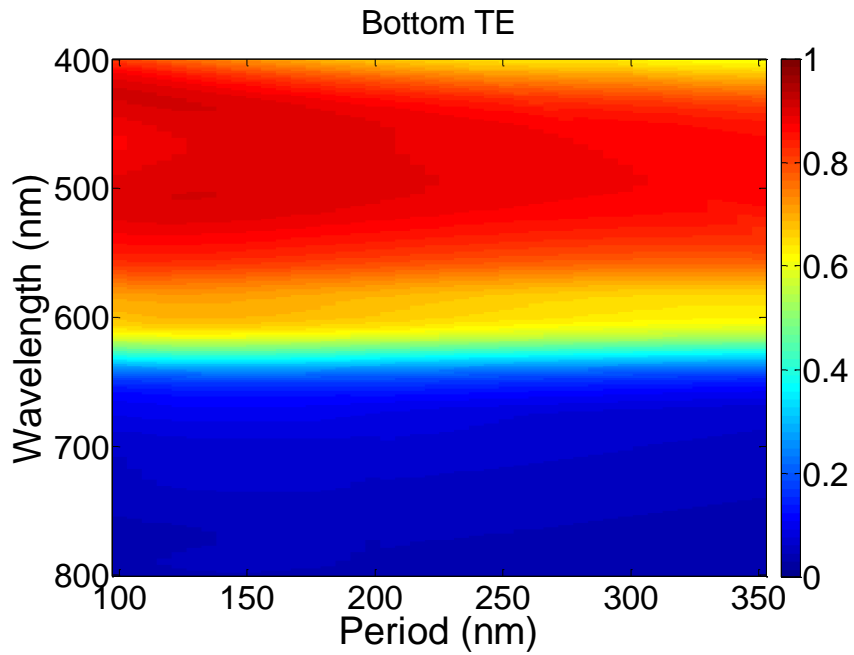


Figure 4.22: Normalized absorptivity map of the bottom metallic grating solar cell as a function of the periodicity of the silver grating under TE-polarized light. Here the absorption spectra are computed for the device parameters of $LT_1=150$ nm, $LT_2=50$ nm, $LT_3=100$ nm, $w_1=50$ nm, and $h=50$ nm.

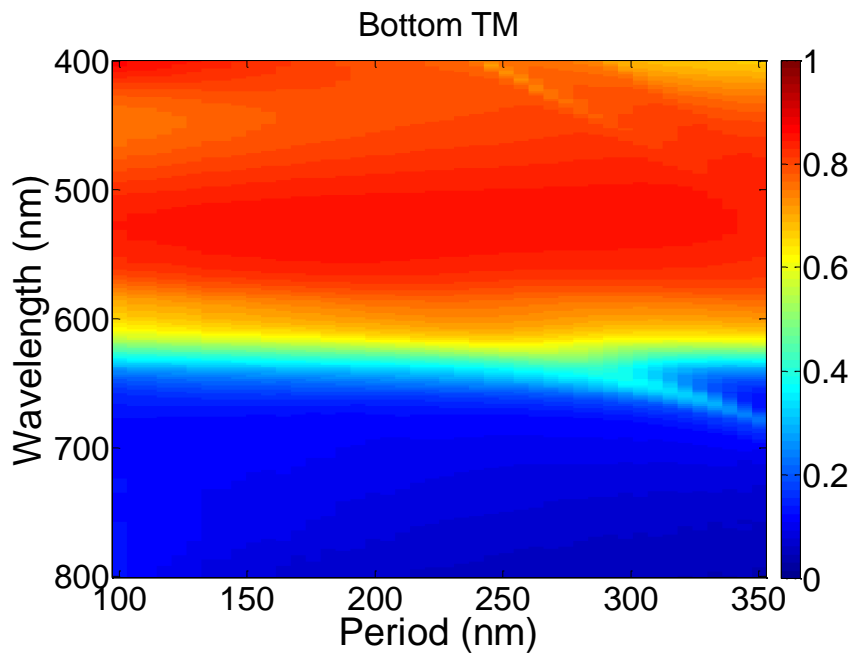


Figure 4.23: Normalized absorptivity map of the bottom metallic grating solar cell as a function of the periodicity of the silver grating under TM-polarized light. Here the

absorption spectra are computed for the device parameters of $LT1=150$ nm, $LT2=50$ nm, $LT3=100$ nm, $w1=50$ nm, and $h=50$ nm.

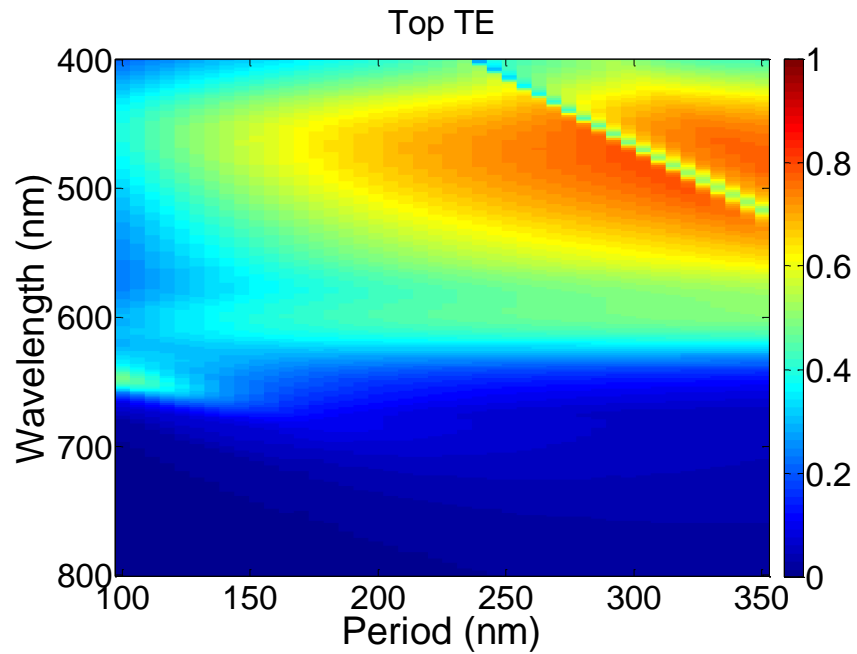


Figure 4.24: Normalized absorptivity map of the top metallic grating solar cell as a function of the periodicity of the silver grating under TE-polarized light. Here the absorption spectra are computed for the device parameters of $LT1=150$ nm, $LT2=50$ nm, $LT3=100$ nm, and $w2=50$ nm.

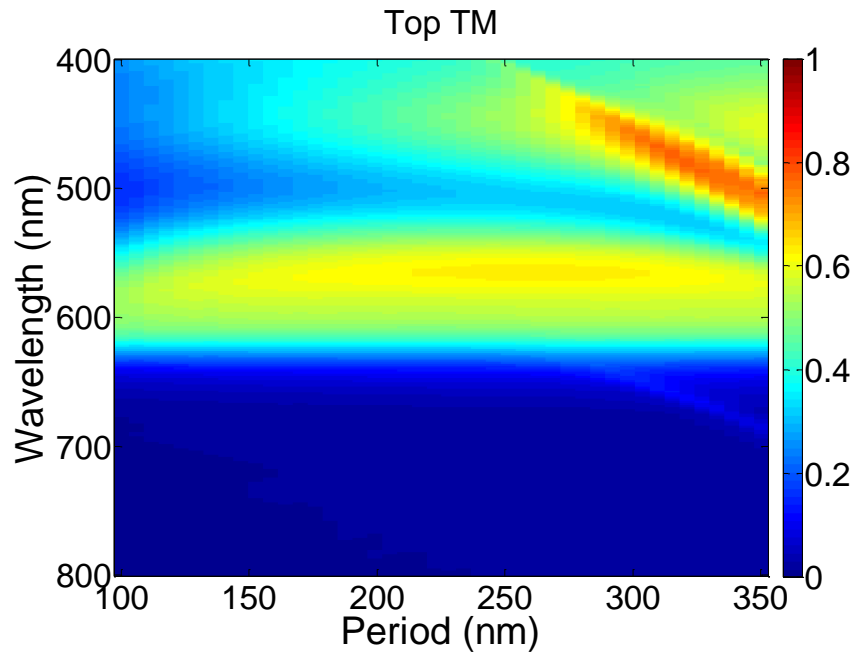


Figure 4.25: Normalized absorptivity map of the top metallic grating solar cell as a function of the periodicity of the silver grating under TM-polarized light. Here the absorption spectra are computed for the device parameters of $LT1=150$ nm, $LT2=50$ nm, $LT3=100$ nm, and $w2=50$ nm.

The absorptivity behavior of the bottom grating embedded architecture remains almost the same in 100-350nm period range. For long periodicities, the absorptivity tend to decrease and match the absorptivity of the bare structure since large field enhancement via excited surface plasmon modes per volume decreases and the plasmonic excitation behavior becomes insignificant. The top grating architecture has the lowest absorptivity behavior at every periodicity. For long periodicities, the absorption of active material in the top grating architecture also increases since the top metallic grating stops reflecting and allows for more light to couple into active material.

In conclusion, we apply periodic metallic grating structure for enhanced optical absorption in P3HT:PCBM based solar cell. We simulate the performance of architectures under both TE and TM polarized illumination and also present the parametric study results for this structure. By taking the advantage of generated

surface plasmon polaritons near metal/dielectric interface, we are able to observe a plasmon assisted absorption increase in the active layers of this solar cell. Plasmon enhanced absorption proposed in this paper is a promising way to increase the performance of solar cells. This design strategy can be extended to 3-dimensional metallic structures and different kind of solar cell architectures.

Chapter 5

Volumetric plasmonic resonators for increased absorption in thin-film organic solar cells

New generation organic thin-film solar cells are designed to feature very thin layers of active material (absorbing material) in the order of tens of nanometers, which conveniently offers the advantage of cost reduction to compete with today's fossil fuel based energy production. In such thin-film organic solar cells, however, the photon conversion efficiency is limited by the photon absorption and photogeneration, which typically occur their very thin layers in the range of 10 – 20 nm film thicknesses [43,44]. Thus, this type of device architecture - based on very thin active layers - undesirably suffers ruinously limited total optical absorption of incident photons in these active layers. To address this problem, there has been an increasing interest in designing plasmonic structures around the active layers to enhance their low optical absorption. Using a single layer of such plasmonic structures either on the top or at the bottom of these

absorbing layers has been extensively studied in the literature and impressive enhancements in optical absorption have been achieved in these studies [4,5,10-28,31,32,34-36,38-42].

In this thesis work, different than our previous work and the other groups', we focus on a new design concept of volumetric plasmonic resonator that relies on the idea of coupling two layers of plasmonic structures embedded in the organic solar cells. For this, here we incorporate one metal grating on the top of the absorbing layer and another at the bottom of the active layer in order to couple them with each other such that field localization is further increased within the volume of the active material between gratings. In addition to individual plasmonic resonances of these metallic structures, this approach allows us to take the advantage of the vertical interaction in the volumetric resonator. This interaction contributes to further enhancement of optical absorption in the active layer, beyond the limited photon absorption in non-metallic (bare) organic solar cell. We used finite-difference time-domain electromagnetic simulations for demonstrating these proposed structures and understanding the contribution of plasmonic resonators on increased absorptivity. Our results show that this architecture exhibits a substantial absorption enhancement performance particularly under the transverse magnetic (TM) polarized illumination, while the optical absorption is maintained at a similar level as the top grating under the transverse electric (TE) polarized illumination. As a result, the overall optical absorption in the active layer (which is the average of the optical absorption under TE- and TM-polarized illumination, $(A_{TE}+A_{TM})/2$) is enhanced up to ~67% compared to non-metallic architecture.

In this section, we present the solar cell structures in which we incorporate the plasmonic resonators. We also provide a detailed description of the FDTD simulations that we performed. Here we present the results of these simulations along with their optimization results and corresponding field distributions and

our discussion on the effects of placing single layer of plasmonic resonators and double layers of volumetric resonators.

5.1 Device Structure

We report a new design consisting of two metallic gratings placed around the active organic materials, which enables enhanced optical absorption in the active layers of bilayer heterojunction organic solar cell structure. We applied our plasmonic design in this organic solar cell architecture which was previously proposed by Peumans et al. [52]. A schematic of this bilayer heterojunction organic solar architecture based on copper phthalocyanine (CuPc) and perylene tetracarboxylic bisbenzimidazole (PTCBI) active layers is presented in Figure 5.1. This architecture consists of six thin-film layers; including the cathode layer, the electron transport layer, the electron acceptor layer, the electron donor (hole acceptor) layer, the hole transport layer, and the anode layer on glass as the substrate.

In Figure 5.1, the bottom Ag cathode layer is covered by a transparent bathocuproine (BCP) layer that facilitates electron transportation. Following BCP, the thin active layers are a 4 nm thick PTCBI electron acceptor layer and a 11 nm thick CuPc electron donor (hole acceptor) layer deposited on BCP layer. The adjacent hole transparent poly (3,4-ethylenedioxythiophene) poly(styrenesulfonate) (PEDOT:PSS) layer collects holes from the underneath CuPc layer in the structure. The top transparent ITO (indium thin oxide) layer serves as the anode and provides electrical contact from the solar cell. For providing a mechanical support, protecting the sensitive organic materials, and sustaining the device operation, the layered device is constructed on glass substrate. This architecture does not include any plasmonic structure, which we refer to as the bare organic solar cell, or the negative control group.

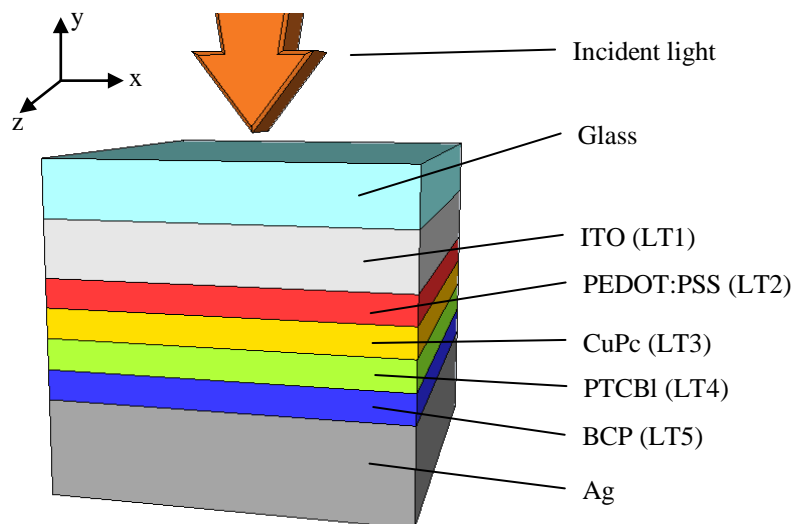


Figure 5.1: Cross-sectional view of bare thin-film organic solar architecture (negative control group) made of glass/ITO/PEDOT:PSS/CuPc/PTCBI/BCP/Ag. (Here LT stands for layer thickness. Also note that this device cross-section is shown upside down here, with the incident light from the top.)

In our comparative study, we also analyzed three plasmonic architectures embedded into the same solar cell structure ITO/PEDOT:PSS/CuPc/PTCBI/BCP/Ag, as sketched in Figure 5.1 and compare the absorptivity performance with the bare architecture to identify the contribution of our proposed plasmonic resonators. The device with a top silver grating is shown in Figure 5.2. In this architecture, the hole transport layer is partially substituted by a periodic silver grating. The architecture with a bottom silver grating is depicted in Figure 5.3. This structure is based on placing periodic plasmonic structure by partially substituting the electron transporting layer. In the case of volumetric plasmonic resonators, both the top and bottom silver gratings are included, as presented in Figure 5.4. The top and bottom gratings are matched with each other to take the advantage of vertical interaction between the top and bottom plasmonic structures.

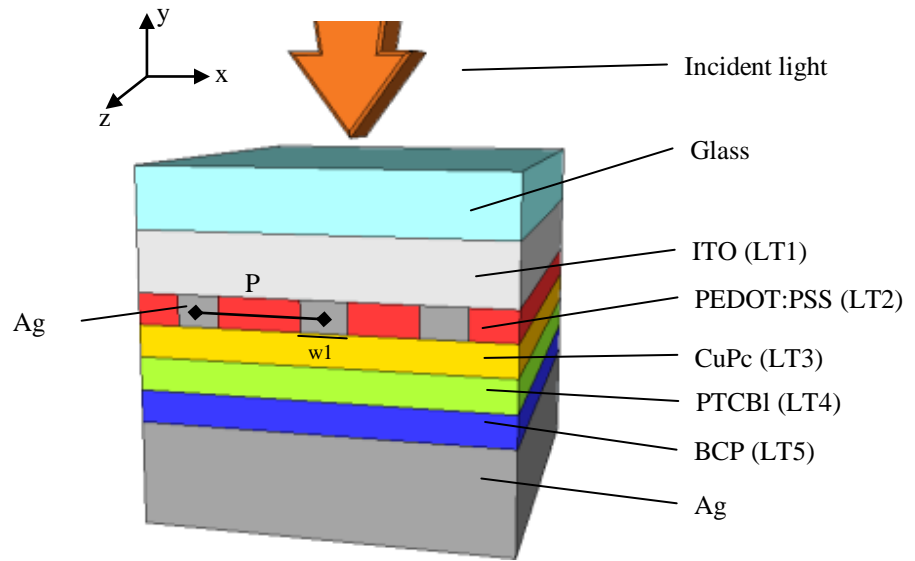


Figure 5.2: Cross-sectional view of thin-film organic solar structure made of glass/ITO/PEDOT:PSS/CuPc/PTCBI/BCP/Ag with the top silver grating. (Here LT stands for layer thickness, P indicates the period, and w_1 denotes the width of the top silver grating.) In our simulations, the illumination is set to be normal to the device structure and the architecture is assumed to be infinite along the x and z axes.

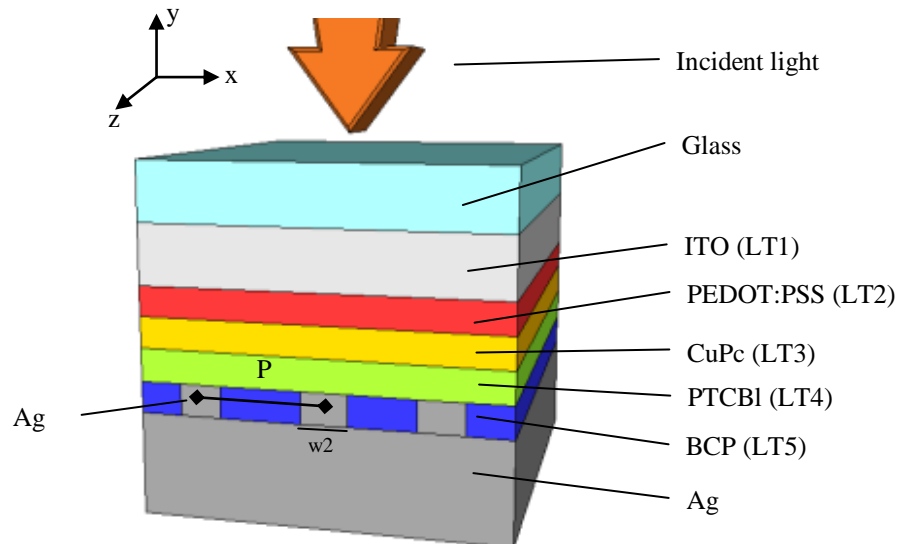


Figure 5.3: Cross-sectional view of thin-film organic solar structure made of glass/ITO/PEDOT:PSS/CuPc/PTCBI/BCP/Ag with the bottom silver grating. (Here LT stands for layer thickness, P indicates the period, and w_2 denotes the width of the bottom

silver grating.) In our simulations, the illumination is set to be normal to the device structure and the architecture is assumed to be infinite along the x and z axes.

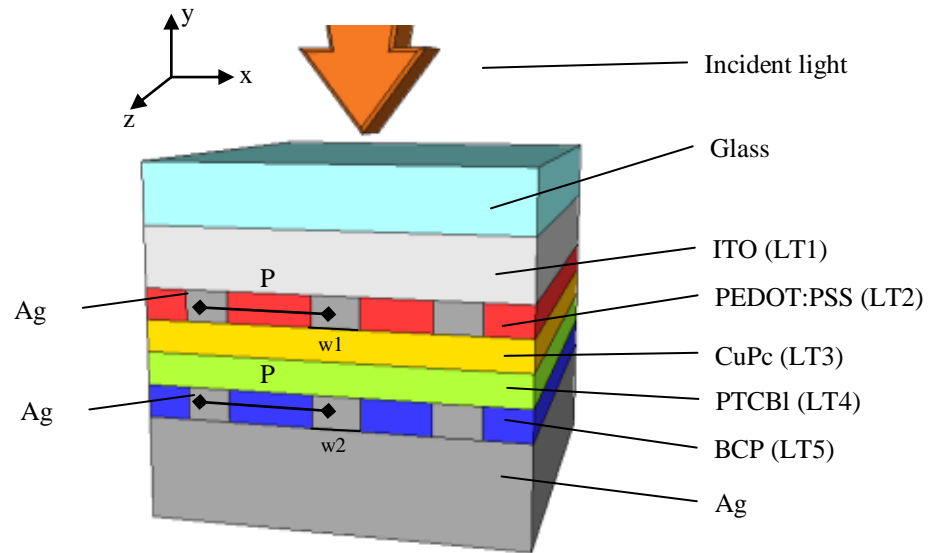


Figure 5.4: Cross-sectional view of thin-film organic solar architecture made of glass/ITO/PEDOT:PSS/CuPc/PTCBI/BCP/Ag with the volumetric silver gratings (including both the top and bottom metal gratings.)(Here LT stands for layer thickness, P indicates the period of the gratings, and w1 and w2 denote the width of the top and bottom silver grating, respectively.) In our simulations, the illumination is set to be normal to the device structure and the architecture is assumed to be infinite along the x and z axes.

5.2 Numerical Simulations

We investigated the effect of metallic gratings on the absorptivity of the active layers by 2-dimensional finite-difference time-domain (FDTD) simulations using a commercially available software package developed by Lumerical Solutions Inc., Canada. In these simulations, we compute the frequency domain responses by taking the Fourier transform of time domain representations. This simulation tool allows us to use experimental refractive index data to represent the thin-film materials including PEDOT:PSS [73], ITO [74], CuPc [26], PTCBI [26], BCP [53] and Ag [69] used in our device structures. The modeled

structures are illuminated by a planewave normal to the device surface. The simulation domain boundary conditions along x axis (x_{\max} and x_{\min}) are set to periodic boundary conditions. Those along y axis (y_{\max} and y_{\min}) are set to perfectly matched layers (PML). The total absorptivity is calculated across the CuPc and PTCBI active layers.

As described in the previous section, we examined four different cases: the proposed volumetric plasmonic resonator structure that consists of top and bottom silver gratings presented in Figure 5.4, only the top silver grating shown in Figure 5.2, only the bottom silver grating depicted in Figure 5.3 and the non-metallic architecture (bare device) given in Figure 5.1. We simulated all these architectures separately under normally-incident planewave illumination in both of TM polarization (with the magnetic field pointed along the z-axis while the electric field is directed along x-axis) and TE polarization (with the electric field pointed along the z-axis while the magnetic field is directed along x-axis).

5.3 Absorption behavior of organic solar cells embedded with plasmonic structures under TE and TM polarized illumination

For the computation of absorptivity, we consider the solar cell consisting of thin-film layers of ITO with a film thickness of $LT_1=150$ nm, PEDOT:PSS with $LT_2=20$ nm, CuPC with $LT_3=11$ nm, PTCI with $LT_5=4$ nm and BCP with $LT_5=12$ nm in our simulations. These film thicknesses have been previously optimized for the corresponding solar cell structure by Peumans et al. [52]. Here all field distribution maps are normalized in the range of 0-10 for better comparison of all cases.

In our analyses, we observed that the optical absorbance is dominated by the CuPc layer in our structure since this layer is thicker than the PTCBI layer and the fields are more localized in this layer. Figure 5.5 presents the electric field distribution for the top silver grating case under TM polarized illumination at the optical wavelength of 510 nm. Here we observe that the surface plasmons are localized around the corners of the metallic grating cross-section. The opposite surface of the grating applies an effective restoring force on the present electrons in the metal. Therefore, a resonance that leads to a field localization can form around the corners of the metallic grating. The localized surface plasmons that are non-propagating excitations of the conduction electrons of the metallic structure are observed under the metallic grating. This localized surface plasmon mode concentrated in the silver grating/organic absorbing material interface increases the absorptivity of the active materials since the absorptivity is linearly proportional to the intensity (electric field square) in the volume of the active material. In this field distribution, we also examine a surface plasmon mode mainly concentrated between silver grating/ITO interface. This extraordinary field increase does not contribute to the enhanced absorption of solar cell due to non-matching condition of the active layers and the field localization.

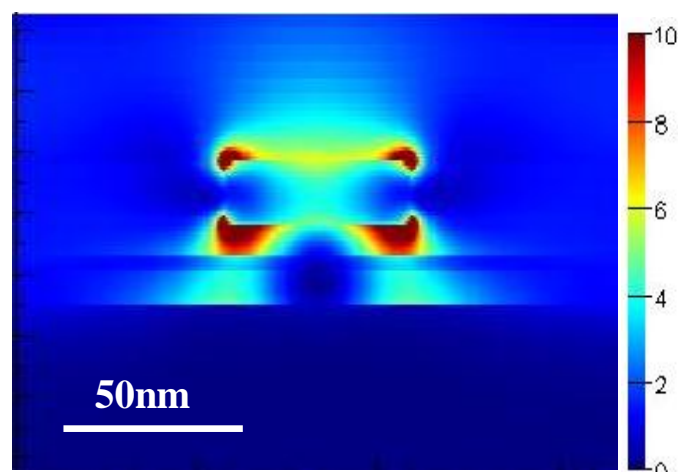


Figure 5.5: Normalized electric field profiles for the top silver grating, with the design parameters of $P=200$ nm (period of the grating), $w_1=50$ nm (width of the top metal grating) under TM-polarized normal-incident illumination at $\lambda=510$ nm. The layer thicknesses of

the solar cell are $LT1=150$ nm (ITO), $LT2=20$ nm (PEDOT:PSS), $LT3=11$ nm (CuPC), $LT4=4$ nm (PTCBI), and $LT5=12$ nm (BCP). The incident light is normal to the device structure. Only one unit cell of the repeating grating structure is shown in this electric field profile.

Figure 5.6 presents the electric field distribution for the case of only bottom silver grating structure using in the same layer thicknesses, polarization and wavelength conditions as the previous case of only top silver grating. In this case, the surface plasmons concentrated at the silver/BCP interface (right and left sides of silver grating) and also at the silver/PTCBI interface (top corners of silver grating) can be observed clearly. The surface plasmon mode at the silver/PTCBI interface increases the absorptivity of the solar cell since these surface plasmons extend across the active material PTCBI. However, the normalized field maps show that the surface plasmons concentrated around the bottom silver grating is relatively low in comparison to the previous case. This is due to the limited TM waveguide modes allowed in this interface.

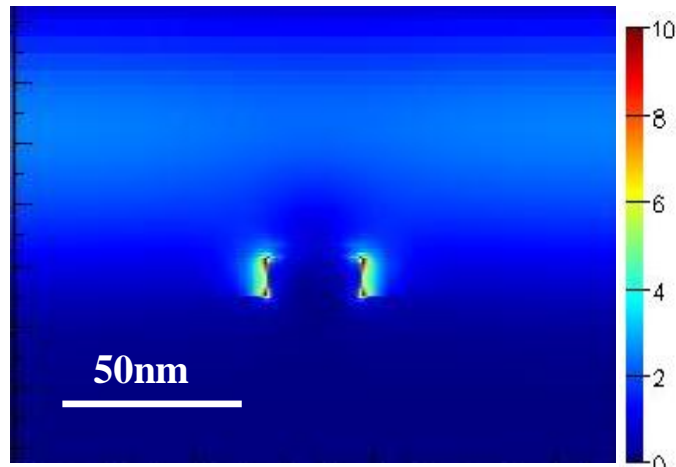


Figure 5.6: Normalized electric field profiles for the bottom silver grating, with the design parameters of $P=200$ nm (period of the grating) $w_2=30$ nm (width of the bottom metal grating) under TM-polarized normal-incident illumination at $\lambda=510$ nm. The layer thicknesses of the solar cell are $LT1=150$ nm (ITO), $LT2=20$ nm (PEDOT:PSS), $LT3=11$ nm (CuPC), $LT4=4$ nm (PTCBI), and $LT5=12$ nm (BCP). The incident light is normal to the

device structure. Only one unit cell of the repeating grating structure is shown in this electric field profile.

The normalized electric field distributions of the volumetric plasmonic resonator architecture that consists of both top and bottom silver gratings is presented in Figure 5.7. The device design and numerical simulation parameters are set to the same conditions as in the previous cases. Here we observe that the strong localized surface plasmon modes allowed at the silver/CuPc interface (bottom part of the top silver grating) and that allowed at the silver/PTCBI interface (top of the bottom silver grating) interact with each other. In addition to individual plasmonic resonances of these metallic structures, this allows for the vertical interaction or the top and bottom plasmonic structures. This coupling contributes to further enhancement of optical absorption in the active layer, beyond the limited photon absorption in the active materials of the solar cell since this field localization is mainly confined to the absorbing materials of the device. As can be clearly seen, the strongest electric field localization is obtained in the volumetric resonator in Figure 5.7, compared to the previous in Figure 5.5 and Figure 5.6.

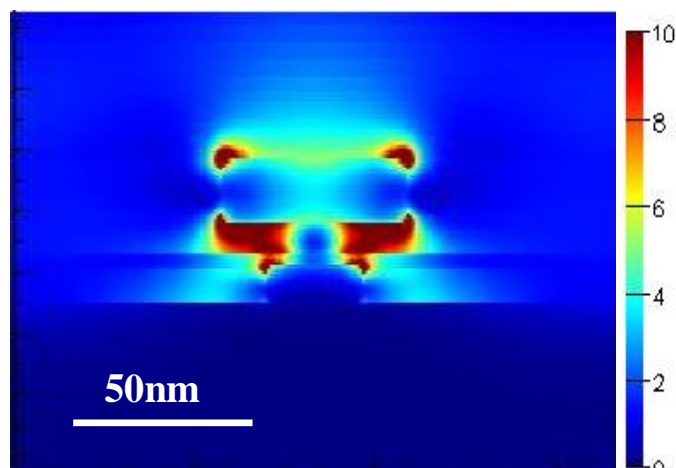


Figure 5.7: Normalized electric field profiles for the volumetric plasmonic resonator (including both the top and bottom silver gratings), with the design parameters of $P=200$ nm (period of the grating), $w_1=50$ nm (width of the top metal grating), and $w_2=30$ nm (width of the bottom metal grating) under TM-polarized normal-incident illumination at

$\lambda=510$ nm. The layer thicknesses of the solar cell are $LT1=150$ nm (ITO), $LT2=20$ nm (PEDOT:PSS), $LT3=11$ nm (CuPC), $LT5=4$ nm (PTCl), and $LT5=12$ nm (BCP). The incident light is normal to the structure. Only one unit cell of the repeating grating structure is shown in this electric field profile.

Previous electric field distributions are given for a specific wavelength ($\lambda=510$ nm) on resonance. Here we present the absorptivity spectra of the investigated architectures under TM polarization (in Figure 5.8) and TE polarization (Figure 5.9). For the first case of only the top silver grating structure embedded in PEDOT:PSS layer, it is possible to obtain strong localized surface plasmon modes in a broad-band spectral range (from 450 to 850nm) under the illumination of TM-polarized light. On the other hand, under TE-polarized light, the optical absorption level is lower. This behavior stems for the fact that the grating coupling of incoming light into the structure is blocked and the thin active layers do not allow TE waveguide modes. The optical absorption performance of the second architecture that consists of only the bottom silver grating embedded into BCP layer exhibits a performance level similar to that of the negative control group (bare solar cell). The weak surface plasmon modes generated around the metal gratings in this case do not contribute to the absorption enhancement under the TE-polarized illumination. In TM polarization, the weak suppression in the absorption spectra is due to reflection from the bottom metallic grating. Our volumetric plasmon resonator architecture based on coupling two plasmonic gratings vertically also results in a great enhancement in the optical absorption under the TM-polarized illumination, slightly better than the first case of only top grating especially at the tails of the absorptivity spectrum. The surface plasmons generated by these metallic resonators exhibits greater electric field localization extended across these structures.

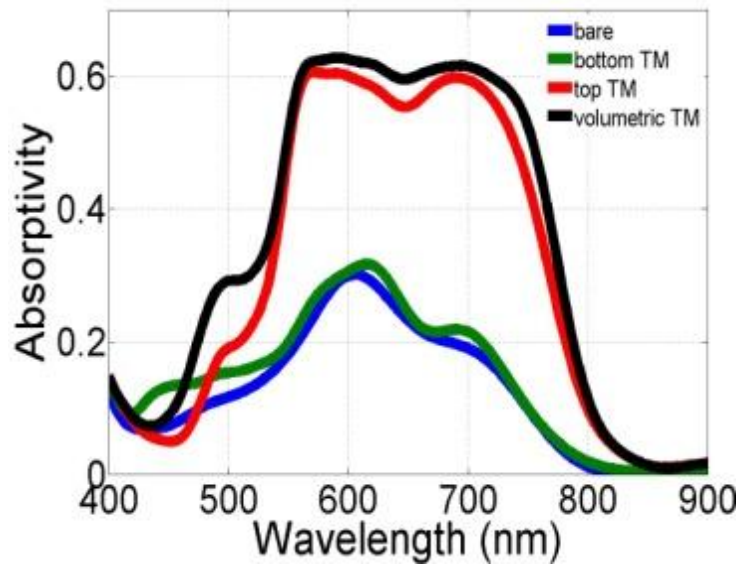


Figure 5.8: Absorption spectra of the four solar cell architectures (bare, bottom grating, top grating, and volumetric design) with the design parameters of $P=200$ nm (period of the grating), $w_1=50$ nm (width of the top metal grating), and $w_2=30$ nm (width of the bottom metal grating), under TM-polarized normal-incident illumination. The layer thicknesses of the solar cells are $LT_1=150$ nm (ITO), $LT_2=20$ nm (PEDOT:PSS), $LT_3=11$ nm (CuPC), $LT_4=4$ nm (PTCBI), and $LT_5=12$ nm (BCP).

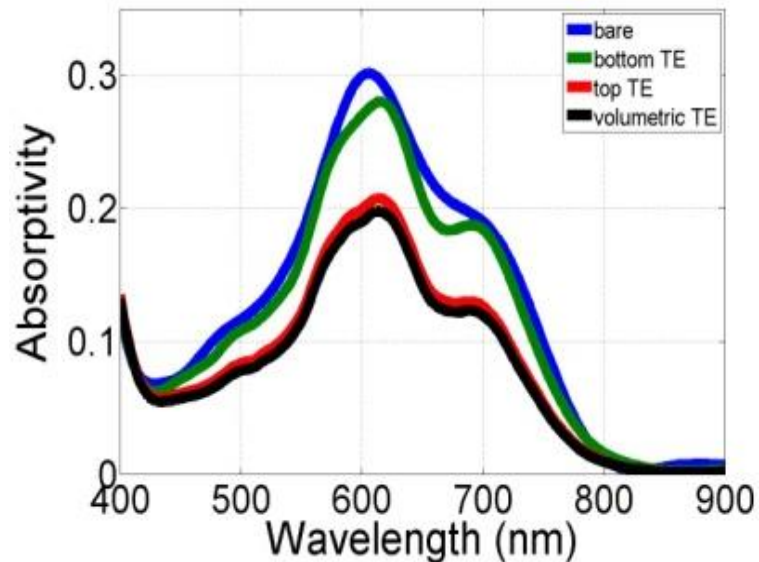


Figure 5.9: Absorption spectra of the four solar cell architectures (bare, bottom grating, top grating, and volumetric design) with the design parameters of $P=200$ nm (period of the grating), $w_1=50$ nm (width of the top metal grating), and $w_2=30$ nm (width of the bottom metal grating), under TE-polarized normal-incident illumination. The layer thicknesses of

the solar cells are $LT_1=150$ nm (ITO), $LT_2=20$ nm (PEDOT:PSS), $LT_3=11$ nm (CuPC), $LT_4=4$ nm (PTCBI), and $LT_5=12$ nm (BCP).

Figure 5.10 presents the overall absorptivity which is the average of the optical absorption (A_{TE}) under TE polarized illumination and that (A_{TM}) under TM polarized illumination, given by $(A_{TE}+A_{TM})/2$. Our results show that the volumetric plasmonic architecture exhibits a substantial absorption enhancement performance particularly under the transverse magnetic polarized illumination, while the optical absorption is maintained at a similar level under the transverse electric polarized illumination. Consequently, the volumetric plasmonic design is found to outperform the other three cases of the bare device and those with either the top or the bottom grating only. Here it is worth noting that, while the volumetric design exceeds by the performance of the bottom grating alone, its performance is only slightly better than that of the top grating alone.

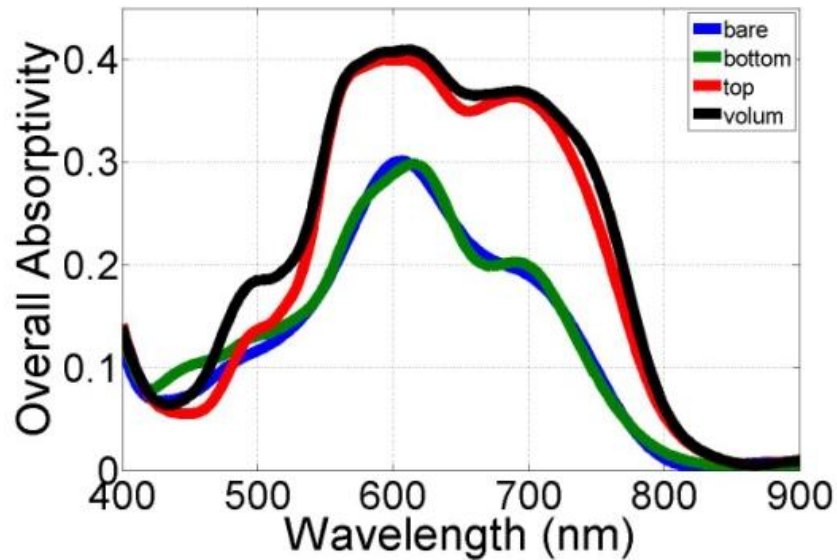


Figure 5.10: Overall absorption $(A_{TM}+A_{TE})/2$ spectra of the four solar cell architectures (bare, bottom grating, top grating, and volumetric design) with the design parameters of $P=200$ nm (period of the grating), $w_1=50$ nm (width of the top metal grating), and $w_2=30$ nm (width of the bottom metal gratings). The layer thicknesses of the solar cells are $LT_1=150$ nm (ITO), $LT_2=20$ nm (PEDOT:PSS), $LT_3=11$ nm (CuPC), $LT_4=4$ nm (PTCBI) and $LT_5=12$ nm (BCP).

In our FDTD simulations, we assume that the illuminating source has equal irradiance at every frequency. However, the actual solar spectrum has different weights at different optical frequencies, which is generally represented by the AM1.5G (air mass 1.5 global filter) solar irradiance spectrum given in Figure 5.11. The solar irradiance reaches its peak level around 500 nm. For this reason, it is important to adjust the plasmonic resonances to hit the range of 450-550 nm to take the maximum advantage of plasmonic resonators. It is important to measure and state the performance of engineered solar cells under AM1.5G solar illumination to predict the performance under real solar radiation. Considering AM1.5G solar radiation, we compute the performance enhancement (in %) of the plasmonic solar cell architectures using (5.1):

$$\frac{\int_0^{\infty} \left(\frac{A_{TM}(\lambda) + A_{TE}(\lambda)}{2} \right) * AM1.5G(\lambda) d\lambda - \int_0^{\infty} A_{bare} * AM1.5G(\lambda) d\lambda}{\int_0^{\infty} A_{bare} * AM1.5G(\lambda) d\lambda} * 100 \quad (5.1)$$

where $A_{TM}(\lambda)$ is the absorptivity in the presence of the plasmonic structure under TM polarized illumination, $A_{TE}(\lambda)$ is the absorptivity in the presence of the plasmonic structure under TE polarized illumination, $A_{bare}(\lambda)$ is the absorptivity in the absence of the plasmonic structure (which is polarization independent) and $AM1.5G(\lambda)$ is the solar irradiance spectrum. The performance enhancement under the AM1.5G solar radiation is computed to be ~67% for the volumetric plasmonic resonator architecture, which the only top resonator architecture increases the absorption performance by ~%58. Therefore, the volumetric design surpassed the top grating by ~%9 in performance enhancement.

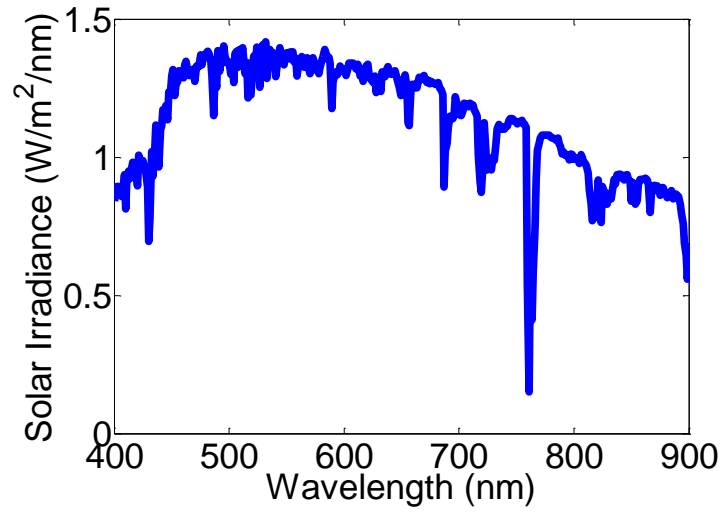


Figure 5.11: AM1.5G solar irradiance spectrum [4].

5.4 Optimization Results

We also consider the effect of silver grating periodicity on the absorptivity enhancement for only top, only bottom and volumetric resonator architectures under both TE and TM polarized illumination. We embodied three different plasmonic resonator structures investigated in our simulations by changing the width of the top resonator $w_1=50$ nm, $w_1=60$ nm, and $w_1=40$ nm. This characterization is important for understanding the coupling conditions of the bottom and top gratings as well as the volumetric design. We selected the bottom grating width as approximately half of width of the top grating, i.e., $w_2 \cong \frac{w_1}{2}$, to achieve the highest possible coupling condition of localized surface plasmons generated by top gratings and surface plasmons generated by bottom gratings. In this step, we fixed the width of the bottom grating structure to be 30 nm and changed the width of the top grating structure. We did not change any other device parameter including the layer thicknesses of the device to make a fair comparison and to avoid diminishing performance of the solar cells since these layer thickness are the optimized ones. Figure 5.15, Figure 5.16, Figure

5.17 and Figure 5.18 present the optimization results for the case of $w_1=50$ nm, $w_2=30$ nm, $LT_1=150$ nm, $LT_2=20$ nm, $LT_3=11$ nm, $LT_4=4$ nm and $LT_5=12$ nm. Subsequently Figure 5.19, Figure 5.20, Figure 5.21 and Figure 5.22 present the optimization results for the case of $w_1=60$ nm, $w_2=30$ nm, $LT_1=150$ nm, $LT_2=20$ nm, $LT_3=11$ nm, $LT_4=4$ nm and $LT_5=12$ nm. Finally Figure 5.23, Figure 5.24, Figure 5.25 and Figure 5.26 present the optimization results for the case of $w_1=40$ nm, $w_2=30$ nm, $LT_1=150$ nm, $LT_2=20$ nm, $LT_3=11$ nm, $LT_4=4$ nm and $LT_5=12$ nm.

Here the optical absorptivity vs. periodicity maps of the bare structure (Figure 5.12), only the bottom resonator structure under TE-polarized illumination (Figure 5.13), only the bottom resonator structure under TM-polarized illumination (Figure 5.14) and only the top resonator under TE-polarized illumination (Figure 5.15, 5.19, and 5.23) are normalized to absorptivity range of (0 – 0.4). The maps of the volumetric design under TM-polarized illumination (Figure 5.18, 5.22, and 5.26) and top resonator structure under TM-polarized illumination (Figure 5.16, 5.20, and 5.24) are normalized to absorptivity range of (0 – 0.65).

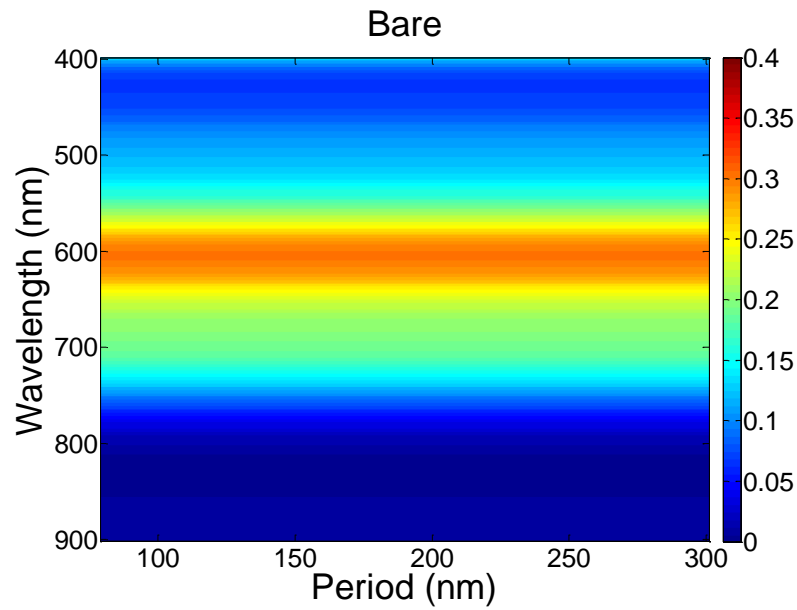


Figure 5.12: Normalized absorptivity map of the bare solar cell for comparison. These absorption spectra are computed for the parameters of $LT1=150$ nm, $LT2=20$ nm, $LT3=11$ nm, $LT4=4$ nm and $LT5=12$ nm.

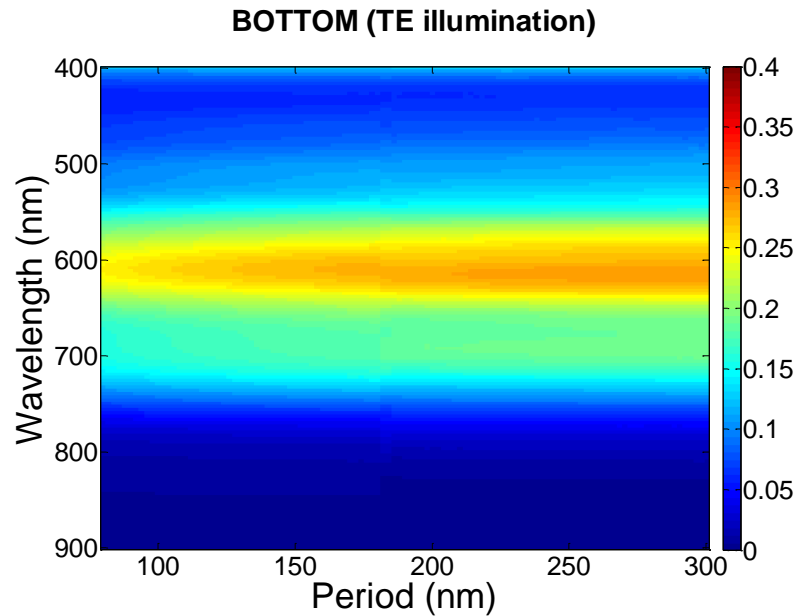


Figure 5.13: Normalized absorptivity map of only the bottom metallic grating solar cell as a function of the periodicity of the silver grating under TE-polarized light. Here the absorption spectra are computed for the device parameters of $w2=30$ nm, $LT1=150$ nm, $LT2=20$ nm, $LT3=11$ nm, $LT4=4$ nm, and $LT5=12$ nm.

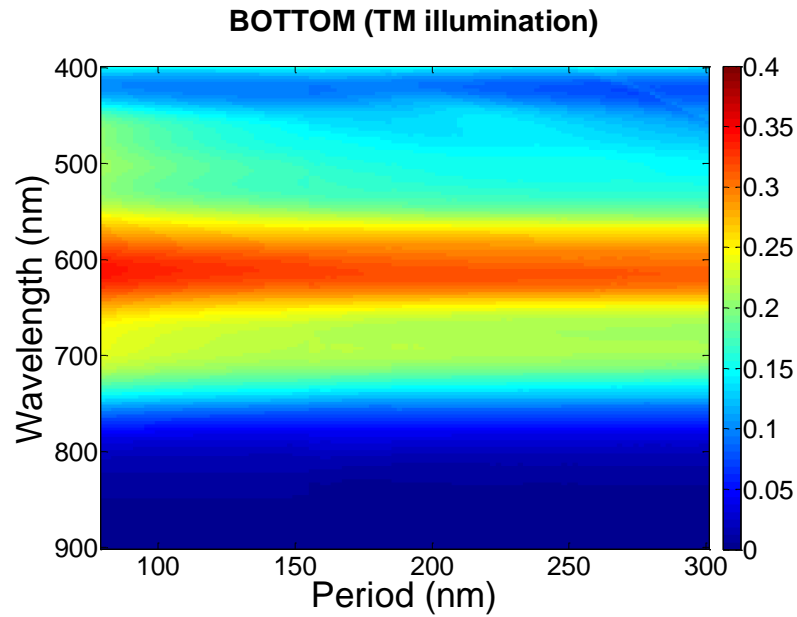


Figure 5.14: Normalized absorptivity map of only the bottom metallic grating solar cell as a function of the periodicity of the silver grating under TM-polarized light. Here the absorption spectra are computed for the device parameters of $w_2=30$ nm, $LT_1=150$ nm, $LT_2=20$ nm, $LT_3=11$ nm, $LT_4=4$ nm, and $LT_5=12$ nm.

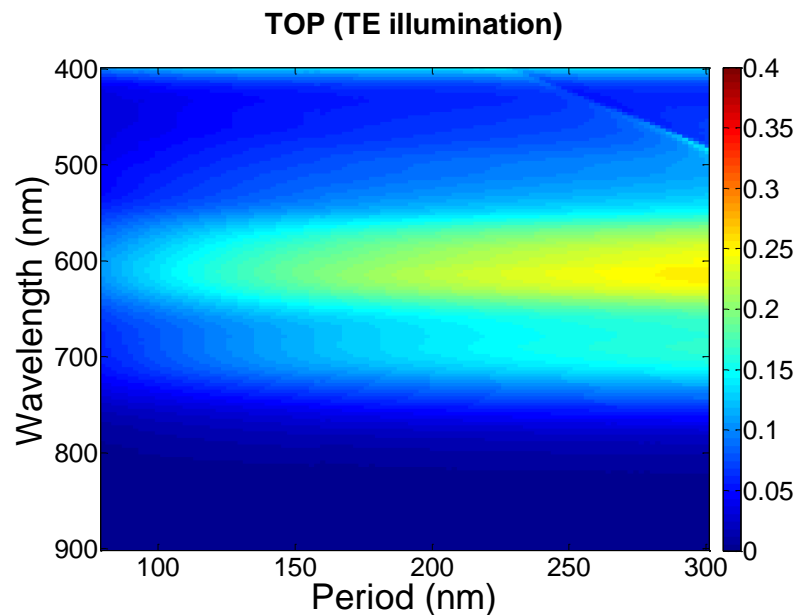


Figure 5.15: Normalized absorptivity map of only the top metallic grating solar cell as a function of the periodicity of the silver grating under TE-polarized light. Here the absorption spectra are computed for the device parameters of $w_1=50$ nm, $LT_1=150$ nm, $LT_2=20$ nm, $LT_3=11$ nm, $LT_4=4$ nm, and $LT_5=12$ nm.

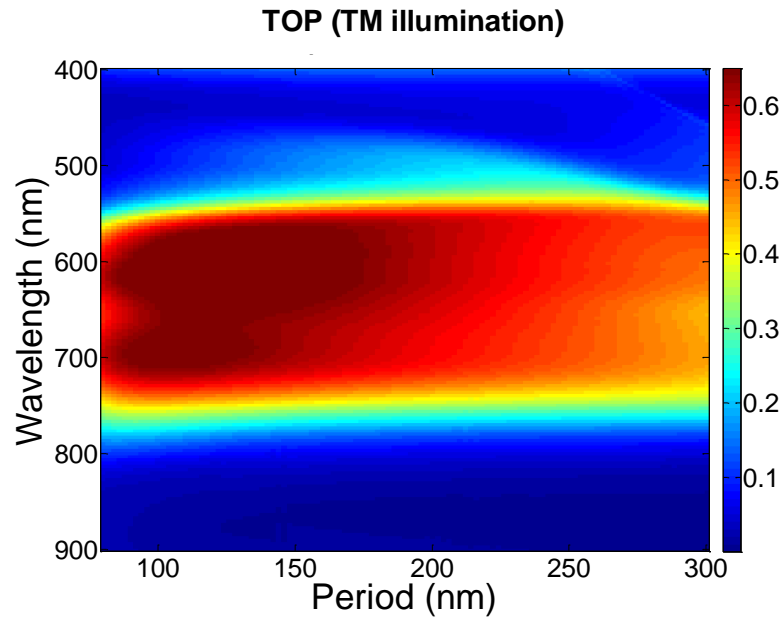


Figure 5.16: Normalized absorptivity map of only the top metallic grating solar cell as a function of the periodicity of the silver grating under TM-polarized light. Here the absorption spectra are computed for the device parameters of $w_1=50$ nm, $LT_1=150$ nm, $LT_2=20$ nm, $LT_3=11$ nm, $LT_4=4$ nm, and $LT_5=12$ nm.

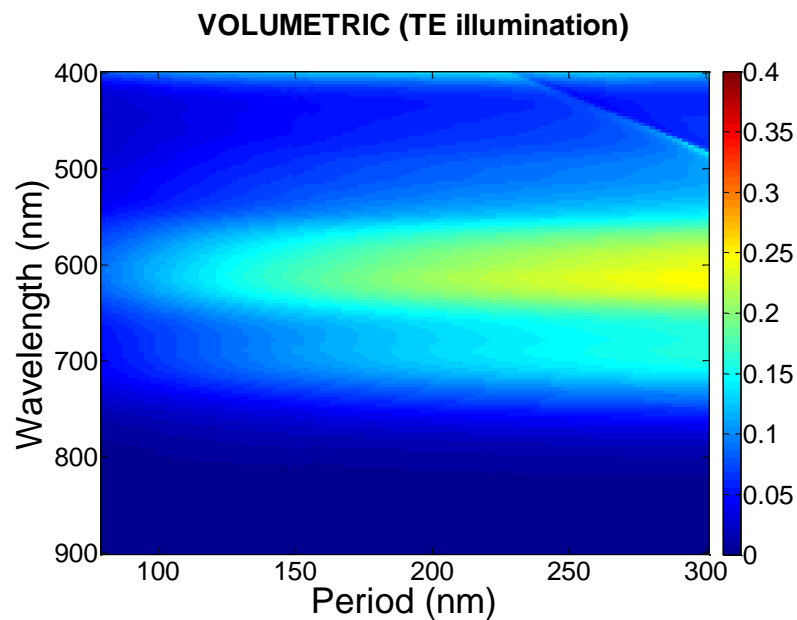


Figure 5.17: Normalized absorptivity map of volumetric metallic gratings solar cell as a function of the periodicity of the silver grating under TE-polarized light. Here the absorption spectra are computed for the device parameters of $w_1=50$ nm, $w_2=30$ nm, $LT_1=150$ nm, $LT_2=20$ nm, $LT_3=11$ nm, $LT_4=4$ nm, and $LT_5=12$ nm.

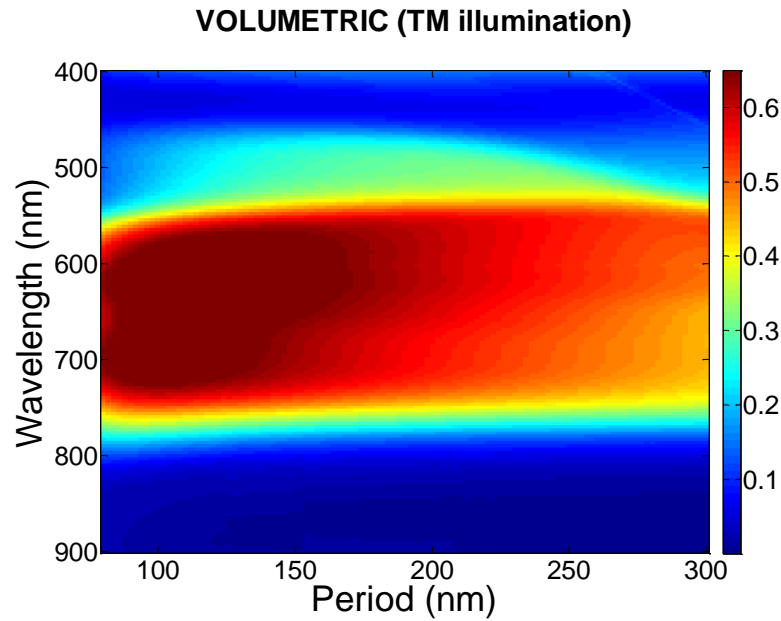


Figure 5.18: Normalized absorptivity map of volumetric metallic gratings solar cell as a function of the periodicity of the silver grating under TM-polarized light. Here the absorption spectra are computed for the device parameters of $w_1=50$ nm, $w_2=30$ nm, $LT_1=150$ nm, $LT_2=20$ nm, $LT_3=11$ nm, $LT_4=4$ nm, and $LT_5=12$ nm.

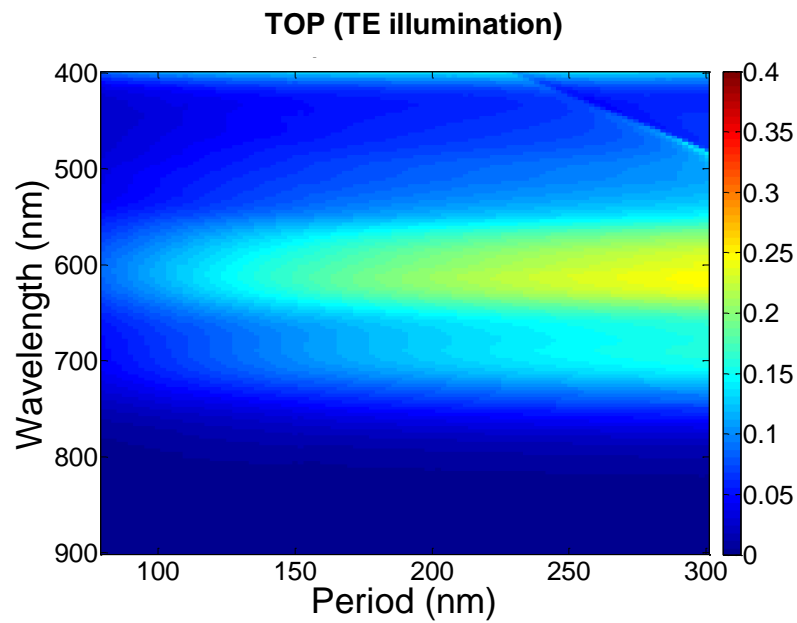


Figure 5.19: Normalized absorptivity map of only the top metallic grating solar cell as a function of the periodicity of the silver grating under TE-polarized light. Here the absorption spectra are computed for the device parameters of $w_1=60$ nm, $LT_1=150$ nm, $LT_2=20$ nm, $LT_3=11$ nm, $LT_4=4$ nm, and $LT_5=12$ nm.

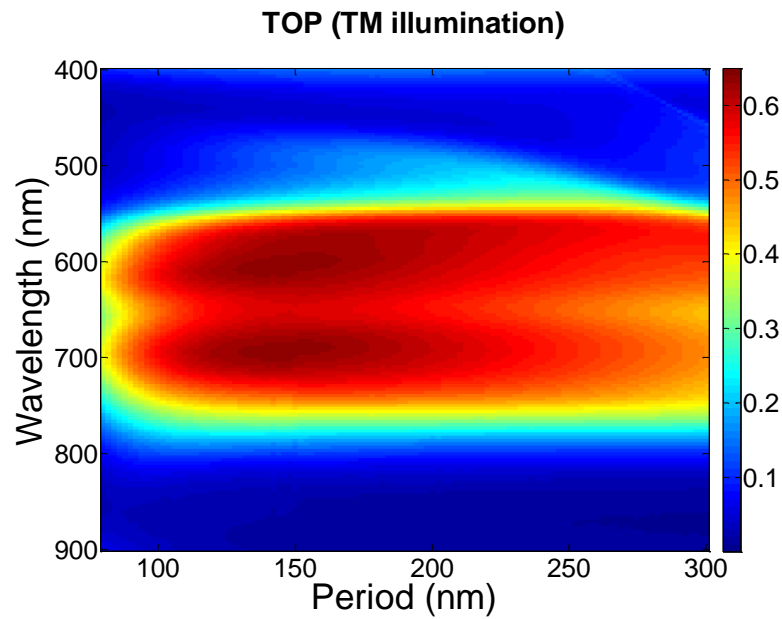


Figure 5.20: Normalized absorptivity map of only the top metallic grating solar cell as a function of the periodicity of the silver grating under TM-polarized light. Here the absorption spectra are computed for the device parameters of $w_1=60$ nm, $LT_1=150$ nm, $LT_2=20$ nm, $LT_3=11$ nm, $LT_4=4$ nm, and $LT_5=12$ nm.

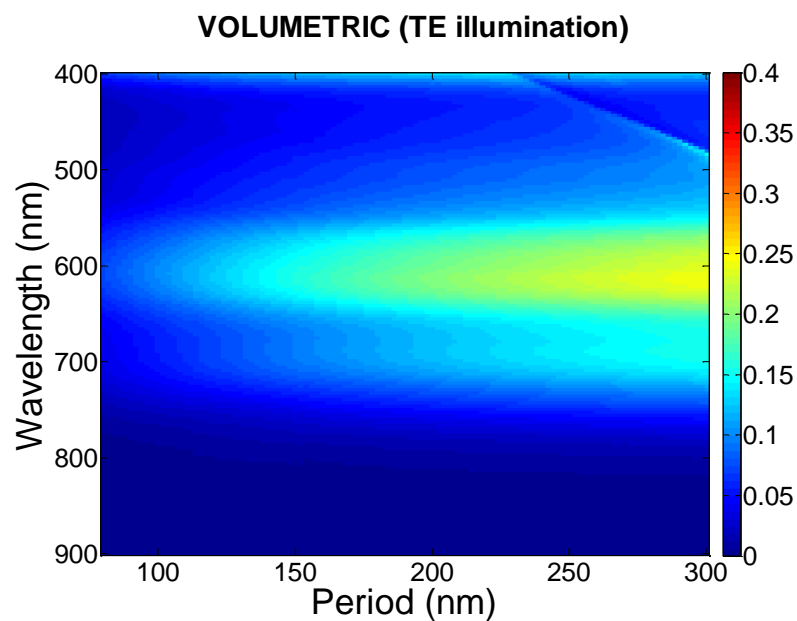


Figure 5.21: Normalized absorptivity map of volumetric metallic gratings solar cell as a function of the periodicity of the silver grating under TE-polarized light. Here the absorption spectra are computed for the device parameters of $w_1=60$ nm, $w_2=30$ nm, $LT_1=150$ nm, $LT_2=20$ nm, $LT_3=11$ nm, $LT_4=4$ nm, and $LT_5=12$ nm.

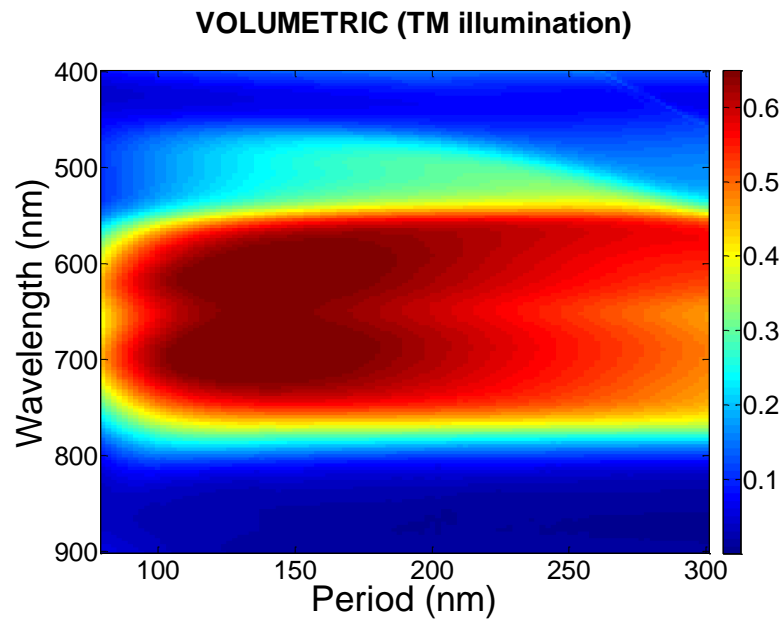


Figure 5.22: Normalized absorptivity map of volumetric metallic gratings solar cell as a function of the periodicity of the silver grating under TM-polarized light. Here the absorption spectra are computed for the device parameters of $w_1=60$ nm, $w_2=30$ nm, $LT_1=150$ nm, $LT_2=20$ nm, $LT_3=11$ nm, $LT_4=4$ nm, and $LT_5=12$ nm.

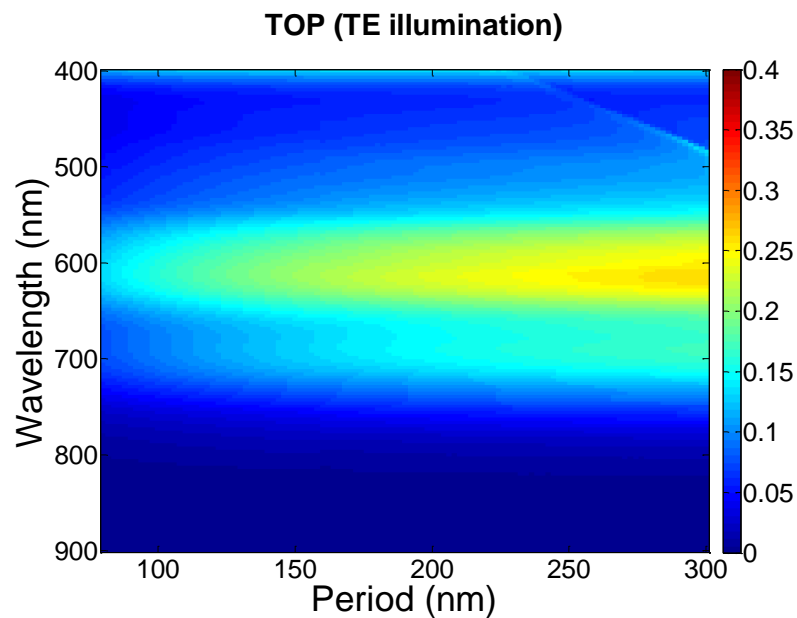


Figure 5.23: Normalized absorptivity map of only the top metallic grating solar cell as a function of the periodicity of the silver grating under TE-polarized light. Here the absorption spectra are computed for the device parameters of $w_1=40$ nm, $LT_1=150$ nm, $LT_2=20$ nm, $LT_3=11$ nm, $LT_4=4$ nm, and $LT_5=12$ nm.

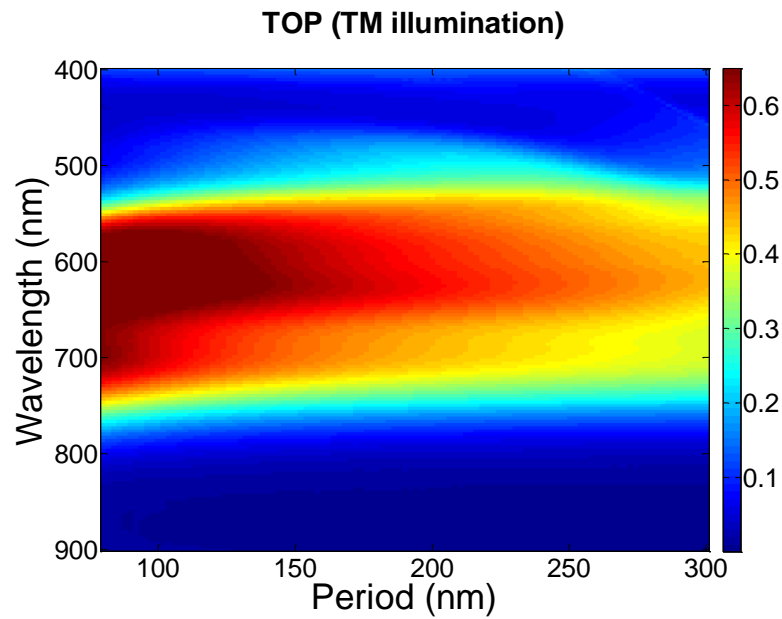


Figure 5.24: Normalized absorptivity map of only the top metallic grating solar cell as a function of the periodicity of the silver grating under TM-polarized light. Here the absorption spectra are computed for the device parameters of $w_1=40$ nm, $LT_1=150$ nm, $LT_2=20$ nm, $LT_3=11$ nm, $LT_4=4$ nm, and $LT_5=12$ nm.

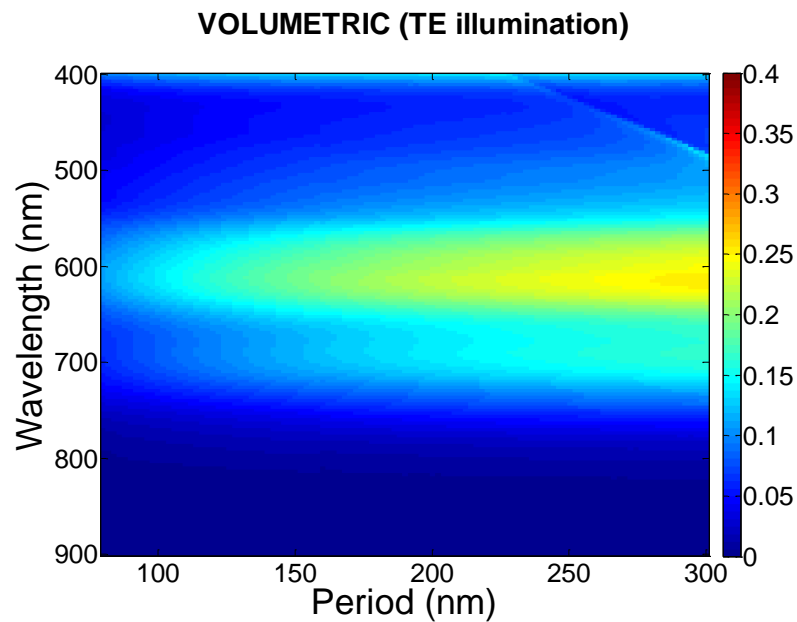


Figure 5.25: Normalized absorptivity map of volumetric metallic gratings solar cell as a function of the periodicity of the silver grating under TE-polarized light. Here the absorption spectra are computed for the device parameters of $w_1=40$ nm, $w_2=30$ nm, $LT_1=150$ nm, $LT_2=20$ nm, $LT_3=11$ nm, $LT_4=4$ nm, and $LT_5=12$ nm.

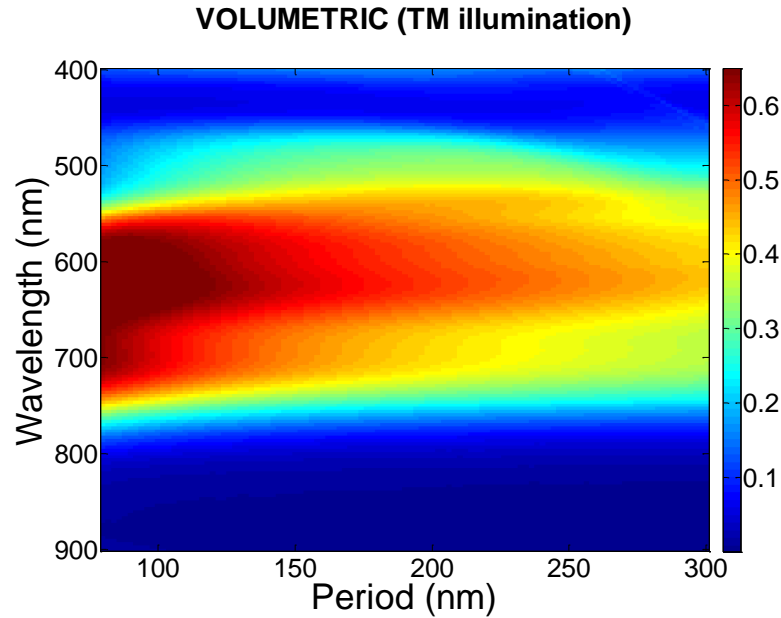


Figure 5.26: Normalized absorptivity map of volumetric metallic gratings solar cell as a function of the periodicity of the silver grating under TM-polarized light. Here the absorption spectra are computed for the device parameters of $w_1=40$ nm, $w_2=30$ nm, $LT_1=150$ nm, $LT_2=20$ nm, $LT_3=11$ nm, $LT_4=4$ nm, and $LT_5=12$ nm.

These results confirm that we obtain larger band absorptivity enhancement by embedding the volumetric architecture in this organic solar cell architecture. We observe the maximum absorptivity is achieved in the case of $80 \text{ nm} \leq P \leq 120$ nm. This is because of the increased surface plasmon modes created between the vertically coupled plasmonic resonators. When we decrease the periodicity of the gratings ($P < 80$ nm), we reduce the overall absorptivity of the solar cell since denser metallic gratings on top of the organic solar cell yields higher reflection of illuminated light.

The volumetric resonator architecture performance is predominantly set by the width of the bottom and top gratings. The highest absorptivity levels are achieved for the case of the top resonator width $w_1=50$ nm and the bottom resonator width $w_2=30$ nm. This condition is the maximized coupling condition of the top and bottom resonators together. When we considered the cases of

$w_1=40$ nm, and $w_2=30$ nm, we observe that the optical absorptivity is diminished since the illuminated light is trapped in the lower region and the resulting excited localized surface plasmons are weaker. Thus the coupling between the top and bottom grating is then decreased.

In summary, we proposed and demonstrated a volumetric plasmonic resonator architecture that embeds two vertically coupled plasmonic gratings in a single thin-film organic solar cell. By this approach, we extended and couple these gratings with each other such that the field localization is further extended and increased within the volume of the active material between the gratings. We showed a ~67% overall absorption performance enhancement in the solar cell under the AM1.5G solar illumination. This novel architecture can be easily extended and applied to different types and materials of solar cells.

Chapter 6

Conclusions

In this thesis work, we proposed and demonstrated a novel plasmonic architecture that relies on coupling multiple plasmonic structures into a volumetric resonator in a thin-film CuPc/PTCBI based organic solar cell with the aim of enhancing the optical absorption beyond the optical absorption enhancement limits of a single plasmonic layer. We also presented a new nanopatterned backcontact grating in a thin-film P3HT:PCBM based organic solar cell to enhance the optical absorption under both TE- and TM-polarized illumination for first time in the literature.

In this thesis, we introduced the basics of surface plasmons, localized surface plasmons and reviewed the plasmonic architectures previously investigated for enhancing the absorption in the literature. We also presented an overview of the organic solar cells, their principles of operation and materials commonly used in the fabrication of organic solar cells.

For the first time in the literature, we demonstrated a volumetric plasmonic resonator architecture that integrates two vertically coupled plasmonic gratings in a single organic solar cell. For this, we incorporated one silver grating on the top of the absorbing layer and another at the bottom of the absorbing layer to interact them with each other such that the field localization is further increased and extended within the volume of the active material between the gratings. In addition to individual plasmonic resonances of these metallic structures, this approach allows us to take the advantage of the vertical interaction in the volumetric resonator. The results demonstrate that we enhance the optical absorption in the CuPc/PTCBI based organic solar cell structure up to ~67% under the AM1.5G solar radiation. This work shows that it is possible to enhance the optical absorption beyond the absorption limits of a single plasmonic structure and this design approach may be extended to different types of organic solar cell architectures and inorganic ultra thin-film solar cell architectures that also suffer from low optical absorption of incoming photons.

Additionally, we worked on a new plasmonic architecture based on applying periodic silver grating on the backcontact in a widely fabricated thin-film solar cell device of P3HT:PCBM active material. In the literature, various types of such metallic architectures have previously been proposed to take the advantage of surface plasmon resonances for enhancing the optical absorption of the active layers, and backcontact grating is one of them. However it is challenging to design a proper plasmonic architecture that matches a real solar cell device to achieve large absorption enhancement in both polarizations. In the literature, there is no previous report of on embedding metallic backcontact grating architecture in widely-used, P3HT:PCBM based thin-film organic solar cell. In this work, we demonstrate a ~21% performance enhancement under AM1.5G solar radiation under TE- and TM-polarized illumination compared to the bare organic cell structure even when the active material is substituted by placing metallic gratings and no additional active material is added.

We are in the process of disseminating our research results presented in Chapter 4 and Chapter 5 separately to two SCI journals [70,71]. Moreover, a part of Chapter 5 material will be presented at to a refereed international conference [72].

BIBLIOGRAPHY

- [1] Intergovernmental Panel on Climate Change (IPCC), Climate Change 2007: The Physical Science Basis Fourth Assessment Report Summary for Policymaker (2007)
- [2] U.S. Environmental Protection Agency (EPA), Inventory of U.S. Greenhouse Gas Emissions and Sinks: 1990-2005 (2007)
- [3] Green, M. (2000). Photovoltaics: technology overview. *Energy Policy*, 28(14), 989-998.
- [4] Atwater, H. A., Polman, A. (2010). Plasmonics for improved photovoltaic devices. *Nature Materials*, 9(3), 205-13.
- [5] Schuller, J. A., Barnard, E. S., Cai, W., Jun, Y. C., White, J. S., Brongersma, M. L. (2010). Plasmonics for extreme light concentration and manipulation. *Nature Materials*, 9(3), 193-204.
- [6] Barnes, W. L., Dereux, A., Ebbesen, T. W. (2003). Surface plasmon subwavelength optics. *Nature*, 242, 824-830.
- [7] Maier, S. A., Plasmonics: Fundamentals and Applications, Springer (2007)
- [8] Brongersma, M. L., Kik P. G., Surface Plasmon Nanophotonics, Springer Series in Optical Sciences, Springer (2007)
- [9] Shalaev V. M., Kawata S., Nanophotonics with Surface Plasmons, Elsevier (2007)
- [10] Catchpole, K. R., & Polman, A. (2008). Plasmonic solar cells. *Optics Express*, 16(26), 21793-21800.
- [11] Lim, S. H., Mar, W., Matheu, P., Derkacs, D., Yu, E. T. (2007). Photocurrent spectroscopy of optical absorption enhancement in silicon photodiodes via scattering from surface plasmon polaritons in gold nanoparticles. *Journal of Applied Physics*, 101104309.
- [12] Akimov, Y. A., Koh, W. S., Ostrikov, K. (2009). Enhancement of optical absorption in thin-film solar cells through the excitation of higher-order nanoparticle plasmon modes. *Optics Express*, 17(12), 10195-205.

- [13] Hägglund, C., Kasemo, B. (2009). Nanoparticle plasmonics for 2D-photovoltaics: mechanisms, optimization, and limits. *Optics Express*, 17(14), 11944-57.
- [14] Derkacs, D., Lim, S. H., Matheu, P., Mar, W., Yu, E. T. (2006). Improved performance of amorphous silicon solar cells via scattering from surface plasmon polaritons in nearby metallic nanoparticles. *Applied Physics Letters*, 89(9), 093103.
- [15] Schaadt, D. M., Feng, B., Yu, E. T. (2005). Enhanced semiconductor optical absorption via surface plasmon excitation in metal nanoparticles. *Applied Physics Letters*, 86(6), 063106.
- [16] Nakayama, K., Tanabe, K., Atwater, H. A. (2008). Plasmonic nanoparticle enhanced light absorption in GaAs solar cells. *Applied Physics Letters*, 93121904.
- [17] Pryce, I. M., Koleske, D. D., Fischer, A. J., Atwater, H. A. (2010). Plasmonic nanoparticle enhanced photocurrent in GaN/InGaN/GaN quantum well solar cells. *Applied Physics Letters*, 96(15), 153501.
- [18] Akimov, Y. A., Ostrikov, K., Li, E. P. (2009). Surface Plasmon Enhancement of Optical Absorption in Thin-Film Silicon Solar Cells. *Plasmonics*, 4(2), 107-113.
- [19] Beck, F. J., Polman, A., Catchpole, K. R. (2009). Tunable light trapping for solar cells using localized surface plasmons. *Journal of Applied Physics*, 105(11), 114310.
- [20] Pillai, S., Catchpole, K. R., Trupke, T., Green, M. A. (2007). Surface plasmon enhanced silicon solar cells. *Journal of Applied Physics*, 101093105.
- [21] Mokkaṡpati, S., Beck, F. J., Polman, A., Catchpole, K. R. (2009). Designing periodic arrays of metal nanoparticles for light-trapping applications in solar cells. *Applied Physics Letters*, 95(5), 053115.
- [22] Beck, F. J., Mokkaṡpati, S., Polman, A., Catchpole, K. R. (2010). Asymmetry in photocurrent enhancement by plasmonic nanoparticle

- arrays located on the front or on the rear of solar cells. *Applied Physics Letters*, 96(3), 033113.
- [23] Pala, R. A., White, J., Barnard, E., Liu, J., Brongersma, M. L. (2009). Design of Plasmonic Thin-Film Solar Cells with Broadband Absorption Enhancements. *Advanced Materials*, 21(34), 3504-3509.
- [24] Rockstuhl, C., Lederer, F. (2009). Photon management by metallic nanodiscs in thin film solar cells. *Applied Physics Letters*, 94(21), 213102.
- [25] Panoiu, N. C., Osgood, R. M. (2007). Enhanced optical absorption for photovoltaics via excitation of waveguide and plasmon-polariton modes. *Optics Letters*, 32(19), 2825-7.
- [26] Min, C., Li, J., Veronis, G., Lee, J., Fan, S., Peumans, P., (2010). Enhancement of optical absorption in thin-film organic solar cells through the excitation of plasmonic modes in metallic gratings. *Applied Physics Letters*, 96(13), 133302.
- [27] Rockstuhl, C., Fahr, S., Lederer, F. (2008). Absorption enhancement in solar cells by localized plasmon polaritons. *Journal of Applied Physics*, 104123102.
- [28] Hägglund, C., Zäch, M., Petersson, G., Kasemo, B. (2008). Electromagnetic coupling of light into a silicon solar cell by nanodisk plasmons. *Applied Physics Letters*, 92053110.
- [29] Shen, H., Bienstman, P., Maes, B. (2009). Plasmonic absorption enhancement in organic solar cells with thin active layers. *Journal of Applied Physics*, 106(7), 073109.
- [30] Wang, J., Tsai, F., Huang, J., Chen, C., Li, N., Kiang, Y. (2010). Enhancing InGaN-based solar cell efficiency through localized surface plasmon interaction by embedding Ag nanoparticles in the absorbing layer. *Optics Express*, 18(3), 2682-94.
- [31] Lindquist, N. C., Luhman, W. A., Oh, S., Holmes, R. J. (2008). Plasmonic nanocavity arrays for enhanced efficiency in organic photovoltaic cells. *Applied Physics Letters*, 93(12), 123308.

- [32] Duche, D., Torchio, P., Escoubas, L., Monestier, F., Simon, J., Flory, F. (2009). Improving light absorption in organic solar cells by plasmonic contribution. *Solar Energy Materials and Solar Cells*, 93(8), 1377-1382.
- [33] Fahr, S., Rockstuhl, C., Lederer, F. (2010). Improving the efficiency of thin film tandem solar cells by plasmonic intermediate reflectors. *Photonics and Nanostructures - Fundamentals and Applications*. Elsevier B.V.
- [34] Bai, W., Gan, Q., Bartoli, F., Zhang, J., Cai, L., Huang, Y. (2009). Design of plasmonic back structures for efficiency enhancement of thin-film amorphous Si solar cells. *Optics Letters*, 34(23), 3725-7.
- [35] Zeng, L., Bermel, P., Yi, Y., Alamariu, B. A., Broderick, K. A., Liu, J. (2008). Demonstration of enhanced absorption in thin film Si solar cells with textured photonic crystal back reflector. *Applied Physics Letters*, 93(22221105).
- [36] Sai, H., Fujiwara, H., Kondo, M. (2009). Back surface reflectors with periodic textures fabricated by self-ordering process for light trapping in thin-film microcrystalline silicon solar cells. *Solar Energy Materials and Solar Cells*, 93(6-7), 1087-1090.
- [37] Rand, B. P., Peumans, P., Forrest, S. R. (2004). Long-range absorption enhancement in organic tandem thin-film solar cells containing silver nanoclusters. *Journal of Applied Physics*, 96(12), 7519.
- [38] Haug, F., Söderström, T., Cubero, O., Terrazzoni-Daudrix, V., Ballif, C. (2008). Plasmonic absorption in textured silver back reflectors of thin film solar cells. *Journal of Applied Physics*, 104(6), 064509.
- [39] Zhou, D., Biswas, R. (2008). Photonic crystal enhanced light-trapping in thin film solar cells. *Journal of Applied Physics*, 103(9), 093102.
- [40] Ferry, V. E., Verschuur, M. A., Li, H. B., Schropp, R. E., Atwater, H. A., Polman, A., (2009). Improved red-response in thin film a-Si:H solar cells with soft-imprinted plasmonic back reflectors. *Applied Physics Letters*, 95(18), 183503.

- [41] Bermel, P., Luo, C., Zeng, L., Kimerling, L. C., Joannopoulos, J. D. (2007). Improving thin-film crystalline silicon solar cell efficiencies with photonic crystals. *Optics Express*, 15(25), 16986.
- [42] Sha, W. E., Choy, W. C., Chew, W. C. (2010). A comprehensive study for the plasmonic thin-film solar cell with periodic structure. *Optics Express*, 18(6), 5993-6007.
- [43] Ameri, T., Dennler, G., Lungenschmied, C., Brabec, C. J. (2009). Organic tandem solar cells: A review. *Energy & Environmental Science*, 2(4), 347.
- [44] Hoppe, H., Sariciftci, N. S. (2004). Organic solar cells: An overview. *Journal of Materials Research*, 19(7), 1924-1945.
- [45] Green, M. A., Emery, K., Hishikawa, Y., Warta, W. (2010). Solar cell efficiency tables (version 35). *Progress in Photovoltaics: Research and Applications*, 18(2), 144-150.
- [46] Gaudiana, R., Brabec, C. (2008). Fantastic plastic. *Group*, 2(May), 287-289.
- [47] Günes, S., Neugebauer, H., Sariciftci, N. S. (2007). Conjugated polymer-based organic solar cells. *Chemical Reviews*, 107(4), 1324-38.
- [48] Clarke, T. M., & Durrant, J. R. (2010). Charge Photogeneration in Organic Solar Cells. *Chemical Reviews*.
- [49] Tumbleston, J. R., Ko, D., Samulski, E. T., Lopez, R. (2009). Electrophotonic enhancement of bulk heterojunction organic solar cells through photonic crystal photoactive layer. *Applied Physics Letters*, 94(4), 043305.
- [50] Kim, S., Cho, C., Kim, B., Choi, Y., Park, S., Lee, K., (2009). The effect of localized surface plasmon on the photocurrent of silicon nanocrystal photodetectors. *Applied Physics Letters*, 94(18), 183108.
- [51] Ferry, V. E., Sweatlock, L. A., Pacifici, D., Atwater, H. A. (2008). Plasmonic nanostructure design for efficient light coupling into solar cells. *Nano Lett.*, 8(12), 4391-4397.

- [52] Agrawal, M., Peumans, P. (2008). Broadband optical absorption enhancement through coherent light trapping in thin-film photovoltaic cells. *Optics express*, 16(8), 5385-96.
- [53] Liu, Z., Kwong, C., Cheung, C., Djuricic, a., Chan, Y., Chui, P., (2005). The characterization of the optical functions of BCP and CBP thin films by spectroscopic ellipsometry. *Synthetic Metals*, 150(2), 159-163.
- [54] Monestier, F., Simon, J., Torchio, P., Escoubas, L., Flory, F., Bailly, S., (2007). Modeling the short-circuit current density of polymer solar cells based on P3HT:PCBM blend. *Solar Energy Materials and Solar Cells*, 91(5), 405-410.
- [55] Dullivan, D. (2000). *Electromagnetic Simulation using the FDTD method*. IEEE Press.
- [56] Allen Taflove (2005). *Computational Electromagnetics: The Finite-Difference Time-Domain Method*. Boston: Artech House.
- [57] Geens, W. (2002). Organic co-evaporated films of a PPV-pentamer and C60: model systems for donor/acceptor polymer blends. *Thin Solid Films*, 403-404, 438-443.
- [58] Peumans, P., Uchida, S., Forrest, S. R. (2003). Efficient bulk heterojunction photovoltaic cells using small-molecular-weight organic thin films. *Nature*, 425(6954), 158-62.
- [59] Gebeyehu, D. (2003). Bulk-heterojunction photovoltaic devices based on donor-acceptor organic small molecule blends. *Solar Energy Materials and Solar Cells*, 79(1), 81-92.
- [60] G. Yu, A.J. Heeger (1995) Charge separation and photovoltaic conversion in polymer composites with internal donor/acceptor heterojunctions. *Journal of Applied. Physics*. 78, 4510.
- [61] J.J.M. Halls, C.A. Walsh, N.C. Greenham, E.A. Marseglia, R.H. Friend, S.C. Moratti, A.B. Holmes (1995). Efficient photodiodes from interpenetrating polymer networks. *Nature* 376, 498.
- [62] K. Tada, K. Hosada, M. Hirohata, R. Hidayat, T. Kawai, M. Onoda, M. Teraguchi, T. Masuda, A.A. Zakhidov, and K. Yoshino (1997). Donor

- polymer (PAT6) - acceptor polymer (CN- PPV) fractal network photocells. *Synth. Met.* 85, 1305.
- [63] G. Yu, J. Gao, J.C. Hummelen, F. Wudl, and A.J. Heeger: Polymer photovoltaic cells (1995). Enhanced efficiencies via a network of internal donor-acceptor heterojunctions. *Science* 270, 1789.
- [64] C.Y. Yang and A.J. Heeger (1996). Morphology of composites of semiconducting polymers mixed with C60. *Synth. Materials.* 83, 85.
- [65] J.J. Dittmer, R. Lazzaroni, P. Leclere, P. Moretti, M. Granstro, K. Petritsch, E.A. Marseglia, R.H. Friend, J.L. Bredas, H. Rost, and A.B. Holmes (2000). Crystal network formation in organic solar cells. *Sol. Energy Material Solar Cells* 61, 53.
- [66] J.J. Dittmer, E.A. Marseglia, R.H. Friend (2000). Electron trapping in dye/polymer blend photovoltaic cells. *Advanced Materials* 12, 1270.
- [67] Petritsch, K. (2000). Dye-based donor/acceptor solar cells. *Solar Energy Materials and Solar Cells*, 61(1), 63-72.
- [68] Schmidt-Mende, L., Fechtenkötter, a., Müllen, K., Moons, E., Friend, R. H., MacKenzie, J. D. (2001). Self-organized discotic liquid crystals for high-efficiency organic photovoltaics. *Science*, 293(5532), 1119-22.
- [69] Palik, E.D. Handbook of Optical constants of solids, Academic Press (1998)
- [70] M.A. Sefünç, A. K. Okyay, H. V. Demir, Volumetric plasmonic resonator architecture for thin-film solar cells, in submission (2010).
- [71] M.A. Sefünç, A. K. Okyay, H. V. Demir, Increased absorption for all polarizations via excitations of plasmonic modes in metallic grating backcontact, in submission (2010).
- [72] M.A. Sefünç, A. K. Okyay, H. V. Demir, Volumetric plasmonic resonators for very thin organic solar cells. 23rd Annual Lasers and Electro Optics Society Meeting, 7-11 November 2010 Denver, USA. Session: Solar Cell Devices and Materials

- [73] Pettersson, L. A., Ghosh, S., Ingan, O. (2002). Optical anisotropy in thin films of poly (3 , 4-ethylenedioxythiophene)– poly (4-styrenesulfonate). *Organic Electronics*, 3, 143-148.
- [74] Co, J. A., Street, M. (1998). Spectroscopic ellipsometry characterization of indium tin oxide film microstructure and optical constants. *Thin Solid Films*, 394-397.